STRONG AND ULTRASTRONG LIGHT-MATTER INTERACTIONS IN MULTILAYER OPTICAL ORGANIC NANOSTRUCTURES

by

BIN LIU

Submitted in partial fulfillment of the requirements

For the degree of Doctor of Philosophy

Dissertation Advisor: Kenneth D. Singer, Ph.D.

Department of Physics

CASE WESTERN RESERVE UNIVERSITY

January, 2018

CASE WESTERN RESERVE UNIVERSITY
SCHOOL OF GRADUATE STUDIES

We hereby approve the thesis/dissertation of

BIN LIU

candidate for the **Doctor of Philosophy** degree [1].

Prof. Kenneth D. Singer

Committee Chair, Advisor
Department of Physics

Prof. Rolfe G. Petschek

Committee Member
Department of Physics

Prof. Giuseppe Strangi

Committee Member
Department of Physics

Prof. Clemens Burda

Committee Member
Department of Chemistry

(date) November 29, 2017

[1]We also certify that written approval has been obtained for any proprietary material contained therein.

To my family

Table of Contents

List of Tables

List of Figures

Acknowledgments

First and foremost, I am extremely grateful to my advisor, Professor Kenneth D. Singer, and it has been a privilege to have him to guide my Ph.D. study. What I learned from him was not only experimental expertise, but more importantly, how to be an experienced scientific researcher with strong enthusiasm and responsibility. I deeply appreciate his continued guidance, encouragement and support, both professionally and personally, to make my Ph.D. experience a stimulating and wonderful journey.

I would also like to thank Professor Rolfe G. Petschek, Professor Giuseppe Strangi and Professor Clemens Burda for serving on my dissertation committee and for their careful review and helpful suggestions on this thesis.

I express my sincerest gratitude to my collaborators, Professor Robert J. Twieg and Dr. Prabin Rai from Kent State University, Professor Mercouri G. Kanatzidis, Professor Tobin J. Marks, Dr. Constantinos C. Stoumpos, and Dr. Chan Myae Myae Soe from Northwestern University, Dr. Wanyi Nie, Dr. Hsinhan Tsai, and Dr. Aditya D. Mohite from Los Alamos National Laboratory, and Professor Michael J. Crescimanno from Youngstown State University. Most of my research was done in close cooperation with them, and I greatly appreciate their tremendous cooperation.

I am also indebted to all the alumni and current members in our Organic Optoelectronic laboratory, particularly Dr. Cory W. Christenson, Dr. Brent Valle, Dr. Anuj Saini, Michael Patrick, Kyle Peters, Michael McMaster, and Samuel Schwab.

I would also like to thank the many other outstanding colleagues in the Case Physics Department who instructed or assisted me in the past years. I would like

to thank Professor Philip Taylor, Professor Walter Lambrecht, Professor Jesse Berezovsky and Professor Robert Brown for teaching my courses during the program. I deeply appreciate the help from Dr. Ina T. Martin for facility use at the MORE center. I also want to thank the administrative staff, Lori Morton, Betty Gaffney and Georgia Wilkins, for their excellent work making my everyday life much more enjoyable in our department.

Last, but certainly not least, I must acknowledge with tremendous thanks to my family for their endless love and encouragement. I would like to thank my parents, Mrs. Xingyun Wu and Mr. Zhigang Liu, for the sacrifice that they have made to give me this life. I also thank my lovely wife, Jie (Olivia) Wang, whose support has kept me afloat throughout this entire process. Lastly, I would like to thank my grandparents, Mrs. Lanying Zhang and Mr. Qingchang Liu, who raise me and provide extraordinary support since my childhood. My grandma is suffering cancer, and currently her only wish is that I can come home soon, as I have not been back home for almost six years, thus her wish for my return and the rest of my family's support have encouraged me emotionally to finish my Ph.D. journey.

Abstract

Strong and Ultrastrong Light-Matter Interactions in Multilayer Optical Organic Nanostructures

by

BIN LIU

Light-matter interactions in multilayer organic nanostructures give rise to an abundance of interesting phenomena, and provide a functional platform for useful optical devices with sophisticated designs via fine control of the optical properties of the constituent materials and the thicknesses of each layers. This thesis focuses on the theoretical and experimental study of linear and nonlinear optical (NLO) properties of multilayer organic nanostructures in order to characterize the interaction between light and matter within the multilayer structure from a fundamental point of view, and to improve the linear and NLO efficiency of layered devices for practical applications.

Metallic Fabry-Pérot cavities filled with organic materials, as a typical multilayer structure, demonstrate strong and ultrastrong light-matter interaction, where hybrid quantum states known as cavity polaritons are formed. Moreover, compared to strongly coupled exciton-photon cavities, double organic cavities exhibit interesting optical properties in the ultrastrong coupling regime, yielding a broken degeneracy of vacuum Rabi splittings due to breaking of the rotating wave approximation (RWA). For the NLO properties, resonant third-harmonic generation (THG) can be enhanced

by cavity polariton states, and THG intensity is seen to be larger when the polariton state is more exciton-like.

Two-dimensional (2D) perovskite-based planar photovoltaic cells, as another typical multilayer structure, exhibit greatly improved environmental stability and photostability under operating conditions comparing with their 3D counterparts. We have investigated and designed devices using optical modeling. The absorption in the photoactive layer can be enhanced due to light-matter interaction in multilayer structures by carefully designing the layer thicknesses. In addition, using a modified drift-diffusion model, charge-carrier recombination is studied, which limits to the device performance of modest-mobility perovskite solar cells, while depending on the layer thickness. Therefore, the thickness optimization is investigated considering both aspects, which guides device fabrication with high power-conversion efficiencies.

Coextruded multilayered polymer films containing a NLO chromophore, a new alignment strategy for NLO chromophore, are studied by the second-harmonic generation (SHG) technique, which give rise to a second-order nonlinear optical response.

1 Introduction

1.1 Overview

The interaction between light and matter determines the appearance of the natural world around us. In particular, multilayer structures give rise to very fascinating optical phenomena, such as the brilliant iridescence of bubbles and butterfly wings that are produced by multilayer inteference.[1] Inspired from nature, multilayer structures have been mimicked and refined for both fundamental study and practical applications, for example, in distributed Bragg reflector (DBR) mirrors,[2] anti-reflective coatings,[3] and photovoltaic devices.[4] Interaction can occur between atoms or solids and light from solar radiation, and continuous-wave (CW) and pulsed lasers. In addition, the properties of materials can be strongly modified due to their interaction with light. Based on the characteristics of the layered materials, in particular, there are two questions addressed here:

1. How to characterize the interaction between light and matter within the planar organic cavities from a fundamental point of view?

2. How to further improve the efficiency of layered photovoltaic devices by exploiting the interaction between the optical field and each layer of material?

To answer these two questions, both the relevant theory and experiment are investigated. The basic concepts of light-matter interactions in multilayer structures will be introduced in the following sections, including the nonlinear optics and multilayer photovoltaic devices.

1.2 Introduction to Light-Matter Interaction

1.2.1 Basics of Light-Matter Interaction

The picture of the interaction process between light and atoms or molecules can be described as the coupling between the electromagnetic (EM) field and the transition dipoles of materials, for example, using a two-level model that satisfy:[5]

$$E_2 - E_1 = \hbar\omega. \tag{1.1}$$

where E_1 and E_2 are energies for the ground state and excited state, respectively. ω is the transition frequency between the ground state and excited state, and $\hbar$ is the reduced Planck constant.

As illustrated in Fig. 1.1, due to the interaction of oscillating field of light with transition dipoles, the the absorption process is viewed in terms of the destruction of a photon from the light beam with the excitation of materials, while the emission process corresponds to the addition of a photon to the light field and the de-excitation of materials.

Importantly, the light-matter interaction will become more complicated and important for nanostructured complex system with specific structures,[6] which can provide promising photonic and electronic properties. Also, a planar microcavity as a

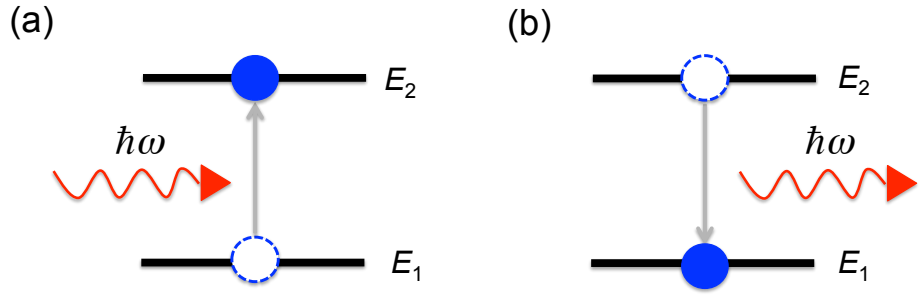

Figure 1.1. Optical transitions between quantized energy levels: (a) absorption; (b) emission.

typical multilayer structure can confine the light and give rise to cavity resonant modes, which we will discuss in the next section.

1.2.2 Light-Matter Interaction in Microcavities

We now explore the interaction in detail between the light and matter, especially organic materials, which are placed inside a planar cavity. This will naturally lead to the subject of cavity quantum electrodynamics (QED). The discussion will start from considering the key parameters that determine the properties of the cavity and the magnitude of the matter-cavity coupling, and then introduce various physical effects that are observed in the limits of different coupling regimes.

Optical Microcavities

Consider a planar cavity shown in Fig. 1.2(a), which consists of two plane mirrors M1 and M2, with reflectivities of R_1 and R_2, respectively, separated by an adjustable length L_{cav}. The space between the mirrors is filled with a medium of refractive index n and the mirrors are aligned parallel to each other so that light inside the cavity reflects backwards and forwards between the mirrors. This cavity is called the Fabry-Pérot cavity, and its properties can be analyzed by considering the effect of

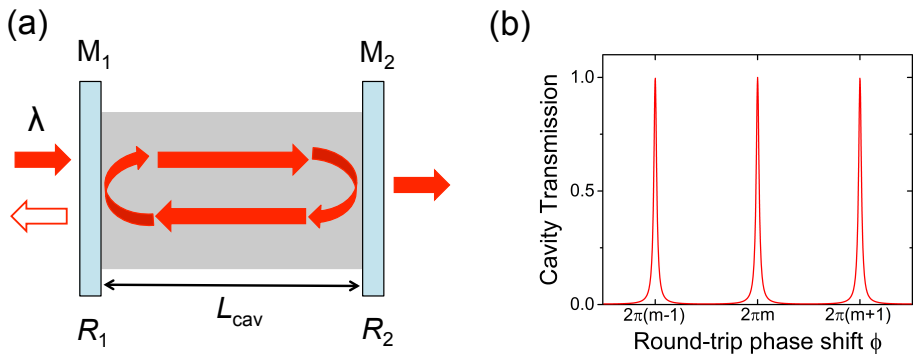

Figure 1.2. (a) A planar cavity of length L_{cav} with two parallel end mirrors M1 and M2 of reflectivity R_1 and R_2, respectively. (b) Transmission of a lossless planar cavity with mirror reflectivities of 90%, giving a finesse $\mathcal{F}$ of 30. Resonance occurs whenever the round-trip phase ϕ equals $2\pi m$, where m is an integer.

introducing light of wavelength λ from one side and calculating how much is transmitted to the other side. On the assumption that there are no absorption or scattering losses within the cavity, the transmission T is given by:

$$T = \frac{1}{1 + (4\mathcal{F}^2/\pi^2)\sin^2(\phi/2)} \tag{1.2}$$

where

$$\phi = \frac{4\pi n L_{cav}}{\lambda} \tag{1.3}$$

is the round-trip phase shift, and

$$\mathcal{F} = \frac{\pi(R_1R_2)^{1/4}}{1 - \sqrt{R_1R_2}} \tag{1.4}$$

is the finesse of the cavity. It is easy to see from Eq. 1.2 that the transmission is equal to unity whenever $\phi = 2\pi m$, where m is an integer. In this situation the cavity is said to be **on-resonance**. From Eq. 1.3 we see that the resonance condition occurs when the cavity length L_{cav} is equal to an integer number m of intracavity half wavelengths:

$$L_{cav} = m\lambda/2n. \tag{1.5}$$

The cavity resonance condition naturally leads to the concept of resonant modes. These are modes of the light field that satisfy the resonance condition and are preferentially selected by the cavity. Fig. 1.2(b) shows the transmission of a lossless planar cavity with $R_1 = R_2 = 0.9$, giving $\mathcal{F} = 30$. The transmission is a sharply peaked function of the round-trip phase shift ϕ, with maxima at the resonance values of $\phi = 2\pi m$, representing the cavity resonant modes. The angular frequencies of the resonant modes can be easily derived from Eq. 1.5:

$$\omega_m = m\frac{\pi c}{nL_{cav}}. \tag{1.6}$$

An analysis of the linear cavity shows that there are basically two key parameters that determine the main properties, namely the resonant mode frequency ω_m and the cavity finesse $\mathcal{F}$. The latter parameter controls both the mode width $\delta\omega$ and the cavity loss rate κ. It is helpful to introduce the **quality factor** (Q) of the cavity, defined by:

$$Q = \frac{\omega}{\delta\omega}. \tag{1.7}$$

This serves the equivalent purpose for an arbitrary optically resonant structure as the finesse does for the planar cavity. It is thus convenient to specify the properties of a cavity either by the frequency and finesse, or equivalently by the frequency and quality factor.

Matter-Cavity Coupling

We can now discuss the interaction between the light inside a cavity and matter, as shown schematically in Fig. 1.3(a). We assume that the matter is inserted in such a way that it can absorb photons from the cavity modes and also emit photons into the cavity by radiative emission. For inorganic semiconductors and organic materials,

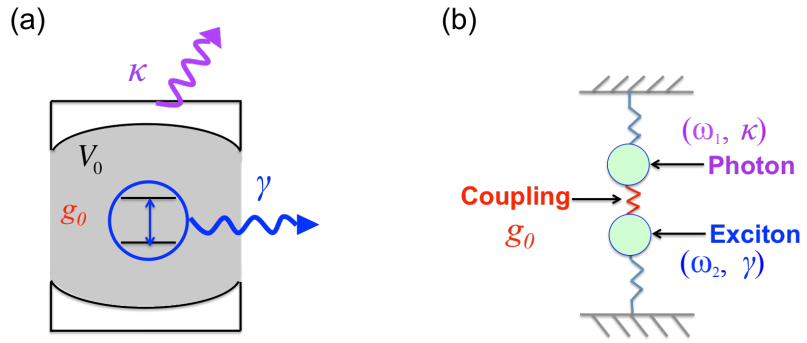

Figure 1.3. (a) Materials with two-level transition dipole moment in a resonant cavity with modal volume V_0. (b) Coupled oscillator model. ω_1 and ω_2 are the nature frequencies of the uncoupled oscillators, and g_0 is the coupling parameter.

a bound state of the electron and hole will be formed when a photon is absorbed, which is termed as exciton. When the transition frequency of excitons coincides with one of the resonant modes of the cavity, the interaction between matter and the light field will be strongly affected, since they can exchange photons in a resonant way. At resonance, the relative strength of the matter-cavity interaction is determined by three parameters:

- the loss rate of photon leaving the cavity κ;
- the non-resonant decay rate γ;
- the matter-cavity coupling parameter g_0.

When the coupling constant g_0 is smaller than the loss rate due to either leakage of photons from the cavity (κ) or decay to non-resonant modes (γ), the interaction is said to be in the weak coupling regime. This means that photons are lost from the matter-cavity system faster than the characteristic interaction time between the material and the cavity. The emission of light by materials in the cavity is therefore irreversible, just as for emission into free space. Since the effect of the cavity is

relatively small in the weak coupling regime, it is appropriate to treat the matter-cavity interaction by perturbation theory. Fermi's Golden Rule states that the rate of spontaneous emission is proportional to the density of photon states at the spatial position of the exciton.[7] Thus, the main effect of the cavity is to enhance or suppress the photon density of states compared to the free-space value, depending on whether the cavity mode is resonant with the exciton transition or not. The radiative lifetime of an exciton in an optical microcavity can either be extended or reduced with respect to its lifetime in vacuum. This phenomenon is known as the Purcell effect,[8] and is a feature of weak exciton-photon coupling.

In contrast, the exciton of materials and photon of the cavity modes may strongly couple if their respective lifetimes are long in comparison to the interaction time between the two particles ($g_0 \gg (\kappa, \gamma)$). In this case, the interaction between the photons in the cavity mode and the exciton of materials is reversible, and a quasi-lossless regime is established wherein the system oscillates coherently between the exciton and cavity photon states. The new eigenstates of the system are referred to as microcavity polaritons.[9–11] The microcavity polariton dispersion curve consists of anti-crossed branches arising from the exciton and photon dispersion separated in energy by the Rabi splitting ($\hbar\Omega_R$). The lifetime condition ($g_0 \gg (\kappa, \gamma)$) is equivalent to stating that the linewidth of the exciton and cavity mode resonance must be smaller than the Rabi splitting.

The Rabi splitting of microcavity polariton in the matter-cavity strongly coupled system can be given a quasi-classical explanation by considering the properties of two coupled classical oscillators as shown in Fig. 1.3(b). If ω_{cav} and ω_{ex} are the natural frequencies of the uncoupled oscillators (i.e. the cavity photon and the exciton), and

g_0 is the coupling parameter, then it can be shown that the frequencies of the coupled modes are given by

$$\omega_{\pm} = \frac{\omega_{cav} + \omega_{ex}}{2} \pm \frac{1}{2}\left(\Omega_R^2 + (\omega_{cav} - \omega_{ex})^2\right)^{1/2}. \tag{1.8}$$

and

$$\Omega_R = 2g_0 = 2\left(\frac{N\mu_{12}^2\omega_{ex}}{2V_0\epsilon\hbar}\right)^{1/2}. \tag{1.9}$$

where ϵ is the dielectric constant of the material, N/V_0 is the number density of atoms/molecules, ω_{ex} is the transition frequency of the uncoupled exciton, and $\mu_{12} \equiv \langle\Psi_1|e\vec{r}|\Psi_2\rangle$ is the electric dipole matrix element of the transition. At resonance, with $\omega_{cav} = \omega_{ex} \equiv \omega$, the frequencies of the coupled modes reduce to:

$$\omega_{\pm} = \omega \pm \frac{\Omega_R}{2}. \tag{1.10}$$

For the above descriptions of the classical coupled oscillator model, the decay rate of cavity photons, κ, and the non-resonant decay rate of excitons, γ, are not considered. In the next section, a full quantum theory for light-matter strong coupling will be discussed, including the consideration of the dissipations within the coupled system.

Quantum Theory for Strong Coupling

In the frame of a quantum mechanical model, both the exciton and the photon are treated as quantum mechanical oscillators. The exciton can be described by a simple two energy level system with the ground state $|g\rangle$ and the excited state $|e\rangle$, and the creation and annihilation operator are $b^\dagger$ and b, respectively. Similarly, the photon is considered as a quantized photonic mode in the cavity, which is created and annihilated by the operator $a^\dagger$ and a, respectively. As illustrated in Fig. 1.4, the strong

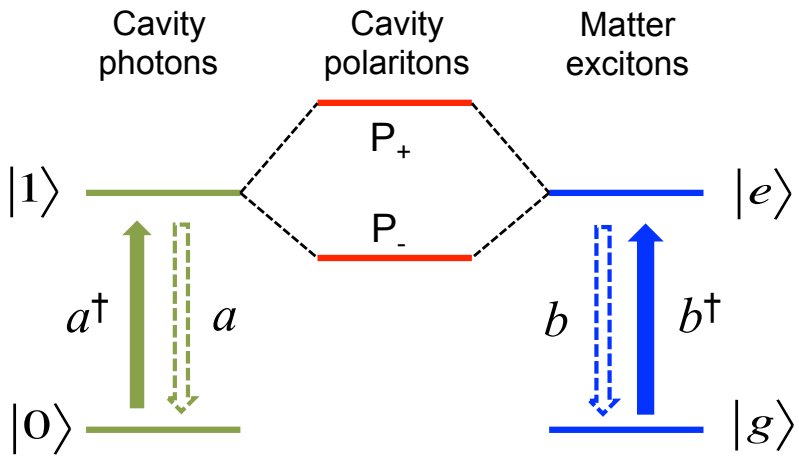

Figure 1.4. Strong coupling between the exciton and cavity photon results in new hybrid states, cavity polaritons. P_+: upper polariton; P_-: lower polariton.

exciton-photon coupling gives rise to new light-matter hybrid states - cavity polaritons, the higher energy state is called upper polariton (P_+), and the lower energy state is called lower polariton (P_-). Within the rotating wave approximation (RWA), the total Hamiltonian of the hybridized system can be written as:[10,11]

$$\hat{H} = \hat{H}_{cav} + \hat{H}_{ex} + \hat{H}_{int} = \hbar\omega_{cav,k} a_k^\dagger a_k + \hbar\omega_{ex,k} b_k^\dagger b_k - i\frac{\hbar\Omega_R}{2}\left(a_k b_k^\dagger - a_k^\dagger b_k\right). \quad (1.11)$$

where subscript index k indicates the momentum of the exciton and photon, and $\hat{H}_{int}$ represents the resonant dipole interaction between the exciton and the quantized radiation field. This is the well-known Jaynes-Cummings model which describes the interaction of a two-level atom/molecule with a single quantized mode of the radiation field in the strong coupling regime.[12] The above Hamiltonian can be easily diagonalized by the following unitary transformation:[10,13]

$$\begin{pmatrix} p_k \\ u_k \end{pmatrix} = \begin{pmatrix} X_k & C_k \\ -C_k^* & X_k^* \end{pmatrix} \begin{pmatrix} b_k \\ a_k \end{pmatrix} \quad (1.12)$$

where u_k and p_k are the upper and lower polariton annihilation operators, X_k and C_k are the Hopfield coefficients to represent the contributions from excitonic and photonic components, respectively, which satisfy the following condition:[14]

$$|X_k|^2 + |C_k|^2 = 1 \tag{1.13}$$

The resulting diagonalized Hamiltonian of the coupled system is given by

$$\hat{H} = E_{LP} p_k^\dagger p_k + E_{UP} u_k^\dagger u_k \tag{1.14}$$

The solution of this Hamiltonian at each wave vector k using energies of uncoupled exciton and cavity mode including the linewidth, $E_{ex,k} + i\gamma_{ex,k}$ and $E_{cav,k} + i\gamma_{cav,k}$, yields

$$\begin{vmatrix} E_{ex,k} + i\gamma_{ex,k} - E & \hbar\Omega_R/2 \\ \hbar\Omega_R/2 & E_{cav,k} + i\gamma_{cav,k} - E \end{vmatrix} = 0 \tag{1.15}$$

with eigenvalues of upper and lower polaritons

$$E^k_{UP,LP} = \frac{E_{cav,k} + E_{ex,k}}{2} + i\frac{\gamma_{cav,k} + \gamma_{ex,k}}{2} \pm \frac{1}{2}\sqrt{(\hbar\Omega_R)^2 + [(E_{cav,k} - E_{ex,k}) + i\,(\gamma_{cav,k} - \gamma_{ex,k})]^2} \tag{1.16}$$

The new modes of the coupled system are described by the real parts of the energy eigenvalue, which can be expressed as a function of detuning between the cavity mode and exciton $\Delta = E_{cav,k} - E_{ex,k}$, and are given by

$$E^k_{UP,LP} = \frac{E_{cav,k} + E_{ex,k}}{2} \pm \frac{1}{2}\sqrt{(\hbar\Omega_R)^2 + \Delta^2} \tag{1.17}$$

where the imaginary part is responsible for the half linewidths of cavity photons and excitons.

At resonance, with $E_{cav,k} = E_{ex,k}$, the upper and lower polariton states are separated by the vacuum Rabi splitting energy, $\hbar\Omega_R$. The Hopfield coefficients X_k and C_k can be expressed in terms of the detuning Δ and the vacuum Rabi splitting energy $\hbar\Omega_R$:

$$\begin{aligned} |X_k|^2 &= \frac{1}{2}\left(1 + \frac{\Delta}{\sqrt{\Delta^2 + (\hbar\Omega_R)^2}}\right) \\ |C_k|^2 &= \frac{1}{2}\left(1 - \frac{\Delta}{\sqrt{\Delta^2 + (\hbar\Omega_R)^2}}\right) \end{aligned} \tag{1.18}$$

At $\Delta = 0$, $|X_k|^2 = |C_k|^2 = \frac{1}{2}$, corresponding that both the upper and lower polariton states are exactly half-photon, half-exciton-like.

Ultrastrong Exciton-Photon Coupling

In the strong coupling limit, the rotating approximation (RWA) neglects the antiresonant and higher interaction terms of the total Hamiltonian for the coupled system. When the vacuum Rabi splitting ($\hbar\Omega_R$) becomes an appreciable fraction of the uncoupled transition energy (E_{ex}) of the exciton, the anti-resonant and higher interaction terms play a more significant role in the hybridized system, and RWA is no longer applicable, thus the system enters the so-called ultrastrong coupling regime (USC). The demonstrations of USC have been realized in both inorganic and organic microcavities, which have provoked many stimulating studies about the modification effect on the properties of the coupled system[15–21]

The full Hopfield-type Hamiltonian of the coupled system in the USC regime is given by[16,19,22]

$$\hat{H} = \hat{H}_{res} + \hat{H}_{anti} + \hat{H}_{A^2} \tag{1.19}$$

and

$$\hat{H}_{res} = \hbar\omega_{cav,k} a_k^\dagger a_k + \hbar\omega_{ex,k} b_k^\dagger b_k - i\frac{\hbar\Omega_R}{2}\left(a_k b_k^\dagger - a_k^\dagger b_k\right) \tag{1.20a}$$

$$\hat{H}_{anti} = i\frac{\hbar\Omega_R}{2}\left(a_k b_{-k} - a_k^\dagger b_{-k}^\dagger\right) + D_k\left(a_k a_{-k} + a_k^\dagger a_{-k}^\dagger\right) \tag{1.20b}$$

$$\hat{H}_{A^2} = \hbar D_k\left(a_k^\dagger a_k + a_k a_k^\dagger\right) \tag{1.20c}$$

where a, b are the photon and exciton annihilation operators, and $a^\dagger$, $b^\dagger$ are the photon and exciton creation operators, respectively. Eq. 1.20(a) describes the Jaynes-Cummings form of the strong-coupling Hamiltonian, Eq. 1.20(b) represents the antiresonant terms, corresponding to the simultaneous creation and annihilation of two excitations with opposite in-plane wave vectors, and Eq. 1.20(c) describes the contribution from the diamagnetic terms, which is proportional to the square of the vector potential (A^2), and gives a renormalization of the photon energy due to the interaction with matter. $D_k = \Omega_R^2/4\omega_{ex}$ is the diamagnetic coupling constant.

The full Hamiltonian in Eq. 1.19 can be diagonalized by introducing polariton annihilation operators

$$p_{j,k} = x_{j,k} a_k + y_{j,k} b_k + z_{j,k} a_{j,-k}^\dagger + w_{j,k} b_{j,-k}^\dagger \tag{1.21}$$

where $j \in [UP, LP]$. The Bose commutation rule

$$\left[p_{j,k}, p_{j',k'}^\dagger\right] = \delta_{j,j'}\delta_{k,k'} \tag{1.22}$$

imposes the normalization condition

$$x_{j,k}^* x_{j',k} + y_{j,k}^* y_{j',k} - z_{j,k}^* z_{j',k} - w_{j,k}^* w_{j',k} = \delta_{j,j'} \tag{1.23}$$

Therefore, the eigenvectors can be written as:

$$\vec{v}_{j,k} = (x_{j,k}, y_{j,k}, z_{j,k}, w_{j,k})^T \tag{1.24}$$

which satisfy the eigenvalue equation:

$$M_k \vec{v}_{j,k} = \omega_{j,k} \vec{v}_{j,k} \tag{1.25}$$

The full Hamiltonian matrix M_k of the ultrastrongly coupled system is given by[19,22]

$$M_k = \begin{pmatrix} \omega_{cav,k} + 2D_k & -i\Omega_R/2 & -2D_k & -i\Omega_R/2 \\ i\Omega_R/2 & \omega_{ex,k} & -i\Omega_R/2 & 0 \\ 2D_k & -i\Omega_R/2 & -\omega_{cav,k} - 2D_k & -i\Omega_R/2 \\ -i\Omega_R/2 & 0 & -i\Omega_R/2 & -\omega_{ex,k} \end{pmatrix} \tag{1.26}$$

Let us discuss one of the important features of the ultrastrongly coupled system, starting from defining $|g\rangle|0\rangle$ as the ground state of the uncoupled light-matter system, which satisfies that

$$a_k|g\rangle|0\rangle = b_k|g\rangle|0\rangle = 0 \tag{1.27}$$

Applying the polariton annihilation operator given by Eq. 1.21, yields

$$p_{j,k}|g\rangle|0\rangle \neq 0 \tag{1.28}$$

which suggests that the coupling modifies the ground state. A new ground state of the coupled system is defined as $|GS\rangle$, satisfying that $p_{j,k}|GS\rangle = 0$. Then, we have

$$\begin{aligned} \langle GS|a_k^\dagger a_k|GS\rangle &= |z_{LP,k}|^2 + |z_{UP,k}|^2 \\ \langle GS|b_k^\dagger b_k|GS\rangle &= |w_{LP,k}|^2 + |w_{UP,k}|^2 \end{aligned} \tag{1.29}$$

Eq. 1.29 shows that the ground state of the coupled system contains a finite number of cavity photons and excitons. Also, note that the ground state of the system has

shifted by ΔG with respect to the uncoupled ground state, which is neglected in the RWA, and can become significant as the relative coupling strength (Ω_R/ω_{ex}) is increased[22,23]

$$\Delta G = \omega_{ex}\left(1 - \sqrt{1 + \left(\frac{\Omega_R}{2\omega_{ex}}\right)^2}\right) \tag{1.30}$$

Classification for Coupling Regimes

The light-matter coupling regimes could be classified by comparing parameter magnitudes of (Γ, Ω_R), where Γ is the loss rate of the system, and Ω_R is the vacuum Rabi splitting frequency, a parameter of coupling strength. Investigating the relative coupling strength (Ω_R/ω_{ex}) of the system, the classification of light-matter interaction regimes is illustrated in Fig. 1.5.

- *Weak coupling*: when $\Omega_R < \Gamma$, then the weak light-matter interaction can be treated as a perturbation term, and Fermi's Golden Role will appropriately describe the evolution of the system;
- *Strong and ultrastrong coupling*: when $\Omega_R > \Gamma$, the light-matter interaction can not be treated as a perturbation term, and is strong enough to result in new eigenstates known as cavity polaritons for microcavities, and strong coupling is achieved. Typically, if $\Omega_R/\omega_{ex} > 0.2$, the system thus enters the ultrastrong coupling regime.[19]
- *Deep strong coupling*: when $\Omega_R/\omega_{ex} > 1$, some counterintuitive phenomena are predicted by new theoretical investigations, such as the breakdown of the Purcell effect,[24] and this light-matter coupling regime is usually termed as deep strong coupling (DSC), which has not been experimentally observed yet. DSC is beyond the scope of this thesis, and interested readers are referred to literature on this topic.[24–27]

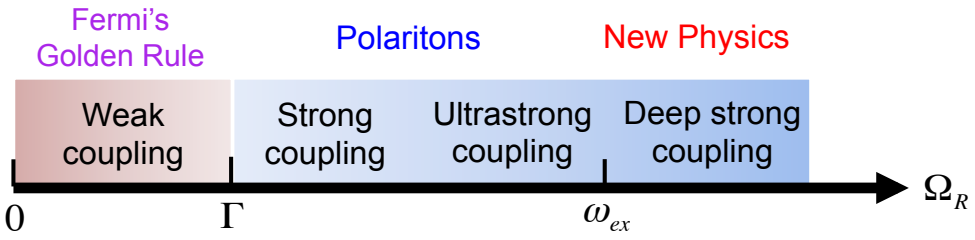

Figure 1.5. Classification for different light-matter coupling regimes regarding the vacuum Rabi frequency Ω_R. Γ: Loss rate; ω_{ex}: uncoupled exciton transition frequency.

1.3 Introduction to Nonlinear Optics

Nonlinear optics is the study of phenomena that occur as a consequence of the modification of the optical properties of a material system by the presence of light.[28] Typically, coherent intense laser light can be sufficient to modify the optical properties of a material system, yielding the nonlinear optical effects. Importantly, organic cavity polariton, as a quasiparticle formed from strong exciton-photon coupling, exhibits significant additional nonlinearity, which will be comprehensively investigated in Chapter 3. The beginning of the field of nonlinear optics is often taken to be the discovery of second-harmonic generation (SHG) by Franken *et al.* in 1961,[29] shortly after the demonstration of the first working laser by Maiman in 1960.[30] Later, Terhune and his coworkers demonstrated third-harmonic generation (THG) with a calcite crystal in 1962.[31] Until now, a large number of nonlinear optical processes have been extensively studied, for example, stimulated Raman scattering,[32] stimulated Brillouin Scattering,[33] Hyper Rayleigh Scattering,[34] optical Kerr effect,[35] self-focussing,[36] two-photon absorption,[37] etc. In this thesis, I will focus on the SHG and THG, and investigate the nonlinear optical response of multilayer organic nanostructures.

Under an electric field provided by the intense coherent laser, the positive and negative charges inside the nonlinear molecules can create a relative displacement to each other, resulting in an induced polarization **P** (dipole moment per unit volume). The nonlinear induced polarization is the origin of the nonlinear optical response, which can be expressed as a power series of the electric field strength **E**:

$$P_i = \chi_{ij}^{(1)} E_j + \chi_{ijk}^{(2)} E_j E_k + \chi_{ijkl}^{(3)} E_j E_k E_l + \cdots \tag{1.31}$$

where E_i $(i = x, y, z)$ are the Cartesian components of the electric field, $\chi_{ij}^{(1)}$ is the linear susceptibility, which determines the linear optical properties of the materials. In an isotropic material, the second-rank tensor, $\chi_{ij}^{(1)}$, becomes a scalar (χ) times the unit matrix. Thus, the dielectric constant of the isotropic material can be given by

$$\epsilon = n^2 = 1 + \chi \tag{1.32}$$

For an anisotropic material, the dielectric constant (ϵ) or the index of refraction (n) is a second-rank tensor, and the birefringence arises from the anisotropic dielectric constant.

The high-order terms in Eq. 1.31 represent the nonlinear optical response of the materials. The third-rank tensor, $\chi_{ijk}^{(2)}$, is known as the second-order nonlinear optical susceptibility. In general, the nonlinear susceptibilities depend on the frequencies of the applied fields, thus the first nonlinear term in Eq. 1.31 can be written as

$$P_i^{(2)}(\omega_3) = \chi_{ijk}^{(2)}(\omega_3; \omega_1, \omega_2) E_j(\omega_1) E_k(\omega_2) \tag{1.33}$$

Specifically, for $\chi^{(2)}(2\omega; \omega, \omega)$ with $\omega_1 = \omega_2 = \omega$ and $\omega_3 = 2\omega$, Eq. 1.33 describes the process of second-harmonic generation, which is illustrated schematically in Fig. 1.6,

and two photons of frequency ω are destroyed, and a photon of frequency 2ω is simultaneously created in a single quantum-mechanical process.

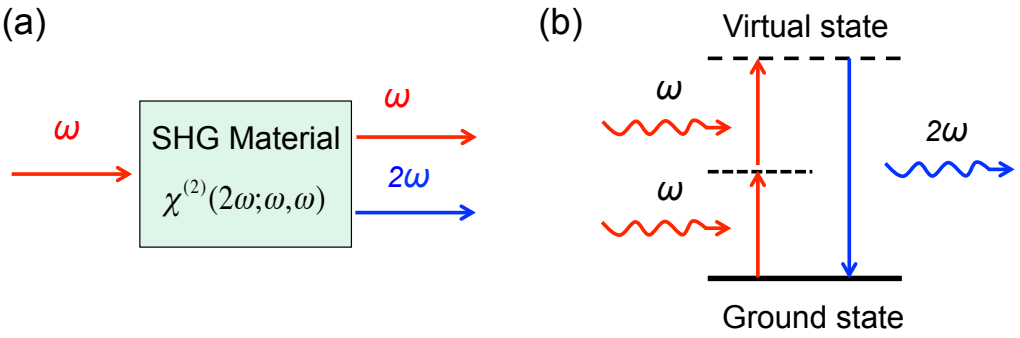

Figure 1.6. (a) Schematic diagram of second-harmonic generation. (b) Energy-level diagram describing second-harmonic generation.

It is known that the second-order nonlinearity vanishes if the material has an inversion center, which satisfies that $\vec{P} \to -\vec{P}$ for $\vec{E} \to -\vec{E}$. Also, we notice that Eq. 1.33 is unchanged for $\vec{E} \to -\vec{E}$. Therefore, we have

$$\vec{P} = -\vec{P} \tag{1.34}$$

which can occur only if $\vec{P}$ vanishes identically. This result shows that $\chi^{(2)} = 0$.

In Eq. 1.31, the fourth-rank tensor, $\chi^{(3)}_{ijkl}$, represents the third-order nonlinear optical susceptibility, and it is always nonzero. Thus, the third-order nonlinear optical interactions described by a $\chi^{(3)}$ susceptibility can occur for both centrosymmetric and noncentrosymmetric materials. Analogously, this nonlinear term is can be written as

$$P_i^{(3)}(\omega_4) = \chi^{(3)}_{ijkl}(\omega_4;\omega_1,\omega_2,\omega_3)E_j(\omega_1)E_k(\omega_2)E_l(\omega_3) \tag{1.35}$$

When $\omega_1 = \omega_2 = \omega_3 = \omega$ and $\omega_4 = 3\omega$, the above nonlinear term leads to the process of third-harmonic generation shown in Fig. 1.7, where three photons of frequency ω are destroyed and one photon of frequency 3ω is created in the microscopic description

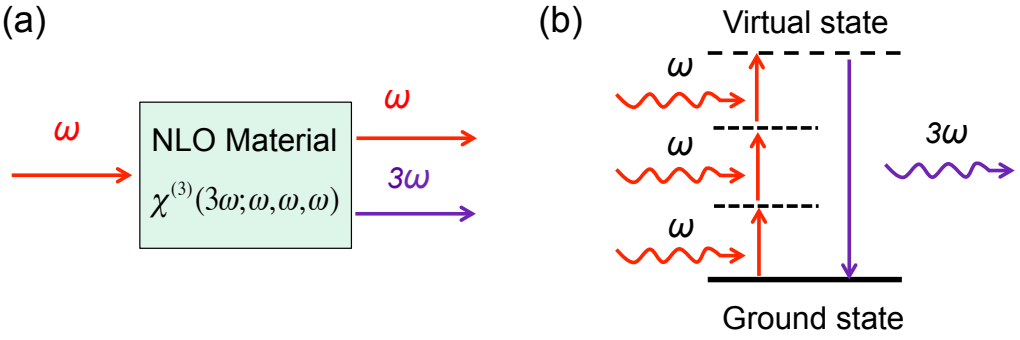

Figure 1.7. (a) Schematic diagram of third-harmonic generation. (b) Energy-level diagram describing third-harmonic generation.

1.4 Introduction to Perovskite Photovoltaics

1.4.1 Overview of Photovoltaics and Perovskite Photovoltaics

The growing world energy demand has motivated people to seek for new alternatives to conventional fossil resources. Solar energy is one of the best available alternatives, for it is both abundant and clean. Since the photovoltaic (PV) effect was discovered in silicon (Si) diodes,[38] photovoltaic technology, which generates electricity directly from sunlight, has become a promising solution to the energy crisis. Currently, various inorganic materials, for example, Si, III-V group semiconductors, CdTe, and copper indium gallium selenide (CIGS), based PV devices are the dominating technologies in the market worldwide,[39], and the device efficiency is approaching the Shockley-Queisser limit, which is referred to as the maximum theoretical efficiency of a solar cell using a single p-n junction to collect power from the cell.[40,41]

To further increase the efficiency, lower the processing cost, and achieve roll-to-roll processability for large area devices and mechanical flexibility, a large number of new technologies based on various materials have been developed with efforts of workers from both commercial enterprises and academic research labs. The National Center

for Photovoltaics (NCPV) at the National Renewable Energy Laboratory (NREL) maintains a plot of compiled values of highest confirmed conversion efficiencies for research cells, from 1976 to the present, for a range of photovoltaic technologies, which is shown in Fig. 1.8. Recently, perovskite photovoltaic materials have rapidly achieved efficiencies comparable to Si photovoltaic devices as shown in the lower right of Fig. 1.8. This newest PV technology is considered in this thesis, incorporating a perovskite structured compound, most commonly a hybrid organic-inorganic halide material, as the light-harvesting active layer.

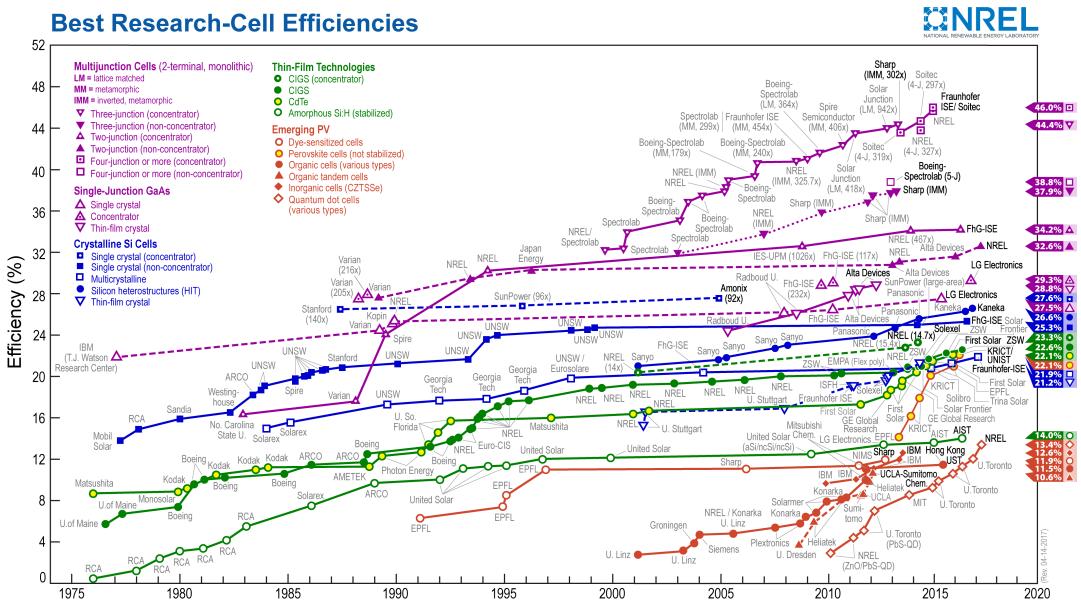

Figure 1.8. Certified efficiency of Certified efficiency of lab solar cells from 1976 to the present. This plot is courtesy of the National Renewable Energy Laboratory, Golden, CO.

Organic-inorganic perovskites $CH_3NH_3PbX_3$ (X=Br and I) were first used as a semiconductor sensitizer in dye-sensitized liquid junction-type solar cells, which led to the power conversion efficiency (PCE) of 3-4% in 2009.[42] However, due to the low photovoltaic performance and extreme instability, little attention has been focused

on the perovskite photovoltaics until the development of a long-term stable solid-state perovskite solar cell yielding a PCE of 9.7%.[43] Since then, rapid progress has been made, and a certified record PCE of 22.1% was demonstrated in 2016. With the potential of achieving even higher efficiencies and the very low production costs, perovskite solar cells have become commercially attractive, with start-up companies already promising modules on the market by 2017.[44,45]

1.4.2 Operating Principles of Solar Cells

The process of conversion of light into electricity by solar cells, illustrated in Fig. 1.9(a), can be schematically described by the following steps:

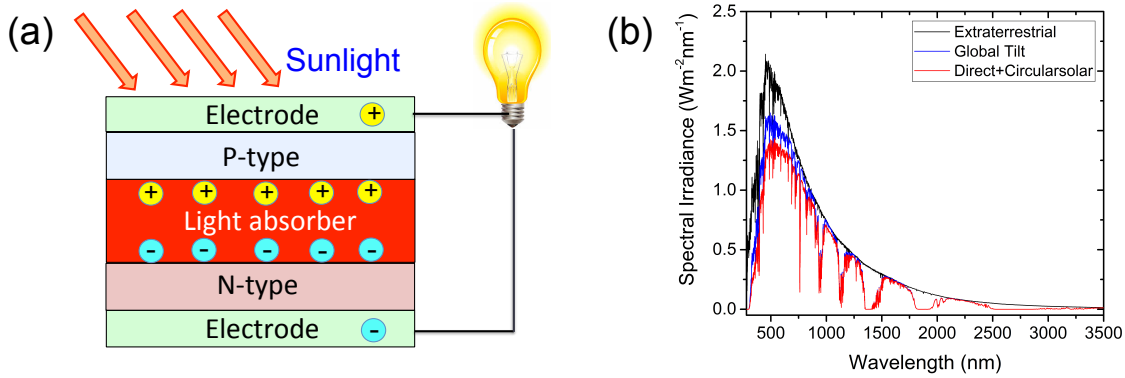

Figure 1.9. (a) Schematic representation of a photovoltaic device. (b) NREL standard solar irradiance spectra depicting the solar spectrum before passing through the Earths atmosphere (extraterrestrial), after traversing 1.5 standard air-mass (direct+circumsolar), and incident upon surface tilted at 37^o towards the equator (global tilt).

- *Light harvest and charge-carrier generation*: the absorption of light by the photoactive layer of material leads to the formation of an excited state, the bound electron-hole pair (exciton). To achieve a high device efficiency, large light harvesting is required in the solar spectrum (Fig. 1.9b).

- *Charge-carrier separation*: the primary photoexcitations in active materials do not directly and quantitatively lead to free charge-carriers but to coulombically bound electron-hole pairs, called excitons. When the binding energy of exciton is much smaller than kT, where k is Boltzmann constant and T is room temperature, then electron-hole pairs dissociate. For excitons with large binding energies, such as Frenkel excitons in organic materials, strong electric fields are necessary for efficient dissociation of excitons, which can be supplied via externally applied electrical fields as well as via interfaces. At an interface, where abrupt changes of the potential energy occur, strong local electrical fields are possible ($\vec{E} = -\nabla U$).[46] Photoinduced charge transfer can occur when the exciton has reached such an interface within its lifetime. Otherwise, excitons decay via radiative or nonradiative path ways before reaching the interface, and their energy is lost for the power conversion.
- *Charge-carrier transport*: for efficient photovoltaic devices, the created free charges need to be transported to the appropriate electrodes within their lifetime. The charge-carriers need a driving force to reach the electrodes. A gradient in the chemical potentials of electrons and holes (quasi Fermi levels of the doped phases) is built up in a p-n/donor-acceptor junction. This chemical potential gradient determines the maximum open circuit voltage (V_{OC}) and contributes to a field-induced drift of charge-carriers. Also, using asymmetrical contacts (one low work-function electrode for the collection of electrons and one high work-function electrode for the collection of the holes) leads to an external field for improving charge transport as that in a p-n junction diode.[47] To further improve the charge transport and impede the electron-hole recombination during the journey to the electrodes,

a hole-transporting layer (p-type) and an electron-transporting layer (n-type) are incorporated in the device structure, which are shown in Fig. 1.9(a).

- *Charge-carrier collection*: charge-carriers are extracted from the device through two selective contacts with optimal conductivity and appropriate work function.

Characterization of a Solar Cell Device

The characteristics of a PV device are determined by current-voltage curves. For the dark characteristics of the solar cell in the absence of light, the sign and value of the applied voltage determines blocking and conducting regimes. The cell conducts when the voltage exceeds a threshold V_S. An ideal cell can follow the thermionic injection model:

$$I = I_S \left(\exp\left(\frac{eV}{k_B T} \right) - 1 \right) \tag{1.36}$$

where I_S is the saturation current under reverse bias.

Under light illumination, the ideal current in the circuit is modeled as

$$I = I_S \left(\exp\left(\frac{eV}{k_B T} \right) - 1 \right) - I_L \tag{1.37}$$

where I_L originates from charge generation by the illumination.

In real devices, the circuit must be modified to account for series R_S and shunt R_{SH} resistance losses, and R_L is the charge resistance of the external circuit. An 'ideality factor' n is also introduced (it is 1 for an ideal diode). Currents becomes determined by the following equation:[48]

$$I \left(1 + \frac{R_S}{R_{SH}} \right) - \frac{V}{R_{SH}} + I_L = I_S \left(\exp\left(\frac{e}{n k_B T} \left(V - I R_S \right) \right) - 1 \right). \tag{1.38}$$

Now, two important characteristic quantities of solar cells are introduced: (1) the short circuit current I_{SC} is the one which crosses the cell at zero applied voltage, it

is a function of illumination G; (2) the open circuit voltage V_{OC} is measured when current in the cell is 0, corresponding to almost flat valence and conduction bands. The relation between V_{OC} and I_{SC} can be determined when it is assumed that $R_S = 0$ and $R_{SH} = \infty$, with $I = 0$ and $I_L = I_{SC}$:

$$V_{OC} = \frac{nk_BT}{e} \ln\left(\frac{I_{SC}}{I_S} + 1\right) \tag{1.39}$$

Therefore, the current-voltage characteristics of a solar cell in the dark and under

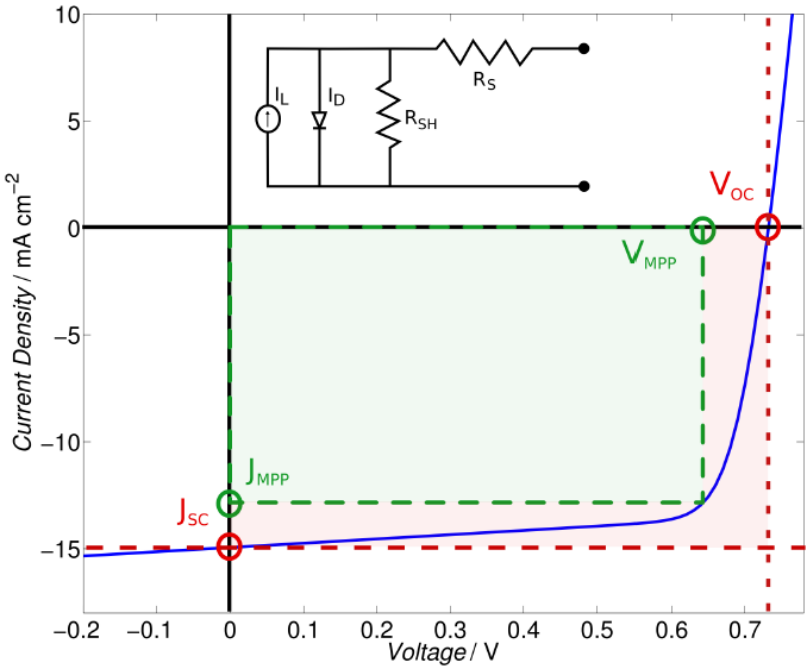

Figure 1.10. A typical J-V curve of a solar cell under illumination.[49] V_{OC}: open circuit voltage, J_{SC}: short circuit current density, V_{MPP}: maximum power point voltage, J_{MPP}: maximum power point current density. Inset: equivalent circuit of a solar cell.

illumination permits an evaluation of most of its photovoltaic performance as well as its electric behavior. Fig. 1.10 shows a typical current density (J)-voltage (V) curve of a solar cell under illumination,[49] where the characteristic intersections with the abscissa and ordinate are the open circuit voltage (V_{OC}) and the short circuit current

density (J_{SC}), respectively. At maximum power point (MPP), the product of current density (J_{MPP}) and voltage (V_{MPP}) is the largest. Thus, a fill factor FF can be defined as:

$$FF = \frac{V_{MPP} \times J_{MPP}}{V_{OC} \times J_{SC}} \tag{1.40}$$

The fill factor is largely determined by the series and shunt resistances, and incorporates many possible defects in the material and fabrication quality. Finally, the photovoltaic power conversion efficiency of a solar cell is determined by

$$\eta = FF \frac{V_{OC} \times J_{SC}}{P_{in}} \tag{1.41}$$

where P_{in} is the incident light power density. This light intensity is standardized at 1000 W/m^2 with a spectral intensity distribution matching that of the sun on the earth's surface at an incident angle of 48.2^o, which is called the AM 1.5 spectrum.[50]

1.4.3 3D and 2D Perovskite Photovoltaics

Properties of 3D Perovskite Photovoltaics

Perovskites are a family of materials with the crystal structure of calcium titanate, that is, ABX_3 shown in Fig. 1.11(a). In organic-inorganic halide perovskite of interest in photovoltaic applications, A is a larger organic cation typically methylammonium $CH_3NH_3^+$ (MA), while ethylammonium $CH_3CH_2NH_3^+$ (EA) and formamidinium $HC(NH_2)_2^+$ (FA) are also used in the perovskite compound for photovoltaics.[51,52] Anion X is a halogen (Cl, Br and I), and as cation B, Pb and Sn have exclusively been used for high efficiency perovskite solar cells because of lower and theoretically ideal band gaps. Thus, the standard three-dimensional (3D) perovskite compound for photovoltaics is methylammonium lead triiodide ($CH_3NH_3PbI_3$), with mixed halides $CH_3NH_3PbI_{3-x}Cl_x$ and $CH_3NH_3PbI_{3-x}Br_x$ also being important.[53]

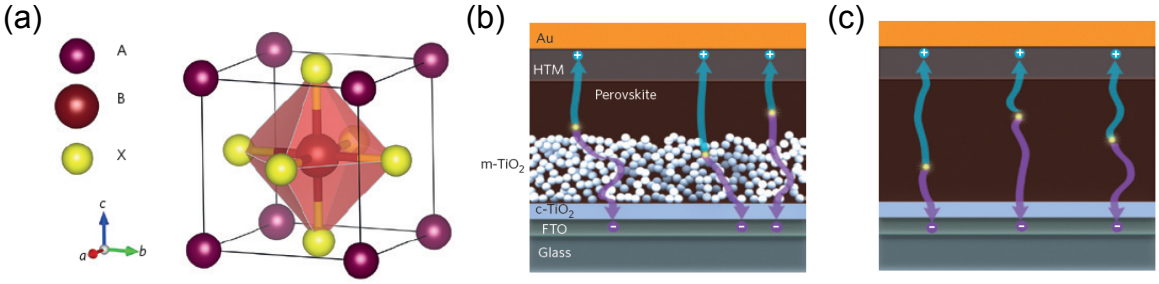

Figure 1.11. (a) Perovskite ABX_3 crystal structure. (b) Mesoscopic perovskite solar cell (c) planar heterojunction structure.[60]

The high power conversion efficiencies (PCE) of organometallic halide perovskite solar cells arise from the remarkable properties of perovskite materials:

- *Broad absorption spectra and large absorption coefficients*: the organometallic halide perovskite typically exhibits broad absorption spectra from 350 nm to 800 nm, which can be modified by tuning the bandgap via chemical modification.[54] The absorption coefficients of perovskite thin films are as high as $10^4 - 10^5$ cm^{-1}, which are comparable to that of conventional photovoltaic materials, such as GaAs, CdTe, and CIGS.[55] These optical properties make the organometallic halide perovskite as suitable light absorber for photovoltaics.
- *Small exciton binging energy*: the values of the exciton binding energy of organometallic halide perovskite are in the range of $1 - 10$ meV, which are determined from direct spectroscopic measurement at room temperature,[56,57] owing to the large effective dielectric constants. Thus, as a result of the small exciton binding energy, free charges are generated spontaneously following light absorption.
- *Large charge carrier mobility and diffusion length*: the free electrons and holes both have high mobilities in the range of $10 - 30$ cm^{2}V^{-1}s^{-1}, which are much larger than that in organic solar cells, and the charge carrier diffusion length at solar (AM 1.5)

irradiation can be several hundreds of nanometers.[58,59] Therefore, the large charge carrier diffusion length plays a key role in achieving the remarkable performance of perovskite photovoltaics.

- *Large open circuit voltage* V_{OC}: perovskite solar cells are quite effective in generating a high electric voltage, which is represented by a large V_{OC} of over 1 V.

Based upon the unique properties of perovskites, two typical structures can be constructed: the mesoscopic nanostructures (Fig. 1.11b) with a mesoporous TiO_2 layer, which acts as a scaffold for carrying the photoactive layer, and the planar heterojunction structure (Fig. 1.11c).[60] The latter architecture is relatively simple, and can lead to higher device efficiency than the former, which results from the smaller recombination rate for the planar structure compared with the mesoscopic structure.[61]

Challenges of 3D Perovskite Photovoltaics

- **Hysteresis**. Perovskite solar cells exhibit an anomalous hysteresis in the current-voltage curves.[62,63] The origin of this phenomenon is not yet understood but a number of possible causes have been proposed, with the two most supported notions being ferroelectricity or the presence of mobile ionic species.[64,65] It appears that most evidence is pointing towards mobile ionic species being responsible: under an applied electric field, negative ionic species will migrate towards one electrode and positive ionic species will migrate towards the other. This will enable the stabilization of positive electronic space charge near one electrode and negative electronic space charge near the other, equivalent to p- and n-doping of the perovskite near the charge collection layers. For forward bias, this results in favorable electronic

contact for charge extraction but for reverse bias (or short-circuit) this results in unfavorable electronic contact for charge extraction.[60,64,65]

- **Operational Stability**. When the perovskite solar cells based on 3D $MAPbX_3$ are aged under sunlight without encapsulation the devices usually rapidly degrade. It is most likely that the moisture in the atmosphere reacting with the perovskite under sunlight decomposes the perovskite crystal. Therefore, the necessary encapsulation will increase the cost and complexity of large-scale manufacture of perovskite solar cells. In addition to sustaining prolonged exposure to sunlight in the atmosphere, the solar cells need to be able to survive long-time operation under temperatures as high as 85 °C, and as low as −40 °C.[60] To fabricate long-term stable solar cells and modules, it is thus critical to overcome the moisture- and thermal-driven degradation of perovskite absorbers.

2D Perovskite Photovoltaics

Two-dimensional (2D) perovskites are promising candidate materials, compared to 3D perovskites, which can overcome stability issue. 2D perovskites are derivatives of $MAPbI_3$, obtained by opening the 3D network and inserting long-chain hydrocarbon cations between the perovskite layers. These materials form 2D layered structures and can be considered as naturally occurring multiple quantum wells (QW), where the thickness of the inorganic slab (m) defines the QW width, and the organic spacer acts as the barrier. 2D perovskite solar cells have shown greatly improved environmental stability and photostability under operating conditions.[66–68] However, this type of PV devices lead to smaller photovoltaic efficiencies in comparison to their three-dimensional counterparts, which could contribute to the higher charge-carrier

recombination rates in 2D perovskite solar cells, and I will discuss this with more details in Chapter 4.

To improve photovoltaic performance of 2D perovskite photovoltaic devices and investigate the loss mechanism of device efficiencies, a comprehensive optical modeling of 2D perovskite solar cells will be exploited in this thesis, which can be briefly described as follows:

(I). Cavity enhanced absorption for 2D perovskite photovoltaics

The optical absorption spectra of the photovoltaic materials can be tuned by the cavity effect in the multilayer structure, which has been used to improve device performance for organic photovoltaics.[69,70] Control of absorption spectra of the active layer is achieved simply by controlling thicknesses of the layers within the device; a much easier method than synthesizing new photovoltaic materials. In this thesis, I will explore how the cavity effect tunes the absorption spectra of 2D perovskites within the multilayer structure, and employ this phenomenal optical effect to raise the light harvest in devices, which is critical to improve the photovoltaic performance of solar cells.

(II). Drift-diffusion model for charge-carrier recombination

To investigate the mechanism of charge-carrier recombination in 2D perovskite solar cells, a modified drift-diffusion model will be introduced, which can be used to understand the lower power conversion efficiency (PCE) comparing to that of 3D perovskite solar cells.

1.5 Summary and Thesis Outline

Light-matter interacting multilayer nanostructures provide a promising platform for both fundamental theory development and optical/optoelectrical application. Considering the different multilayer nanostructures investigated, this thesis can be roughly broken into three sections. In the first section (Chapters 2 and 3), I will describe the linear and nonlinear optical properties of ultrastrongly exciton-photon coupled organic cavities containing a well-researched conjugated organic glass. In the next (Chapter 4), the optical modeling of 2D perovskite solar cells will be discussed for a typical photovoltaic multilayered structure. Finally, in the third section (Chapter 5), I will present the nonlinear optical properties of coextruded-multilayered polymer films containing a nonlinear chromophore.

In the following chapters, I will cover the topics, both theoretically and experimentally, listed below with details:

- **Ultrastrong Exciton-Photon Coupling in Single and Double Low-Q Organic Cavities**
- **Cavity-Polariton Enhanced Third-Harmonic Generation in Organic Cavities**
- **Optical Properties and Modeling of 2D Perovskite Solar Cells**
- **Nonlinear Optical Properties of Coextruded-Multilayered Polymer Films**

References

[1] A. R. Parker and H. E. Townley, "Biomimetics of photonic nanostructures," Nat. nanotechnol. **2**, 347 (2007).

[2] K. D. Singer, T. Kazmierczak, J. Lott, H. Song, Y. Wu, J. Andrews, E. Baer, A. Hiltner, and C. Weder, "Melt-processed all-polymer distributed Bragg reflector laser," Opt. Express **16**, 10358 (2008).

[3] P. M. Kaminski, F. Lisco, and J. M. Walls, "Multilayer broadband anti-reflective coating for more efficient thin film solar cells," IEEE J. Photovoltaics **4**, 452 (2014).

[4] L. El Chaar, L. A. Iamont, and N. El Zein, "Review of photovoltaic technologies," Renew. Sustainable Energy Rev. **15**, 2165 (2011).

[5] M. Fox, "Quantum Optics: An Introduction," Oxford University Press, (2006).

[6] T. W. Ebbesen, H. J. Lezec, H. F. Ghaemi, T. Thio, and P. A. Wolff, "Extraordinary optical transmission through sub-wavelength hole arrays," Nature **391**, 667 (1998).

[7] H. Yokoyama, Y. Nambu, T. Kawakami, in: E. Burstein, and C. Weisbuch (Eds.), "Confined Electrons and Photons: New Physics and Applications," Plenum Press, New York, (1995).

[8] E. M. Purcell, "Spontaneous emission probabilities at radio frequencies," Phys. Rev. **69**, 681 (1946).

[9] C. Weisbuch, M. Nishioka, A. Ishikawa, and Y. Arakawa, "Observation of the coupled exciton-photon mode splitting in a semiconductor quantum microcavity," Phys. Rev. Lett. **69**, 3314 (1992).

[10] V. Savona, L. C. Andreani, P. Schwendimann, and A. Quattropani, "Quantum well excitons in semiconductor microcavities: Unified treatment of weak and strong coupling regimes," Solid State Commun. **93**, 733 (1995).

[11] M. S. Skolnick, T. A. Fisher, and D. M. Whittaker, "Strong coupling phenomena in quantum microcavity structures," Semicond. Sci. Technol. **13**, 645 (1998).

[12] E. T. Jaynes and F. W. Cummings, "Comparison of quantum and semiclassical radiation theories with application to the beam maser," Proc. IEEE **51**, 89 (1963).

[13] X. Liu, "Control of Exciton Photon Coupling in Nano-structures," Thesis pp. 25-27 (2014).

[14] J. J. Hopfield, "Theory of the contribution of excitons to the complex dielectric constant of crystals," Phys. Rev. **112**, 1555 (1958).

[15] G. Güniter, A. A. Anappara, J. Hees, A. Sell, G. Biasiol, L. Sorba, S. De Liberato, C. Ciuti, A. Tredicucci, A. Leitenstorfer, and R. Huber, "Sub-cycle switch-on of ultrastrong light-matter interaction," Nature **458**, 178 (2009).

[16] A. A. Anappara, S. De Liberato, A. Tredicucci, C. Ciuti, G. Biasiol, L. Sorba, and F. Beltram, "Signatures of the ultrastrong light-matter coupling regime," Phys. Rev. B **79**, 201303(R) (2009).

[17] Y. Todorov, A. M. Andrews, R. Colombelli, S. De Liberato, C. Ciuti, P. Klang, G. Strasser, and C. Sirtori, "Ultrastrong light-matter coupling regime with polariton dots," Phys. Rev. Lett. **105**, 196402 (2010).

[18] T. Schwartz, J. A. Hutchison, C. Genet, and T. W. Ebbesen, "Reversible switching of ultrastrong light-molecule coupling," Phys. Rev. Lett. **106**, 196405 (2011).

[19] S. Kéna-Cohen, S. A. Maier, and D. D. C. Bradley, "Ultrastrongly coupled exciton-polaritons in metal-clad organic semiconductor microcavities," Adv. Opt. Mater. **1**, 827 (2013).

[20] S. Gambino, M. Mazzeo, A. Genco, O. Stefano, S. Savasta, S. Patanè, D. Ballarini, F. Mangione, G. Lerario, D. Sanvitto, and G. Gigli, "Exploring light-matter interaction phenomena under ultrastrong coupling regime," ACS Photonics **1**, 1042 (2014).

[21] B. Liu, P. Rai, J. Grezmak, R. J. Twieg, and K. D. Singer, "Coupling of exciton-polaritons in low-Q coupled microcavities beyond the rotating wave approximation," Phys. Rev. B **92**, 155301 (2015).

[22] C. Ciuti and G. Bastard, "Quantum vacuum properties of the intersubband cavity polariton field," Phys. Rev. B **72**, 115303 (2005).

[23] S. Wang, "Strong light-molecule coupling: routes to new hybrid materials," Thesis pp. 27-28 (2015).

[24] S. De Liberato, "Light-matter decoupling in the deep strong coupling regime: the breakdown of the Purcell effect," Phys. Rev. Lett. **112**, 016401 (2014).

[25] M. Bamba and T. Ogawa, "System-environment coupling derived by Maxwell's boundary conditions from the weak to the ultrastrong light-matter-coupling regime," Phys. Rev. A **88**, 013814 (2013).

[26] J. Casanova, G. Romero, I. Lizuain, J. J. Garca-Ripoll, and E. Solano, "Deep strong coupling regime of the Jaynes-Cummings model," Phys. Rev. Lett. **105**, 263603 (2010).

[27] D. Hagenmüller, S. De Liberato, and C. Ciuti, "Ultrastrong coupling between a cavity resonator and the cyclotron transition of a two-dimensional electron gas in the case of an integer filling factor," Phys. Rev. B **81**, 235302 (2010).

[28] R. W. Boyd, "Nonlinear Optics," Academic Press, 3rd Edition (2008).

[29] P. A. Franken, A. E. Hill, C. W. Peters, and G. Weinreich, "Generation of optical harmonics," Phys. Rev. Lett. **7**, 118 (1961).

[30] T. H. Maiman, "Stimulated optical radiation in ruby," Nature **187**, 493 (1960).

[31] R. W. Terhune, P. D. Maker, and C. V. Savage, "Optical harmonic generation in calcite," Phys. Rev. Lett. **8**, 404 (1962).

[32] E. J. Woodbury and W. K. Ng, "Ruby laser operation in the near IR," Proc. IRE **50**, 2367 (1962).

[33] R. Y. Chiao, C. H. Townes, and B. P. Stoicheff, "Stimulated Brillouin scattering and coherent generation of intense hypersonic waves," Phys. Rev. Lett. **12**, 592 (1964).

[34] R. W. Terhune, P. D. Maker, and C. M. Savage, "Measurements of nonlinear light scattering," Phys. Rev. Lett. **14**, 681 (1965).

[35] R. Righini, "Ultrafast optical Kerr effect in liquids and solids," Science **1386**, 681 (1993).

[36] R. Y. Chiao, E. Garmire, and C. H. Townes, "Self-trapping of optical beams," Phys. Rev. Lett. **13**, 479 (1964).

[37] M. Kaiser and C. G. B. Garrett, "Two-photon excitation in CaF_2: Eu^{2+}," Phys. Rev. Lett. **7**, 229 (1961).

[38] D. M. Chapin, C. S. Fuller, and G. L. Pearson, "A new silicon p-n Junction photocell for converting solar radiation into electrical power," J. Appl. Phys. **25**, 676 (1954).

[39] M. A. Green, K. Emery, Y. Hishikawa, W. Warta, and E. D. Dunlop, "A new silicon p-n Junction photocell for converting solar radiation into electrical power," Prog. Photovolt. Res. Appl. **20**, 12 (2012).

[40] B. Parida, S. Iniyan, and R. Goic, "A review of solar photovoltaic technologies," Renew. Sustainable Energy Rev. **15**, 1625 (2011).

[41] W. Shockley and H. J. Queisser, "Detailed balance limit of efficiency of p-n junction solar cells," J. Appl. Phys. **32**, 510 (1961).

[42] A. Kojima, K. Teshima, Y. Shirai, and T . Miyasaka, "Organometal halide perovskites as visible-light sensitizers for photovoltaic cells," J . Am. Chem. Soc. **131**, 6050 (2009).

[43] H.-S. Kim, C.-R. Lee, J.-H. Im, K.-B. Lee, T. Moehl, A. Marchioro, S.-J. Moon, R. Humphry-Baker, J.-H. Yum, J. E. Moser, M. Grätzel, and N.-G. Park, "Lead iodide perovskite sensitized all-solid-state submicron thin film mesoscopic solar Cell with efficiency exceeding 9%," Sci. Rep. **2**, 591 (2012).

[44] J. S. Manser, J. A. Christians, and P. V. Kamat, "Intriguing optoelectronic properties of metal halide perovskites," Chem. Rev. **116**, 12956 (2016).

[45] M. Grätzel, "The rise of highly efficient and stable perovskite solar cells," Acc. Chem. Res. **50**, 487 (2017).

[46] S. Günes, H. Neugebauer, and N. S. Sariciftci, "Conjugated polymer-based organic solar cells," Chem. Rev. **107**, 1324 (2007).

[47] I. D. Parker, "Carrier tunneling and device characteristics in polymer light-emitting diodes," J. Appl. Phys. **75**, 1656 (1994).

[48] J. M. Nunzi, "Organic photovoltaic materials and devices," C. R. Physique **3**, 523 (2002).

[49] B. Valle, "Design of Multilayer Optical Media: Organic Photovoltaics and Optical Data Storage," Thesis pp. 7 (2013).

[50] J. Rostalski and D. Meissner, "Monochromatic versus solar efficiencies of organic solar cells," Sol. Energy Mater. Sol. Cells **61**, 87 (2000).

[51] J.-H. Im, J. Chung, S.-J. Kim, and N.-G. Park, "Synthesis, structure, and photovoltaic property of a nanocrystalline 2H perovskite-type novel sensitizer ($CH_3CH_2NH_3$)PbI_3," Nanoscale Res. Lett. **7**, 353 (2012).

[52] G. E. Eperon, S. D. Stranks, C. Menelaou, M. B. Johnston, L. M. Herz, and H. J. Snaith, "Formamidinium lead trihalide: a broadly tunable perovskite for efficient planar heterojunction solar cells," Energy Environ. Sci. **7**, 982 (2014).

[53] M. I. Ahmed, A. Habib, and S. S. Javaid, "Perovskite solar cells: potentials, challenges, and opportunities," Int. J. Photoenergy **2015**, 1 (2015).

[54] F. Hao, C. C. Stoumpos, R. P. H. Chang, and M. G. Kanatzidis, "Anomalous band gap behavior in mixed Sn and Pb perovskites enables broadening of absorption spectrum in solar cells," J. Am. Chem. Soc. **136**, 8094 (2014).

[55] S. D. Wolf, J. Holovsky, S.-J. Moon, P. Löper, B. Niesen, M. Ledinsky, F.-J. Haug, J.-H. Yum, and C. Ballif, "Organometallic halide perovskites: sharp optical absorption edge and its relation to photovoltaic performance," J. Phys. Chem. Lett. **5**, 1035 (2014).

[56] A. Miyata, A. Mitioglu, P. Plochocka, O. Portugall, J. T. W. Wang, S. D. Stranks, H. J. Snaith, and R. J. Nicholas, "Direct measurement of the exciton binding energy and effective masses for charge carriers in organic-inorganic tri-halide perovskites," Nat. Phys. **11**, 582 (2015).

[57] K. Galkowski, A. Mitioglu, A. Miyata, P. Plochocka, O. Portugall, G. E. Eperon, J. T.-W. Wang, T. Stergiopoulos, S. D. Stranks, H. Snaith, and R. J. Nicholas, "Determination of the exciton binding energy and effective masses for methylammonium and formamidinium lead tri-halide perovskite semiconductors," Energy Environ. Sci. **9**, 962 (2016).

[58] C. Wehrenfennig, G. E. Eperon, M. B. Johnston, H. J. Snaith, and L. M. Herz, "High charge carrier mobilities and lifetimes in organolead trihalide perovskites," Adv. Mater. **26**, 1584 (2014).

[59] M. B. Johnston and L. M. Herz, "Hybrid perovskites for photovoltaics: charge-carrier recombination, diffusion, and radiative efficiencies," Acc. Chem. Res. **49**, 146 (2016).

[60] S. D. Stranks and H. J. Snaith, "Metal-halide perovskites for photovoltaic and light-emitting devices," Nat. Nanotechnol. **10**, 391 (2015).

[61] V. Gonzalez-Pedro, E. J. Juarez-Perez, W.-S. Arsyad, E. M. Barea, F. Fabregat-Santiago, I. Mora-Sero, and J. Bisquert, "General working principles of $CH_3NH_3PbX_3$ perovskite solar cells," Nano Lett. **14**, 888 (2014).

[62] H. J. Snaith, A. Abate, J. M. Ball, G. E. Eperon, T. Leijtens, N. K. Noel, S. D. Stranks, J. T.-W. Wang, K. Wojciechowski, and W. Zhang, "Anomalous hysteresis in perovskite solar cells," J. Phys. Chem. Lett. **5**, 1511 (2014).

[63] E. L. Unger, E. T. Hoke, C. D. Bailie, W. H. Nguyen, A. R. Bowring, T. Heumüller, M. G. Christoforo, and M. D. McGehee, "Hysteresis and transient behavior in current-voltage measurements of hybrid-perovskite absorber solar cells," Energy Environ. Sci. **7**, 3690 (2014).

[64] Y. Zhang, M. Liu, G. E. Eperon, T. C. Leijtens, D. McMeekin, M. Saliba, W. Zhang, M. de Bastiani, A. Petrozza, L. M. Herz, M. B. Johnston, H. Lin, and H. J. Snaith, "Charge selective contacts, mobile ions and anomalous hysteresis in organic-inorganic perovskite solar cells," Mater. Horiz. **2**, 315 (2015).

[65] W. Tress, N. Marinova, T. Moehl, S. M. Zakeeruddin, M. K. Nazeeruddin and M. Grätzel, "Understanding the rate-dependent J-V hysteresis, slow time component, and aging in $CH_3NH_3PbI_3$ perovskite solar cells: the role of a compensated electric field," Energy Environ. Sci. **8**, 995 (2015).

[66] I. C. Smith, E. T. Hoke, D. Solis-Ibarra, M. D. McGehee, and H. I. Karunadasa, "A layered hybrid perovskite solar-cell absorber with enhanced moisture stability," Angew. Chem. Int. Ed. **53**, 11232 (2014).

[67] D. H. Cao, C. C. Stoumpos, O. K. Farha, J. T. Hupp, and M. G. Kanatzidis, "2D homologous perovskites as light-absorbing materials for solar cell applications," J. Am. Chem. Soc. **137**, 7843 (2015).

[68] H. Tsai, W. Nie, Jean-Christophe Blancon, C. C. Stoumpos, R. Asadpour, B. Harutyunyan, A. J. Neukirch, R. Verduzco, J. J. Crochet, S. Tretiak, L. Pedesseau, J. Even, M. A. Alam, G. Gupta, J. Lou, P. M. Ajayan, M. J. Bedzyk, M. G. Kanatzidis, and A. D. Mohite, "High-efficiency two-dimensional Ruddlesden-Popper perovskite solar cells," Nature **536**, 312 (2016).

[69] B. Valle, S. Loser, J. W. Hennek, V. DeGeorge, C. Klosterman, J. H. Andrews, and K. D. Singer, "Spectral aspects of cavity tuned absorption in organic photovoltaic films," Opt. Express **20**, A954 (2012).

[70] S. Loser, B. Valle, K. A. Luck, C. K. Song, G. Ogien, M. C. Hersam, K. D. Singer, and T. J. Marks, "High-efficiency inverted polymer photovoltaics via spectrally tuned absorption enhancement," Adv. Energy Mater. **4**, 1301938 (2014).

2 Ultrastrong Coupling in Single and Double Low-Q Organic Cavities

2.1 Introduction

Light-matter interactions in optical cavities are being intensively studied, well beyond the laser concept and now encompassing both fundamental investigations and application in light emission, nonlinear optics, and quantum information.[71–73] The effect of the optical cavity on the emission of light can be divided into different regimes. In the weak coupling regime, the spatial and temporal distribution of the emitted light can be altered. In the strong coupling regime, energy exchange between the emitter and cavity mode becomes faster than any dissipation or decoherence in what is known as vacuum Rabi oscillations. This mixing between optical and electronic (excitonic) states within the cavity leads to the formation of quasi-particles termed cavity polaritons, which are characterized by the anticrossing dispersion with a vacuum Rabi splitting ($\hbar\Omega_R$).

Originally, strong coupling was studied with atoms in a resonant cavity,[74] and, later, strong exciton-photon coupling was first demonstrated with GaAs quantum wells in optical inorganic microcavities.[75] Quantum well excitons in inorganic semiconductors are of the Wannier-Mott-type. These extended excited states are weakly

bound (∼meV) and can have large Bohr radii (>10 nm). The excitonic state has a low saturation density and can generally be ionized at room temperature. These features often limit the observation and study of the strongly coupled state to low temperatures and small excitation densities.[76] Similarly, the low exciton oscillator strength results in small Rabi splittings. Recent developments have led to demonstrations of room-temperature strong exciton-photon coupling and polariton lasing in group III nitrides and ZnO, which triggered tremendous attention and interest in the manipulation of this system for strongly coupled devices.[77,78]

In contrast to inorganic materials, excitons in organic materials exhibit a number of appealing physical properties relevant to strong coupling. Particularly, the excitons in organic materials are tightly bound (∼1 eV) Frenkel-type states that can have large oscillator strengths along with their strong exciton binding energies. In addition, a large density of molecules can easily be deposited in an optical structure. Therefore, the high effective transition dipole moments of organic materials can compensate for low Q-factor cavities. Strong exciton-photon coupling was first demonstrated by using a spun cast film of the organic semiconductor (4TBPPZn) in polystyrene located in a planar microcavity at room temperature, yielding a vacuum Rabi splitting of $\hbar\Omega_R = 110$ meV,[79] which is followed by numerous experimental demonstrations of strong coupling using organic materials, such as cyanine dye J-aggregates,[80] polycrystalline films,[81] single-crystal anthracene,[82] polymers,[83] and two-dimensional layered transition metal dichalcogenides (TMD).[84,85] Due to the remarkable properties of organic cavity polaritons, some interesting room-temperature physical observations have been reported, for example, polariton condensate and lasing,[83,86] polariton-mediated

energy transfer,[87,88] polariton-induced work-function modification,[89] and superfluidity.[90]

In the limit where the exciton-photon coupling is increased to a significant fraction of the uncoupled exciton energy ($\hbar\Omega_R \sim E_{ex}$), the light-matter interacting system enters the so-called ultrastrong coupling regime (USC), where the presence of non-negligible antiresonant light-matter interaction terms leads to modifications of both excited and ground state properties. Demonstrations of USC in organic microcavities have been reported, which have sparked interest in the study of its effect on material properties and practical applications.[91–93]

Importantly, multiple coupled microcavities introduce additional degrees of freedom, both for materials and the cavity interactions, and have attracted increasing attention. Quantum well based multiple coupled microcavites (MCs) have been well studied for theory and optical devices.[94–99] Cavity polariton-induced splitting of excitonic states and optical reflection asymmetry were reported by Armitage *et al.* in quantum well based coupled inorganic MCs.[95,96] Some researchers analyzed the polariton-polariton interaction potentials using pump-probe degenerate scattering.[98] With increasing degrees of freedom, these quantum well based multiple coupled microcavity systems have promising applications, such as angle-resonant stimulated polariton amplifiers and optical parametric oscillators.[99] Recently, vertical coupled double organic microcavities have been demonstrated at room temperature, which could offer new opportunities for the development of organic active-media based devices.[100]

To the best of our knowledge, coupling between multiple cavities in the ultrastrong limit has not been observed in any material. Therefore, we focus on single and double organic microcavities, which are composed of neat glassy organic dye films

between metallic (silver) mirrors. Via room-temperature optical characterization of these cavities, we experimentally find that:

- Ultrastrong exciton-photon coupling is demonstrated from low-Q single organic microcavity at room temperature;
- Four polariton branches exhibit the degeneracy broken of vacuum Rabi splittings in the symmetric double coupled microcavity, which results from the coupling of double cavity comprised two single exciton-photon ultrastrongly coupled microcavities beyond the rotating wave approximation;
- Polariton-induced optical asymmetry is observed from the asymmetric double coupled cavity in the ultrastrong coupling regime.

In addition, the transfer matrix theory with complex index of refraction dispersion data, obtained by detailed modeling of spectroscopic ellipsometry data for each material, is employed for the organic cavities, yielding excellent quantitative agreements between calculation and experimental results. To explain the degeneracy broken of vacuum Rabi splittings, a modified oscillator coupled model is introduced, and the calculated vacuum Rabi splittings are consistent with the measured values.

2.2 Experimental

2.2.1 Cavity Structures and Fabrication

We have studied low-Q single (Fig. 2.1a) and double (Fig. 2.1b and c) cavity using metal mirrors enclosing a neat organic dye glass, DCDHF-6-V, and the inset in Fig. 2.3 shows the chemical structure of this molecule.[101] Two types of double coupled cavities are studied: (I) symmetric cavities where both contain the exciton dye glass, shown

in Fig. 2.1(b), and (II) asymmetric cavities where one is filled with DCDHF-6-V and one with polyvinyl alcohol (PVA), a nonabsorbing polymer, as shown in Fig. 2.1(c).

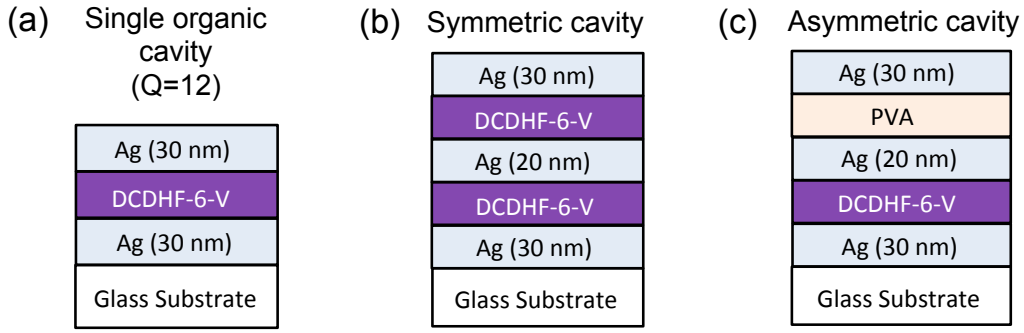

Figure 2.1. Structures of organic cavities: (a) single cavity; (b) symmetric double cavity; (c) asymmetric double cavity. The transparent PVA film within asymmetric cavity works as a spacer layer.

Organic cavities were fabricated on glass substrates (1 mm), which were cleaned by successive 15 min. sonication at 50 °C in a weak detergent water solution, DI water, acetone, methanol, and isopropanol. First, a thin (30 nm) silver film was thermally evaporated onto the glass substrate in vacuum at 10^{-7} Torr. Next, DCDHF-6-V was spun cast on top of the metal film, and the thickness of the organic film was varied from 90 to 170 nm by adjusting the spin speed. The single cavity fabrication was completed by evaporating a second thin (30 nm) silver film on top of the organic layer. This process provided single cavities with low Q-factors of around 12. For the double coupled cavities, a thinner (20 nm) silver layer was made in the center of cavity structures.

2.2.2 Spectroscopic Ellipsometry Measurements

Spectroscopic ellipsometry was used to obtain the complex refractive index of each material in the organic cavities, and the measurements were carried out with a Horiba Jobin Yvon UVISEL iHR320 ellipsometer for photon energies between 1 eV and 5

eV with 10 meV increment. In this measurement, linearly polarized light with equal intensities of p and s polarization is incident on the measured material at some incidence angle between 55 and 80^o. The specular reflection is collected and the ratio of intensity and phase difference of s to p polarizations is collected. Then the experimental data is fit using a user-defined model composed of the thickness and dispersion of the material and substrate being measured. The complex optical dispersion of the material under investigation can then be used as fitting parameters and optimized to produce the best fit. In the following section, I will show an example of experimental data and modeling functions for DCDHF-6-V, which is more complicated than the modeling for both silver and PVA films.

2.2.3 Absorption and Photoluminescence Measurements

The absorption spectra measurements of neat DCDHF-6-V film were carried out using a Cary 300 UV-Vis spectrophotometer between 300 and 900 nm with 1 nm increment, and the photoluminescence emission spectra were measured by a Horiba Fluorolog-3 spectrofluorometer.

2.2.4 Transmission Measurements

The transmission measurements of single organic cavities with different thickness were carried out using a Cary 300 UV-Vis spectrophotometer between 300 and 900 nm with 1 nm increment.

2.2.5 Angularly Resolved Reflection Measurements

The linearly optical angle-resolved reflectivity spectra of the organic microcavities were acquired at room temperature using a J. A. Woollam Co. Inc V-VASE instrument with an angular increment of 5^o and wavelength from 300 to 900 nm with an increment of 2 nm.

2.3 Results and Discussion

2.3.1 Optical Characterization of DCDHF-6-V film

- **Complex refractive index of DCDHF-6-V**

The dispersion function of complex refractive index (optical constants) used to fit experimental ellipsometric data of DCDHF-6-V is the Forouhi-Bloomer model,[102,103] satisfying Kramers-Kronig relation, which can be expressed as:

$$n(\omega) = n_\infty + \sum_{j=1}^{N} \frac{B\,(\omega - \omega_j) + C}{(\omega - \omega_j) + \Gamma_j^2} \tag{2.1a}$$

$$k(\omega) = \begin{cases} \sum_{j=1}^{N} \dfrac{f_j\,(\omega - \omega_g)^2}{(\omega - \omega_j) + \Gamma_j^2} & \omega > \omega_g \\ 0 & \omega \leq \omega_g \end{cases} \tag{2.1b}$$

where

$$B = \frac{f_j}{\Gamma_j}\left(\Gamma_j^2 - (\omega_j - \omega_g)^2\right) \tag{2.2a}$$

$$C = 2 f_j \Gamma_j\,(\omega_j - \omega_g) \tag{2.2b}$$

with the following fitting parameters:

- n_∞ the long wavelength (low energy) refractive index
- ω_j the frequency of maximum absorption

- f_j the oscillator strength
- ω_g the band gap frequency
- Γ_j the width of the oscillator

The complex refractive index (optical constants) of the DCDHF-6-V film is shown in Fig. 2.2.

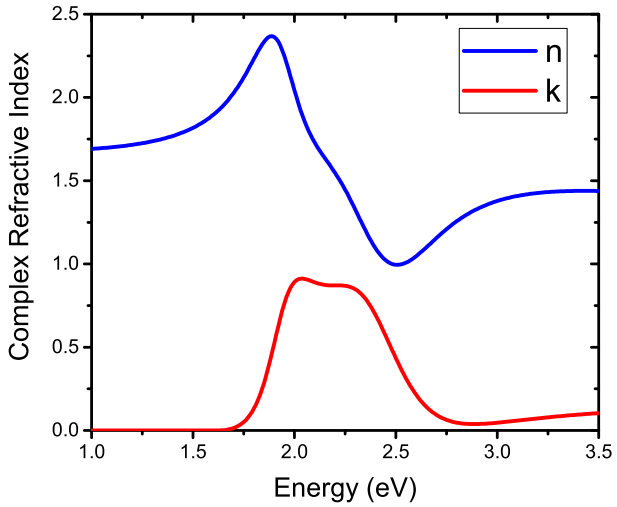

Figure 2.2. The complex refractive index of the DCDHF-6-V film obtained by ellipsometry modeling.

- **Absorption and emission spectra of DCDHF-6-V**

Fig. 2.3 shows the room-temperature absorption and photoluminescence emission spectra from a 90-nm-thick neat film of DCDHF-6-V spun cast onto a glass substrate. The Stokes shift, which is the difference between positions of the band maxima of the absorption and emission spectra of the same material, can be observed, and the FWHM for the transition at 2.16 eV is 0.58 eV, and the strong inhomogeneous broadening of the excitonic resonance results from the disorder inherent in the organic glass (DCDHF-6-V). In addition, it is worth mentioning that the imaginary part

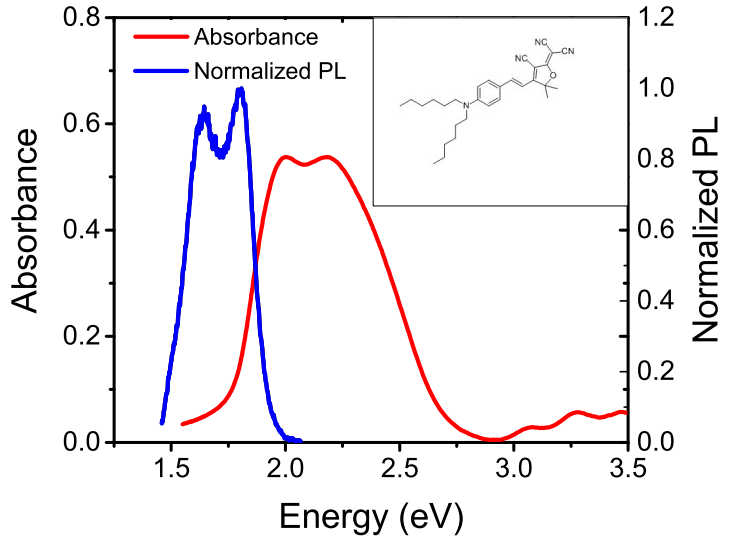

Figure 2.3. The absorbance (red curve) and photoluminescence emission (blue curve) spectra of a 90-nm-thick neat film of DCDHF-6-V. The inset shows the chemical structure of DCDHF-6-V.

(k) of refractive index obtained by ellipsometry modeling behaves the same trend as the measured absorption spectra of DCDHF-6-V, which also indicates that the ellipsometry fitting results of DCDHF-6-V are satisfactory.

2.3.2 Optical Characterization of Single Organic Microcavities

The cavity mode can be tuned to be resonant with the exciton state by varying either the cavity thickness or the angle of incidence, as the wave vector $\vec{k}$ is varied. Thus, to investigate the momentum-energy dispersion relation for the light-matter interacting organic microcavities, we can vary either the cavity thickness or the angle of incidence.

Tuning the cavity mode by varying the cavity thickness

Fig. 2.4(a) show the variation in room-temperature normal-incidence transmittance spectra as the photon mode is tuned by varying the cavity thickness. For each cavity, two transmittance peaks, corresponding to the cavity polariton states, are observed,

and the shift of energetic positions of the cavity polariton states can be seen clearly as the cavity thickness is varied. To represent the experimentally measured dispersion directly, energetic positions of cavity polariton states are plotted as a function of the cavity thickness, shown in Fig. 2.4(b). Two cavity polariton branches, upper polaritons (UP) for higher energy states and lower polaritons (LP) for lower energy states, anticross a point of cavity thickness where dispersions of the uncoupled cavity mode (dashed black curve) and exciton state (solid blue line) cross. At this point, the vacuum Rabi splitting energy ($\hbar\Omega_R$) as the minima of the energy difference between UP and LP, is obtained, yielding a $\hbar\Omega_R$ of 1.12 eV. Thus, the ratio value of the vacuum Rabi splitting energy to the uncoupled exciton energy is $\hbar\Omega_R/E_{ex} = 1.12/2.16 = 0.52$, which is larger than 0.2,[104] indicating the ultrastrong exciton-photon coupling is demonstrated from the low-Q organic microcavities. The dispersion relations of the cavity polariton calculated using the transfer matrix formalism are shown by the solid red curves, which precisely agree with the measurement results. The horizontal blue line is the exciton transition energy of DCDHF-6-V, and this energy is thickness independent, which is expected to give the resonance energy for the coupled exciton-photon system.

Tuning the cavity mode by varying the angle of incidence

Fig. 2.5(a) and (b) show the variation in room-temperature reflectivity spectra as the photon mode is angle tuned through the exciton mode energy with TM and TE polarized light, respectively. At each angle, two reflectivity dips, corresponding to the cavity polariton states, are observed, and the shift of energetic positions of the cavity polariton states can be seen clearly as the angle of incidence is varied. To represent the experimentally measured dispersion more directly, contour plots of the

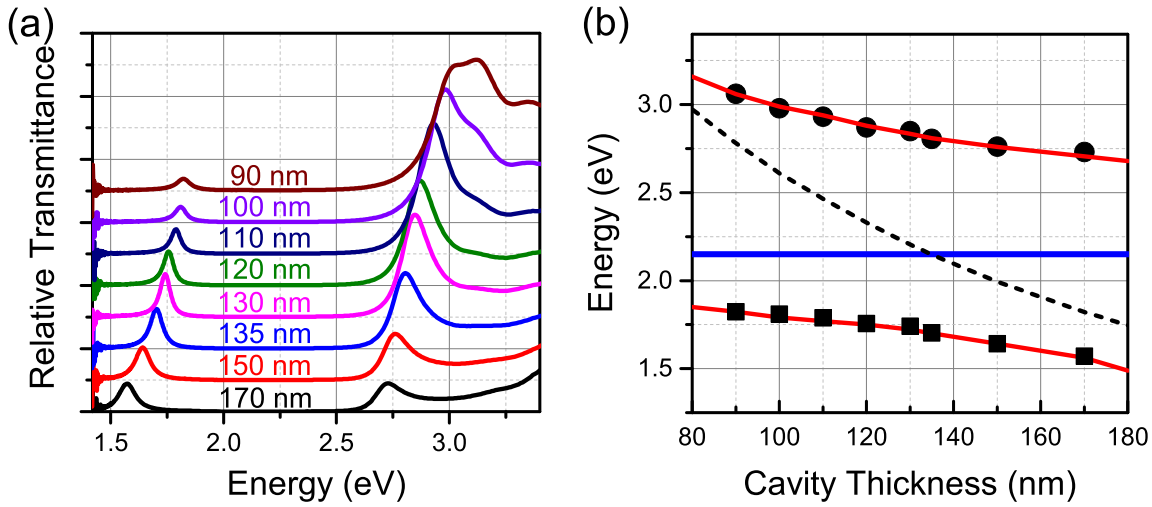

Figure 2.4. (a) Normal-incidence transmittance spectra of organic microcavities. The spectra for different cavity thickness (indicated in the figure) have been displaced vertically for clarity. (b) Anticrossing dispersions as a function of the cavity thickness. The circles and squares are experimental data, and the red curves are obtained by the transfer matrix calculation. The dashed black curve is the dispersion of bare cavity mode, and the blue line shows the uncoupled exciton transition energy of DCDHF-6-V.

angle-resolved reflectivity (**R**) are shown in Fig. 2.6(a) for TM and Fig. 2.6(b) for TE polarization. The dispersion shown in Fig. 2.6(a) and Fig. 2.6(b) exhibits widely separated anticrossed states characteristic of a strongly coupled exciton-polariton. Again, upper polariton (UP) and lower polariton (LP) branches are observed near the point where the dispersions of the uncoupled cavity mode (dashed white curve) and exciton state (solid blue line) cross. The dispersion relations of the cavity polariton calculated using the transfer matrix reflectivity model are shown by the dashed black curves, which precisely agree with the measurement results. Comparing these two contour plots, the polariton dispersion of the TM modes is flatter than that of the TE modes consistent with polarization dependence of the bare cavity photon dispersion shown as the dashed white curves in Fig. 2.6(a) and Fig. 2.6(b). The resonance

between cavity photon and exciton occurs at around 25^o and 15^o for TM and TE polarization, respectively.

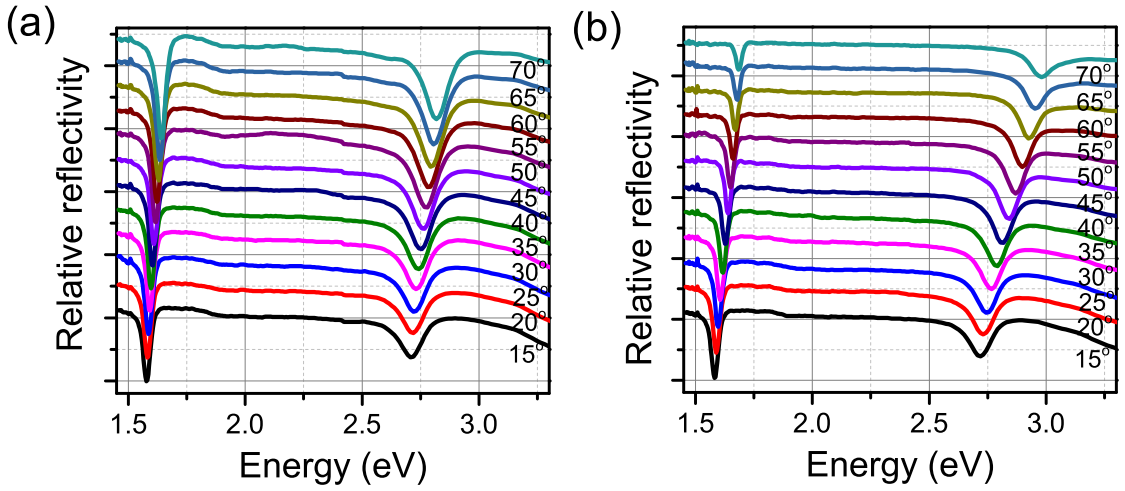

Figure 2.5. Angularly resolved reflectivity spectra for an organic microcavity containing a 140-nm-thick DCDHF-6-V film for TM (a) and TE (b) polarization. The spectra for different measurement angles (indicated in the figure) have been displaced vertically for clarity.

Significantly, using the angle as the parameter to determine the vacuum Rabi splitting energy always results in an important overestimation of the strength of the coupling.[105] To obtain $\hbar\Omega_R$ correctly from the angularly resolved reflectivity measurement results, the energy positions of the reflectivity dips are re-plotted as a function of the wave vector, which are shown in Fig. 2.7(a) for TM and Fig. 2.7(b) for TE polarization, respectively. The in-plane wave vector $\mathbf{k}_{\|}$ is related to the incident angle θ and wavelength λ of the incident light through the relation:[106]

$$k_{\|} = k \sin\theta = (2\pi/\lambda) \sin\theta \tag{2.3}$$

Thus, the measured anticrossing dispersions as a function of the wave vector lead to the same $\hbar\Omega_R$ of 1.12 eV, which is the minimal energy separation between the

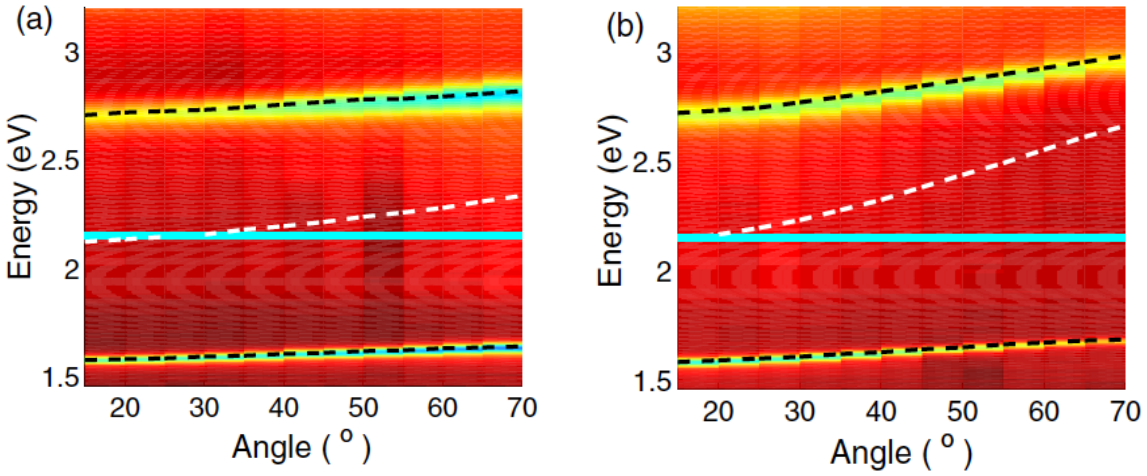

Figure 2.6. Angle-resolved reflectivity maps of the 140-nm-thick microcavity. The spectra are shown for TM (a) and TE (b) polarization. The dashed black curves, which are obtained by transfer matrix calculation, trace the positions of the reflectivity minima that correspond to the UP and LP branches. The dashed white curve is the dispersion of bare cavity mode, and the blue line shows the DCDHF-6-V exciton transition energy.

polariton branches, for both TM and TE polarization, and this is equal to the value of $\hbar\Omega_R$ obtained from the cavity-thickness dependent anticrossing dispersion.

Next, we can examine the calculated vacuum Rabi splitting energy with a simple classical model. The coupling parameter between a dielectric material and an optical cavity is given as follows:

$$g_0 = \left(\frac{N\mu_{12}^2 \omega_{ex}}{2V_0 \epsilon \hbar} \right)^{1/2} \tag{2.4}$$

where ϵ is the dielectric constant of organic material, N/V_0 is the molecular number density, $E_0 = \hbar\omega_{ex}$ is the uncoupled exciton transition energy, and $\mu_{12} \equiv \langle \Psi_1 | e\vec{r} | \Psi_2 \rangle$ is the electric dipole matrix element of the transition. Generally, in the classical oscillator model, the vacuum Rabi splitting energy $\hbar\Omega_R$ in an OMC can be expressed

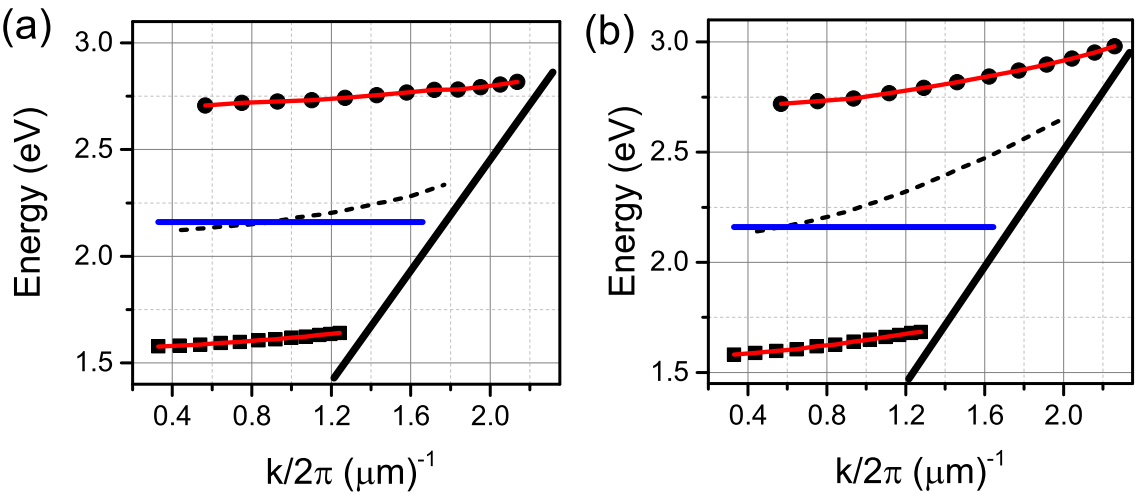

Figure 2.7. Anticrossing dispersions as a function of the wave vector for TM (a) and TE (b) polarization. The circles and squares are measurement data, and the red curves are obtained by transfer matrix calculation. The dashed black curve is the dispersion of bare cavity mode, and the blue line shows the DCDHF-6-V exciton energy. The diagonal black line on the right of the plots signifies the maximum scan angle.

as

$$\hbar\Omega_R = 2\left[(\hbar g_0)^2 - \frac{1}{4}(\gamma_{ex} - \gamma_{cav})^2\right]^{1/2} \tag{2.5}$$

where γ_{ex} and γ_{cav} are half widths (HWFM) of the uncoupled exciton and cavity mode, respectively. The parameters shown in Eq. 2.4 and Eq. 2.5 for the (DCDHF-6-V)-filled OMC are given in Table 2.1. The calculated vacuum Rabi splitting using Eq. 2.4 and Eq. 2.5 along with the experimentally determined oscillator strength and spectral widths is obtained as 1.118 eV, which is in excellent agreement with the experimental value of 1.120 eV, even though Eq. 2.5 applies to homogeneously broadened spectra. These results are consistent with the sharp falloff of the inhomogeneously broadened spectra where the coherence of the inhomogeneously broadened dipoles is maintained.[107] This is in keeping with the narrow polariton linewidths observed and

with the observations of Gambino *et al.*[108] There are three main contributions to the large vacuum Rabi splitting of the (DCDHF-6-V)-filled OMC: (1) the large number density of the material as a neat organic glass; (2) the large electric dipole matrix element of the transition due to the broad absorption spectrum and high exciton oscillator strength; and (3) the similar linewidths between the uncoupled exciton and cavity mode. The first two factors give rise to a large coupling parameter $\hbar g_0$ around 0.56 eV, thus a large vacuum Rabi splitting, because $\hbar\Omega_R$ depends on the oscillator strength determined from the energy-integrated absorption rather than on just the magnitude of the absorption peak.[108,109]

Table 2.1. Parameter values in Eq. 2.4 and Eq. 2.5 for an OMC filled with a 140 nm DCDHF-6-V film.

N/V_0 (cm^{-3})	μ_{12} (D)	$\hbar\omega_{ex}$ (eV)	γ_{ex} (eV)	γ_{cav} (eV)	$\hbar g_0$ (eV)	$(\hbar\Omega_R)_{calc}$ (eV)	$(\hbar\Omega_R)_{expt.}$ (eV)
1.8×10^{21}	7.3	2.16	0.29	0.23	0.56	1.118	1.120

2.3.3 Optical Characterization of Symmetric Double OMCs

For the symmetric double OMCs with the structure shown in Fig. 2.1(b), a series of TM polarized reflectivity spectra taken at room temperature are shown in Fig. 2.8(a). For each angle, four reflectivity dips corresponding to the cavity polariton states, are observed, and the energetic positions of the dips shift as the angle of incidence are varied. Extracting the energetic positions of those reflectivity minima, four cavity polariton blanches, indicated as UP, MP1, MP2, and LP branch, can be seen in Fig. 2.8(b). According to the measurement results, anticrossing between UP and MP2 leads to a vacuum Rabi splitting $\hbar\Omega_{R1}$ of 1.11 eV, while anticrossing between MP1 and LP yields a vacuum Rabi splitting $\hbar\Omega_{R2}$ of 1.08 eV. The anticrossing occurs at

different angles (different wave vector **k**), which is consistent with the observation by Armitage *et al.* for the strongly coupled inorganic MCs, and this is due to the splitting between symmetric and antisymmetric cavity modes.[95] However, the inequality of these two splittings is inconsistent with the prediction of the classical four-oscillator coupled model proposed by Armitage *et al.* for the strong coupling regime. For the coupled OMCs in the ultrastrong coupling regime, a modified four-oscillator coupled model is now examined that takes into account the antiresonant Hamiltonian terms for the interacting system beyond the rotating wave approximation (RWA).

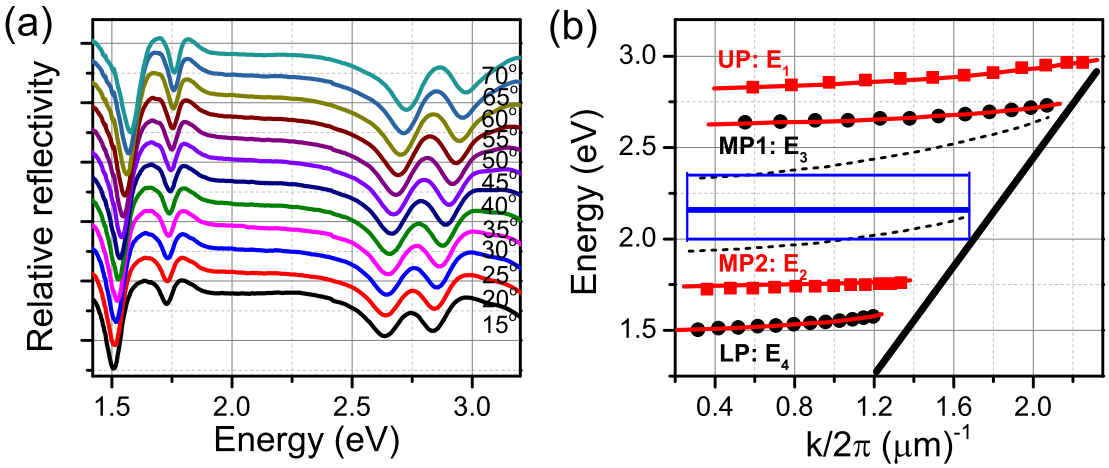

Figure 2.8. (a) Angularly resolved reflectivity spectra for a symmetric double OMC containing two 140-nm-thick DCDHF-6-V layers for TM polarization. The spectra for different measurement angles (indicated in the figure) have been displaced vertically for clarity. (b) Energetic positions of reflectivity dips plotted as a function of the wave vector. Experimental data are shown as circles and squares, and the solid red curves are obtained by transfer matrix calculation. The dashed black curves are the dispersion of bare-cavity symmetric and antisymmetric modes. The blue rectangular box shows inhomogeneous broadening of excitonic resonance of DCDHF-6-V. The diagonal black line on the right of the plot signifies the maximum scan angle.

First, the optical fields in the coupled cavities yield symmetric and antisymmetric cavity modes, and the coupled cavity energies can be obtained via[95]

$$\begin{bmatrix} E_c & V_0 \\ V_0 & E_c \end{bmatrix} \begin{bmatrix} \alpha \\ \beta \end{bmatrix} = E \begin{bmatrix} \alpha \\ \beta \end{bmatrix} \tag{2.6}$$

where E_c is the energy of the uncoupled cavity modes and V_0 is the optical coupling parameter between the cavities. The energies of the symmetric and antisymmetric coupled cavity modes are given by $E_S = E_c + V_0$, $E_{AS} = E_c - V_0$.

Second, the exciton states in the two separate cavities also form symmetric and antisymmetric combinations (ψ_S, ψ_{AS}) given as $\psi_S = (\phi_1 + \phi_2)/2$ and $\psi_{AS} = (\phi_1 - \phi_2)/2$, where ϕ_1 and ϕ_2 are the single exciton wave functions in the two cavities.[95,110]

Third, the symmetric coupled cavity mode couples to the symmetric exciton state ψ_S, and the antisymmetric coupled cavity mode couples to the antisymmetric exciton state ψ_{AS} via the equation which describes the eigenvalues of the Hopfield Hamiltonian of the interacting system:[108,111,112]

$$(E_{cav}^2 - E^2)(\hat{E}_{ex}^2 - E^2) = \beta^2 E_{ex}^2 E_{cav}^2 \tag{2.7}$$

where E_{ex} is the uncoupled exciton energy, $\beta = \hbar\Omega_R/E_{ex}$, and $\hat{E}_{ex}^2 = E_{ex}^2 + \beta^2 E_{ex}^2$. E_{cav} describes the energy dispersion of the cavity mode; for the coupled cavities, E_{cav} can be described as $E_S = E_c + V_0$, $E_{AS} = E_c - V_0$. Thus, for the coupled double microcavities, taking into account the antiresonant Hamiltonian terms, the polariton energies can be described via

$$(E_{S/AS}^2 - E^2)(E_{ex}^2 + \beta^2 E_{ex}^2 - E^2) = \beta^2 E_{ex}^2 E_{S/AS}^2 \tag{2.8}$$

If β is relatively small, corresponding to strong exciton-photon coupling, the above equation can be approximated as

$$(E_{S/AS} - E)(E_{ex} - E) = V_1^2 \tag{2.9}$$

where we define $V_1^2 = \frac{1}{4}\beta^2 E_{ex} E_{S/AS}$, which is the coupling parameter between exciton and cavity modes. The above equations are the result of the classical four-oscillator coupled model, and the solutions for polariton eigenvalues at resonance (namely, $E_c = E_{ex}$) are given as

$$\begin{aligned} E_{1,2} &= \frac{1}{2}(2E_{ex} + V_0 \pm \sqrt{V_0^2 + 4V_1^2}) \\ E_{3,4} &= \frac{1}{2}(2E_{ex} - V_0 \pm \sqrt{V_0^2 + 4V_1^2}) \end{aligned} \tag{2.10}$$

At resonance conditions, $\hbar\Omega_{R1} = \Delta E_{12} = \Delta E_{34} = \hbar\Omega_{R2} = \sqrt{V_0^2 + 4V_1^2}$, and this relation can only hold when the small-β condition is satisfied.

For the ultrastrong coupling regime, β is significant, thus, the polariton eigenvalues at resonance conditions can be derived from Eq. 2.8:

$$\begin{aligned} E_{1,2}^2 &= \pm\frac{1}{2}\sqrt{(E_{ex}^2 + E_{SR}^2 + (\hbar\Omega_{R1})^2)^2 - 4E_{ex}^2 E_{SR}^2} \\ &\quad + \frac{1}{2}\left(E_{ex}^2 + E_{SR}^2 + (\hbar\Omega_{R1})^2\right) \\ E_{3,4}^2 &= \pm\frac{1}{2}\sqrt{(E_{ex}^2 + E_{ASR}^2 + (\hbar\Omega_{R2})^2)^2 - 4E_{ex}^2 E_{ASR}^2} \\ &\quad + \frac{1}{2}\left(E_{ex}^2 + E_{ASR}^2 + (\hbar\Omega_{R2})^2\right) \end{aligned} \tag{2.11}$$

where $E_{SR} = E_{ex} + V_0$, $E_{ASR} = E_{ex} - V_0$ at resonance conditions. According to Eq. 2.11, we can derive that $\hbar\Omega_{R1} = \triangle E_{12} = f\left[(\hbar\Omega_{R1})^2, E_{SR}^2\right]$, $\hbar\Omega_{R2} = \triangle E_{34} = f\left[(\hbar\Omega_{R2})^2, E_{ASR}^2\right]$, which could not guarantee that the equality $\hbar\Omega_{R1} = \hbar\Omega_{R2}$ always holds. From the measurement results, shown in Fig. 2.8(b), anticrossing between UP

and MP2 leads to a measured vacuum Rabi splitting $\hbar\Omega_{R1} = E_1 - E_2 = 2.83 - 1.72 = 1.11$ eV, which is the minima of the energy difference between UP and MP2, and the calculated $\hbar\Omega_{R1}$ from Eq. 2.11 is 1.106 eV. Anticrossing between MP1 and LP leads to a measured vacuum Rabi splitting $\hbar\Omega_{R2} = E_3 - E_4 = 2.64 - 1.56 = 1.08$ eV, and the calculated $\hbar\Omega_{R2}$ from Eq. 2.11 is 1.06 eV. The results are summarized in Table 2.2, and the strong quantitative agreement between the measurement and calculated results confirm that the modified four-oscillator coupled model can describe the dispersion of cavity polariton states and permit a good physical understanding of the on-resonance behavior for the coupled symmetric double microcavities in the ultrastrong coupling regime. The observed broken degeneracy between the UP-MP2 and MP1-LP vacuum Rabi splittings is a signature of coupling between the double exciton-photon ultrastrongly coupled cavities and the higher-order antiresonant terms beyond the the rotating wave approximation.

Table 2.2. Comparison between experimental and calculated vacuum Rabi splitting $\hbar\Omega_R$.

Vacuum Rabi Splitting	Bands	Energies (eV)	$(\hbar\Omega_R)_{calc}$ (eV)	$(\hbar\Omega_R)_{expt.}$ (eV)
$\hbar\Omega_{R1}$	UP-MP_2	$E_1 - E_2$	1.11	1.11 ± 0.01
$\hbar\Omega_{R2}$	MP_1 -LP	$E_3 - E_4$	1.06	1.08 ± 0.01

2.3.4 Optical Characterization of Asymmetric Double OMCs

For the asymmetric double OMCs with the structure shown in Fig. 2.1(c), the angle-resolved reflectivity spectra taken for TM polarization at room temperature are shown in Fig. 2.9(a) and Fig. 2.10(a) when the microcavity is illuminated from its top and bottom, respectively. In Fig. 2.9(a), three reflectivity dips corresponding to three cavity polariton states (UP, MP, and LP), can be seen for each angle of incidence when

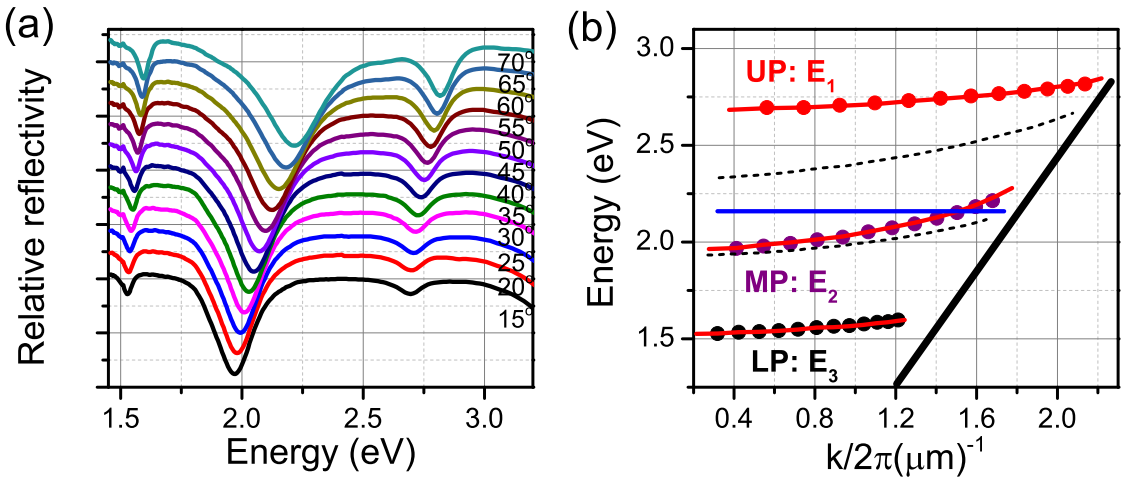

Figure 2.9. (a) Angularly resolved reflectivity spectra for an asymmetric double OMC, which has a structure shown in Fig. 2.1(c), containing a 140-nm-thick DCDHF-6-V film and a 140-nm-thick PVA film for TM polarization. The coupled cavity is illuminated from its top. (b) Energetic positions of reflectivity dips plotted as a function of the wave vector. Experimental data are shown as circles, and the solid red curves are obtained by transfer matrix calculation. The dashed black curves are the dispersion of bare-cavity symmetric and antisymmetric modes. The blue line is the uncoupled exciton transition energy of DCDHF-6-V. The diagonal black line on the right of the plot signifies the maximum scan angle.

the microcavity is illuminated from its top. The energetic positions of cavity polariton states shift as the angle, thus the wave vector, is varied, consistent with anticrossing dispersion, which is shown in Fig. 2.9(b). When the reflectivity measurements are taken by illuminating the cavity from its bottom, only two reflectivity dips, which correspond to UP and LP states, are observed for each angle of incidence, and the central mode (MP) is unobservable.

According to measurement results and the discussions above, the central mode is unobservable when light is incident on the cavity containing DCDHF-6-V film. In contrast, when light is incident on the cavity containing the spacer layer of PVA film, the central mode (MP) is always observable and strong, and more photon-like

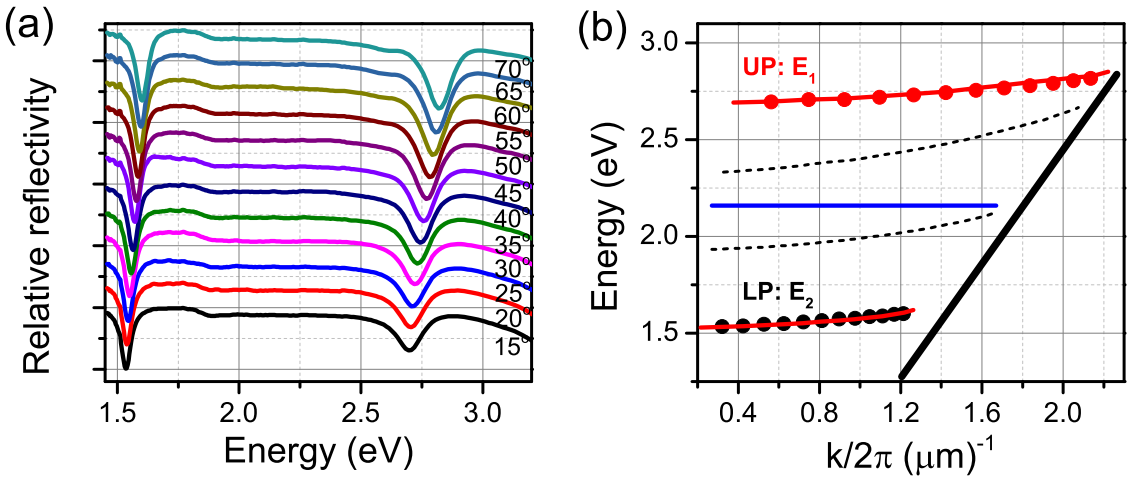

Figure 2.10. (a) Angularly resolved reflectivity spectra for an asymmetric double OMC, which has a structure shown in Fig. 2.1(c), containing a 140-nm-thick DCDHF-6-V film and a 140-nm-thick PVA film for TM polarization. The coupled cavity is illuminated from its bottom. (b) Energetic positions of reflectivity dips plotted as a function of the wave vector. Experimental data are shown as circles, and the solid red curves are obtained by transfer matrix calculation. The dashed black curves are the dispersion of bare-cavity symmetric and antisymmetric modes. The blue line is the uncoupled exciton transition energy of DCDHF-6-V. The diagonal black line on the right of the plot signifies the maximum scan angle.

dispersive than the other two modes (UP and LP). This optical asymmetry in the reflectivity spectra is induced by the cavity polariton, and similar results have been reported for the coupled inorganic microcavities.[96] Armitage *et al.* proposed a three-coupled oscillator model composed of the optical modes from two cavities and the excitonic states, explaining that whether the central mode (MP) is observable (bright) or not (dark) depends on the direction of observation, consistent with the eigenstates of the system. Our results showing very large splittings at room-temperature and low-Q cavities indicate a new regime for observation of this asymmetry. These results may provide applications for fast-response optical switches by converting dark modes to bright ones in asymmetric coupled OMCs.

2.4 Conclusion

In conclusion, we have demonstrated ultrastrong exciton-photon coupling within the low-Q single cavities, which are constructed from low-Q all-metal mirrors filled with the glass forming dye of DCDHF-6-V at room temperature. We also demonstrated the coupling between a pair of ultrastrong coupled single microcavities. Because of the nonlinear coupling describing the ultrastrong limit, the degeneracy between the Rabi splittings associated with symmetric and asymmetric cavity modes is broken by the antiresonant terms beyond the rotating wave approximation. This is in quantitative agreement with a modified four-oscillator coupled model. The large vacuum Rabi splitting, which is an appreciable fraction of the excited state energy of material, and the anticrossing dispersion are the most significant features for the ultrastrong coupling regime. Furthermore, we have observed polariton-induced optical asymmetry in the reflectivity spectra of coupled organic microcavities having much larger splittings than those of coupled inorganic microcavities. These results are very promising for the study of light-matter interaction physics, and could lead to applications of coupled organic multiple microcavities in the ultrastrong light-matter coupling regime for the constituent microcavities at room temperature, for example in organic microcavity light-emitting diodes, where the coupling effect can narrow the linewidth of emission.[113] The coupled multiple cavity is also an interesting system for realizing photon blockades in the ultrastrong coupling regime.[114]

References

[71] G. S. Solomon, M. Pelton, and Y. Yamamoto, "Single-mode spontaneous emission from a single quantum dot in a three-dimensional microcavity," Phys. Rev. Lett. **86**, 3903 (2001).

[72] M. Saba, C. Ciuti, J. Bloch, V. Thierry-Mieg, R. André, Le Si Dang, S. Kundermann, A. Mura, G. Bongiovanni, J. L. Staehli, and B. Deveaud, "High-temperature ultrafast polariton parametric amplification in semiconductor microcavities," Nature **414**, 731 (2001).

[73] J. M. Raimond, M. Brune, and S. Haroche, "Manipulating quantum entanglement with atoms and photons in a cavity," Rev. Mod. Phys. **73**, 565 (2001).

[74] M. G. Raizen, R. J. Thompson, R. J. Brecha, H. J. Kimble, and H. J. Carmichael, "Normal-mode splitting and linewidth averaging for two-state atoms in an optical cavity," Phys. Rev. Lett. **63**, 240 (1989).

[75] C. Weisbuch, M. Nishioka, A. Ishikawa, and Y. Arakawa, "Observation of the coupled exciton-photon mode splitting in a semiconductor quantum microcavity," Phys. Rev. Lett. **69**, 3314 (1992).

[76] R. J. Holmes and S.R. Forrest, "Strong exciton-photon coupling in organic materials," Org. Electron. **8**, 77 (2007).

[77] S. Christopoulos, G. B. H. von Högersthal, A. J. D. Grundy, P. G. Lagoudakis, A. V. Kavokin, and J. J. Baumberg, "Room-temperature polariton lasing in semiconductor microcavities," Phys. Rev. Lett. **98**, 126405 (2007).

[78] T.-C. Lu, Y.-Y. Lai, Y.-P. Lan, S.-W. Huang, J.-R. Chen, Y.-C. Wu, W.-F. Hsieh, and H. Deng, "Room temperature polariton lasing vs. photon lasing in a ZnO-based hybrid microcavity," Opt. Express **20**, 5530 (2012).

[79] D. G. Lidzey, D. D. C. Bradley, M. S. Skolnick, T. Virgili, S. Walker, and D. M. Whittaker, "Strong exciton-photon coupling in an organic semiconductor microcavity," Nature **395**, 53 (1998).

[80] D. G. Lidzey, D. D. C. Bradley, T. Virgili, A. Armitage, M. S. Skolnick, and S. Walker, "Room temperature polariton emission from strongly coupled organic semiconductor microcavities," Phys. Rev. Lett. **82**, 3316 (1999).

[81] R. J. Holmes and S. R. Forrest, "Strong exciton-photon coupling and exciton hybridization in a thermally evaporated polycrystalline film of an organic small molecule," Phys. Rev. Lett. **93**, 186404 (2004).

[82] S. Kéna-Cohen, M. Davanço, and S. R. Forrest, "Strong exciton-photon coupling in an organic single crystal microcavity," Phys. Rev. Lett. **101**, 116401 (2008).

[83] J. D. Plumhof, T. Stöferle, L. Mai, U. Scherf, and R. F. Mahrt, "Room-temperature Bose-Einstein condensation of cavity exciton-polaritons in a polymer," Nat. Mater. **13**, 247 (2014).

[84] X. Liu, T. Galfsky, Z. Sun, F. Xia, E.-C. Lin, Y.-H. Lee, S. Kéna-Cohen, and V. M. Menon, "Strong light-matter coupling in two-dimensional atomic crystals," Nat. Photonics **9**, 30 (2014).

[85] S. Wang, S. Li, T. Chervy, A. Shalabney, S. Azzini, E. Orgiu, J. A. Hutchison, C. Genet, P. Samorì, and T. W. Ebbesen, "Room-temperature Bose-Einstein condensation of cavity exciton-polaritons in a polymer," Nano Lett. **16**, 4368 (2016).

[86] K. S. Daskalakis, S. A. Maier, R. Murray, and S. Kéna-Cohen, "Nonlinear interactions in an organic polariton condensate," Nat. Mater. **13**, 271 (2014).

[87] D. M. Coles, N. Somaschi, P. Michetti, C. Clark, P. G. Lagoudakis, P. G. Savvidis, and D. G. Lidzey, "Polariton-mediated energy transfer between organic dyes in a strongly coupled optical microcavity," Nat. Mater. **13**, 712 (2014).

[88] X. Zhong, T. Chervy, S. Wang, J. George, A. Thomas, J. A. Hutchison, E. Devaux, C. Genet, and T. W. Ebbesen, "Non-radiative energy transfer mediated by hybrid light-matter states," Angew. Chem. Int. Ed. **55**, 6202 (2016).

[89] J. A. Hutchison, A. Liscio, T. Schwartz, A. Canaguier-Durand, C. Genet, V. Palermo, P. Samorì, and T. W. Ebbesen, "Tuning the Work-Function Via Strong Coupling," Adv. Mater. **25**, 2481 (2013).

[90] G. Lerario, A. Fieramosca, F. Barachati, D. Ballarini, K. S. Daskalakis, L. Dominici, M. De Giorgi, S. A. Maier, G. Gigli, S. Kéna-Cohen, and D. Sanvitto, "Room-temperature superfluidity in a polariton condensate," Nat. Phys. **13**, 837 (2017).

[91] J. Galego, F. J. Garcia-Vidal, and J. Feist, "Cavity-induced modifications of molecular structure in the strong-coupling regime," Phys. Rev. X **5**, 041022 (2015).

[92] M. Mazzeo, A. Genco, S. Gambino, D. Ballarini, F. Mangione, O. Di Stefano, S. Patanè, S. Savasta, D. Sanvitto, and G. Gigli, "Ultrastrong light-matter coupling in electrically doped microcavity organic light emitting diodes," Appl. Phys. Lett. **104**, 233303 (2014).

[93] C. R. Gubbin, S. A. Maier, and S. Kéna-Cohen, "Low-voltage polariton electroluminescence from an ultrastrongly coupled organic light-emitting diode," Appl. Phys. Lett. **104**, 233302 (2014).

[94] R. P. Stanley, R. Houdré, U. Oesterle, M. Ilegems, and C. Weisbuch, "Coupled semiconductor microcavities," Appl. Phys. Lett. **65**, 2093 (1994).

[95] A. Armitage, M. S. Skolnick, V. N. Astratov, D. M. Whittaker, G. Panzarini, L. C. Andreani, T. A. Fischer, J. S. Roberts, A. V. Kavokin, M. A. Kaliteevski, and M. R. Vladimirova, "Optically induced splitting of bright excitonic states in coupled quantum microcavities," Phys. Rev. B **57**, 14877 (1998).

[96] A. Armitage, M. S. Skolnick, A. V. Kavokin, D. M. Whittaker, V. N. Astratov, G. A. Gehring, and J. S. Roberts, "Polariton-induced optical asymmetry in semiconductor microcavities," Phys. Rev. B **58**, 15367 (1998).

[97] C. Diederichs and J. Tignon, "Design for a triply resonant vertical-emitting micro-optical parametric oscillator," Appl. Phys. Lett. **87**, 251107 (2005).

[98] T. Lecomte, D. Taj, A. Lemaitre, J. Bloch, C. Delalande, J. Tignon, and P. Roussignol, "Polariton-polariton interaction potentials determination by pump-probe degenerate scattering in a multiple microcavity," Phys. Rev. B **89**, 155308 (2014).

[99] C. Diederichs, J. Tignon, G. Dasbach, C. Ciuti, A. Lematre, J. Bloch, P. Roussignol, and C. Delalande, "Parametric oscillation in vertical triple microcavities," Nature **440**, 904 (2006).

[100] S. Stelitano, G. D. Luca, S. Savasta, L. M. Scolaro, and S. Patané, "Vertical coupled double organic microcavities," Appl. Phys. Lett. **95**, 093303 (2009).

[101] B. Liu, P. Rai, J. Grezmak, R. J. Twieg, and K. D. Singer, "Coupling of exciton-polaritons in low-Q coupled microcavities beyond the rotating wave approximation," Phys. Rev. B **92**, 155301 (2015).

[102] A. Forouhi and I. Bloomer, "Optical dispersion relations for amorphous semiconductors and amorphous dielectrics," Phys. Rev. B **34**, 7018 (1986).

[103] A. Forouhi and I. Bloomer, "Optical properties of crystalline semiconductors and dielectrics," Phys. Rev. B **38**, 1865 (1988).

[104] S. Kéna-Cohen, S. A. Maier, and D. D. C. Bradley, "Ultrastrongly coupled exciton-polaritons in metal-clad organic semiconductor microcavities," Adv. Opt. Mater. **1**, 827 (2013).

[105] C. Symonds, C. Bonnand, J. C. Plenet, A. Bréhier, R. Parashkov, J. S. Lauret, E. Deleporte, and J. Bellessa, "Particularities of surface plasmon-exciton strong coupling with large Rabi splitting," New J. Phys. **10**, 065017 (2008).

[106] P. A. Hobson, W. L. Barnes, D. G. Lidzey, G. A. Gehring, D. M. Whittaker, M. S. Skolnick, and S. Walker, "Strong exciton-photon coupling in a low-Q all-metal mirror microcavity," Appl. Phys. Lett. **81**, 3519 (2002).

[107] I. Diniz, S. Portolan, R. Ferreira, J. M. Gérard, P. Bertet, and A. Auffèves, "Strongly coupling a cavity to inhomogeneous ensembles of emitters: Potential for long-lived solid-state quantum memories," Phys. Rev. A **84**, 063810 (2011).

[108] S. Gambino, M. Mazzeo, A. Genco, O. Stefano, S. Savasta, S. Patanè, D. Ballarini, F. Mangione, G. Lerario, D. Sanvitto, and G. Gigli, "Exploring light-matter interaction phenomena under ultrastrong coupling regime," ACS Photonics **1**, 1042 (2014).

[109] R. Houdré, R. P. Stanley, and M. Ilegems, "Vacuum-field Rabi splitting in the presence of inhomogeneous broadening: Resolution of a homogeneous linewidth in an inhomogeneously broadened system," Phys. Rev. A **53**, 2711 (1996).

[110] G. Panzarini, L. C. Andreani, A. Armitage, D. Baxter, M. S. Skolnick, V. N. Astratov, J. S. Roberts, A. V. Kavokin, M. R. Vladimirova, and M. A. Kaliteevski, "Exciton-light coupling in single and coupled semiconductor microcavities: Polariton dispersion and polarization splitting," Phys. Rev. B **59**, 5082 (1999).

[111] Y. Todorov, A. M. Andrews, R. Colombelli, S. De Liberato, C. Ciuti, P. Klang, G. Strasser, and C. Sirtori, "Ultrastrong light-matter coupling regime with polariton dots," Phys. Rev. Lett. **105**, 196402 (2010).

[112] J. J. Hopfield, "Theory of the contribution of excitons to the complex dielectric constant of crystals," Phys. Rev. **112**, 1555 (1958).

[113] S. Wang, T. Chervy, J. George, J. A. Hutchison, C. Genet, and T. W. Ebbesen, "Quantum yield of polariton emission from hybrid light-matter states," J. Phys. Chem. Lett. **5**, 1433 (2014).

[114] A. Ridolfo, M. Leib, S. Savasta, and M. J. Hartmann, "Photon blockade in the ultrastrong coupling regime," Phys. Rev. Lett. **109**, 193602 (2012).

3 Cavity-Polariton Enhanced Third-Harmonic Generation in Organic Cavities

3.1 Introduction

Strong exciton-photon coupling within microcavities results in new eigenstates of microcavity polariton systems, which are characterized by anticrossing of the momentum-energy dispersions of the cavity and exciton.[115] Due to the large oscillator strength and exciton binding energy of organic materials, organic cavity polaritons exhibit large vacuum Rabi splitting energies ($\hbar\Omega_R$) even at room temperature.[116–118] When $\hbar\Omega_R$ is comparable (20%) to the uncoupled exciton energy (E_{ex}), the system is characterized by the ultrastrong coupling (USC) regime, where the rotating wave approximation (RWA) is no longer applicable, and the antiresonant terms could significantly modify cavity-polariton properties in both single and multiple cavities.[119–122] The hybrid light-matter states are of significant theoretical and practical importance, such as organic LEDs,[123,124] room-temperature polariton condensation and lasing,[125–127] polariton-mediated energy transfer,[128,129] and superfluidity.[130]

Moreover, cavity polaritons are of interest in nonlinear optics, as the nature of hybridization of the light-matter coupled system could provide more degrees of freedom, which can be used to tune the optical properties of the hybrid system. As

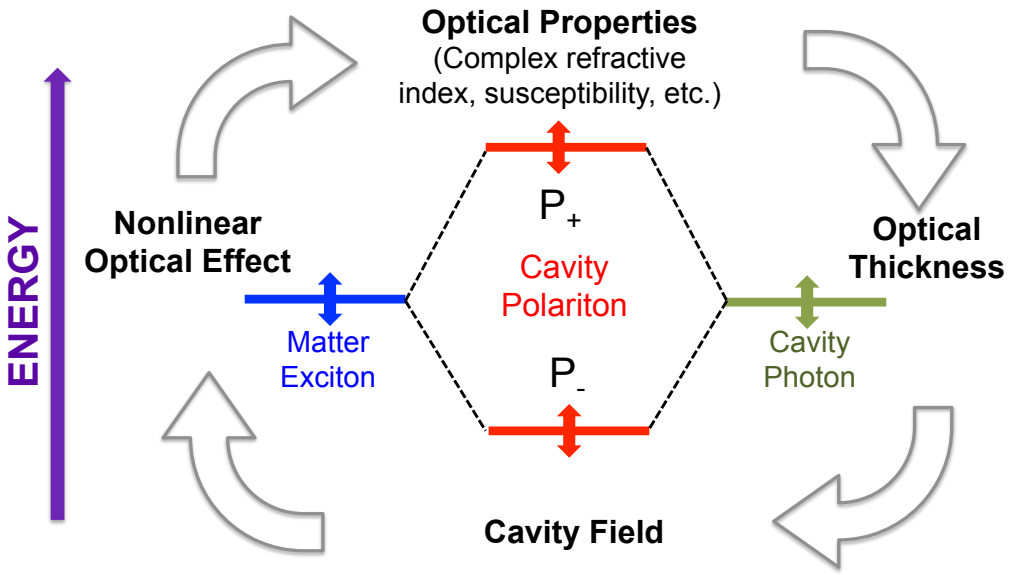

Figure 3.1. Schematic illustration of modification of cavity polariton induced by both linear and nonlinear optical effect. For example, in linear optical regime, the optical thickness can be altered by the physical thickness, refraction, and angle; while the nonlinear optical processes, which are affected by the incident light intensity, susceptibility, and number density, also modify the optical properties of the hybrid light-matter system.

illustrated in Fig. 3.1, in linear optical regime, the optical thickness, which tunes the cavity polariton, can be altered by the physical thickness, index of refraction, and incident angle; while the nonlinear optical processes, which are affected by the incident light intensity, susceptibility, and number density, could also significantly modify the optical properties of the hybrid light-matter system. However, nonlinear optical processes, such as the optical Kerr effect and optical third harmonic generation, arising from cavity polaritons in organic materials are not well studied. Recently, the enhancement of resonant second-harmonic generation (SHG) of the lower polariton is reported from strongly coupled organic crystalline nanofiber microcavities, where

the SH wavelength is resonant with the lower polariton.[131] Also, the enhanced third-harmonic generation (THG) is observed from cavity polaritons in the ultrastrong coupling regime when the pump wavelength is resonant with the lower polariton.[132]

Here, we experimentally demonstrate upper-polariton enhanced THG using angle-varying reflection configuration in the ultrastrong coupling regime, and observe the THG intensity is largest when the THG wavelength is resonant with the upper polariton, in contrast to the observation of Barachati *et al.*,[132] where the pump wavelength they used is resonant with the lower-polariton state. We also show that the enhanced THG is stronger when THG energy (wavelength) is resonant with the cavity polariton state, which is more exciton-like.

3.2 Experimental

3.2.1 Organic Microcavity Fabrication

A 100 nm-thick Ag layer was thermally evaporated onto a 1 mm-thick glass substrate in vacuum at 10^{-7} Torr. DCDHF-6-V was spun cast on top of the metal film, and the thickness of the organic film can be varied by adjusting the spin speed. Microcavity fabrication was completed by evaporating a second 30 nm-thick Ag layer on top of the organic film, which provided microcavities with low Q-factor around 20.

3.2.2 Profilometry and Spectroscopic Ellipsometry

DCDHF-6-V layer thickness was measured using a stylus profilometer (KLA-Tencor P-6). Spectroscopic ellipsometry measurements were carried out with a Horiba Jobin Yvon UVISEL iHR320 ellipsometer under incident angles of 55^o, 60^o, 65^o, for photon energies between 1 eV and 5 eV with 10 meV increment, and the complex refractive

index spectra of DCDHF-6-V were obtained by fitting the ellipsometric data using the Forouhi-Bloomer model (New Amorphous). See Chapter 2 for more details about the ellipsometry modeling.

3.2.3 Linearly Optical Angle-Resolved Reflectivity Measurements

To characterize the linear optical properties of organic microcavities, the linearly optical angle-resolved reflectivity spectra were acquired at room temperature using a J. A. Woollam Co. Inc V-VASE instrument with an angular increment of 5^o and wavelength from 300 to 900 nm with an increment of 2 nm.

3.2.4 Angle-Resolved THG Measurements

The schematic of the THG setup is shown in Fig. 3.2. Infrared wavelengths used as the fundamental pump are generated from a traveling-wave optical parametric amplifier of superfluorescence (TOPAS, Light Conversion Ltd.), which is pumped by a Ti:Sapphire regenerative amplifier (CPA-2010, Clark-MXR) with 1 kHz reparation rate, 200-fs pulse duration and 1 mJ pulse energy. The combination of a polarizing prism and compensator is used to continuously vary the pump power, and a second polarizing prism determines the polarization of the pump beam. A 50.2 mm focal-length lens focuses the beam into the sample, which is placed on the computer-controlled motorized rotation stage, and a second large aperture lens is used to collect the output light. The KG3 (Schott) color filter, narrow band-pass filter (Thorlabs, Inc.) and neutral density filter are used to attenuate the fundamental beam and to verify the detected wavelength is from THG. The data is acquired from a photomultiplier tube (PMT, R1333, Hamamatsu) in combination with a gated BoxCar integrator (SR200 series, Stanford Research Systems). A linear polarizer is placed in front of the PMT

to study the THG polarization. All the components are placed on a rotating arm, which is indicated by the dashed box in Fig. 3.2.

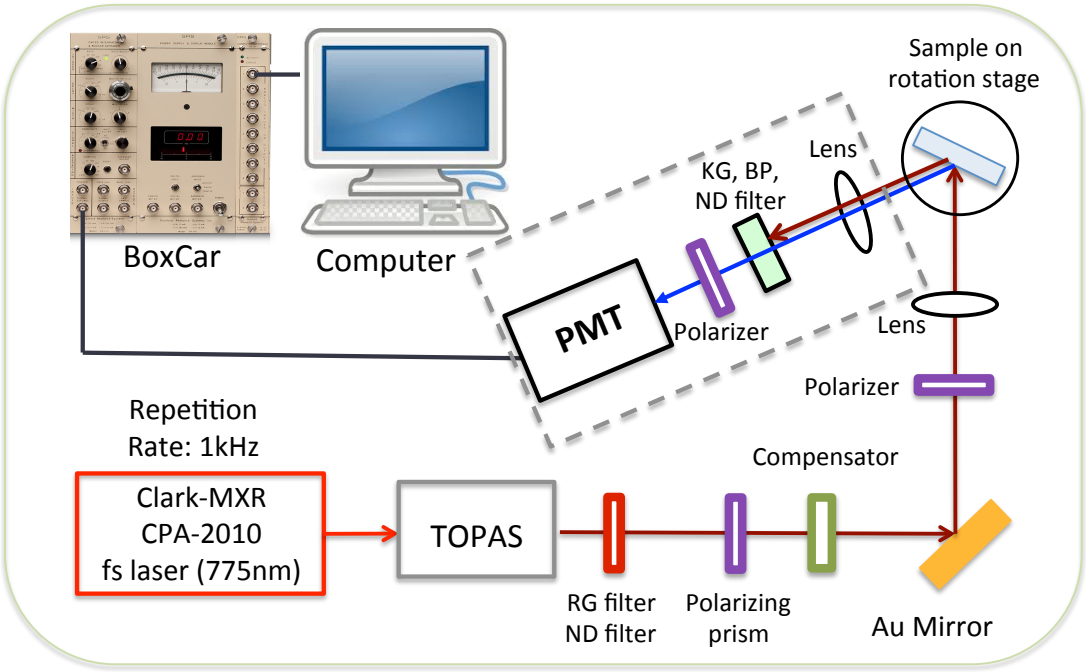

Figure 3.2. Schematic setup of angle-resolved THG experiment. BP: narrow band-pass filter; ND: neutral density filter; PMT: photomultiplier tube.

For all pump fundamental wavelengths, the same area of each sample is tested by varying the incident angle from 15^o to 60^o, and also from 60^o to 15^o, in order to check if the measurement results are reproducible and make sure there is no permanent damage to each sample. A 30 nm-thick Ag film is also tested, and no significant THG signal is observed using the same pump powers as for microcavity samples. Furthermore, using the linear polarizer in front of the PMT, only TE-polarized THG is detected when the cavity samples are pumped by TE-polarized fundamental wavelengths.

3.3 Results and Discussion

3.3.1 Linear and Nonlinear Characterization of a 165 nm Organic Cavity

Fig. 3.3(a) shows the angularly resolved TE-polarized reflectivity spectra of a 165 nm-thick organic microcavity at room temperature. To obtain the vacuum Rabi splitting, $\hbar\Omega_R$, correctly from the measurement results, we plot the energy position of the reflectivity dips as a function of the wave vector ($k = (2\pi\lambda)\sin\theta$), yielding that $\hbar\Omega_R = 1.12 \pm 0.01$ eV from the anticrossing dispersion (Fig. 3.3(b)), which is about 52% of the uncoupled exciton energy, thus indicating ultrastrong exciton-photon coupling in the microcavity. The dispersion of the cavity polariton calculated using the linear transfer matrix formalism are shown by the black solid lines in Fig. 3.3, which are in quantitative agreement with the measurement results.

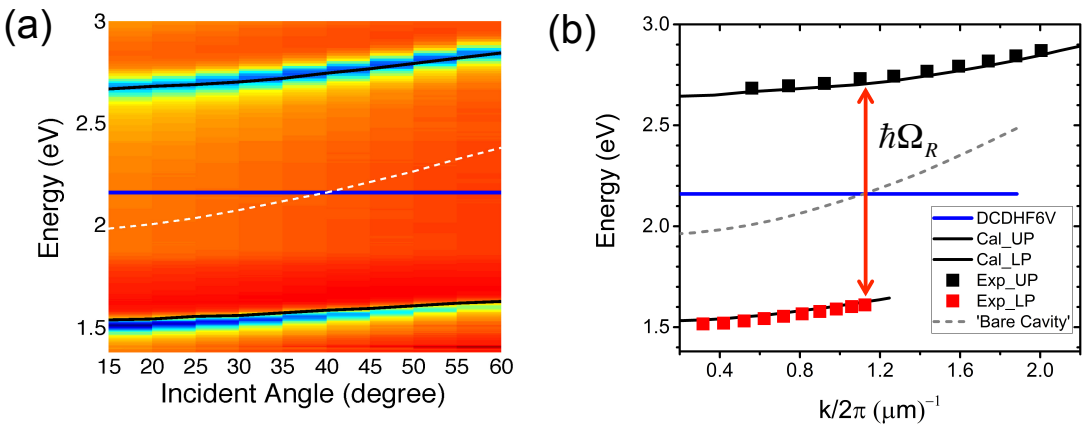

Figure 3.3. (a) Angle-resolved TE-polarized reflectivity map of a 165 nm-thick organic microcavity. The black solid lines show the calculated polariton dispersion using the linear transfer matrix method. The dashed curve is the dispersion of bare cavity mode, and the blue line shows the uncoupled exciton energy of DCDHF-6-V. (b) TE-polarized reflectivity dip energy as a function of the wave vector for the 165 nm-thick cavity. The red arrow indicates the vacuum Rabi splitting of $\hbar\Omega_R = 1.12$ eV.

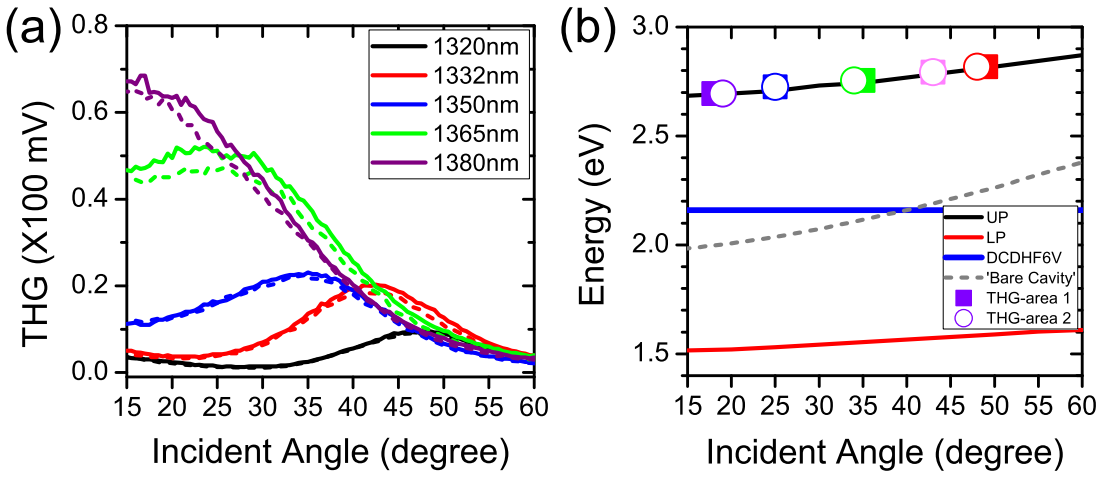

Figure 3.4. (a) Angle-resolved reflected THG intensity of the 165 nm-thick cavity pumped by different fundamental wavelengths, and the pump power is fixed as 1.3 0.2 mW. (b) THG energy versus the incident angle at which the peak THG intensity is generated, following the dispersion of the upper-polariton branch. Solid squares show the results in (a), and the circles represent the results from a different measurement area of the same microcavity. The squares and circles with color changing from violet to red represent the THG intensity monotonically decreases.

Next, the angle-resolved TE-polarized THG measurements are performed with the ultrastrongly coupled microcavity pumped by different fundamental wavelengths. Fig. 3.4(a) shows the measured THG results for the 165 nm-thick organic microcavity. For each pump wavelength, the THG is measured by varying the incident angle from 15^o to 60^o (solid curves in Fig. 3.4(a)), and also from 60^o to 15^o (dashed curves), indicating the reproducibility of the measurements. Importantly, to verify the detected signals arise from THG, the peak THG intensity for different pump wavelengths at particular angles is measured as a function of the pump power (Fig. 3.5), which can fit well by a cubic-power function in Fig. 3.5(d), indicating the key characteristic of THG. As shown in Fig. 3.4(a), the THG intensity has a peak at a particular incident angle for each pump wavelength, and the angular position of the peak THG intensity

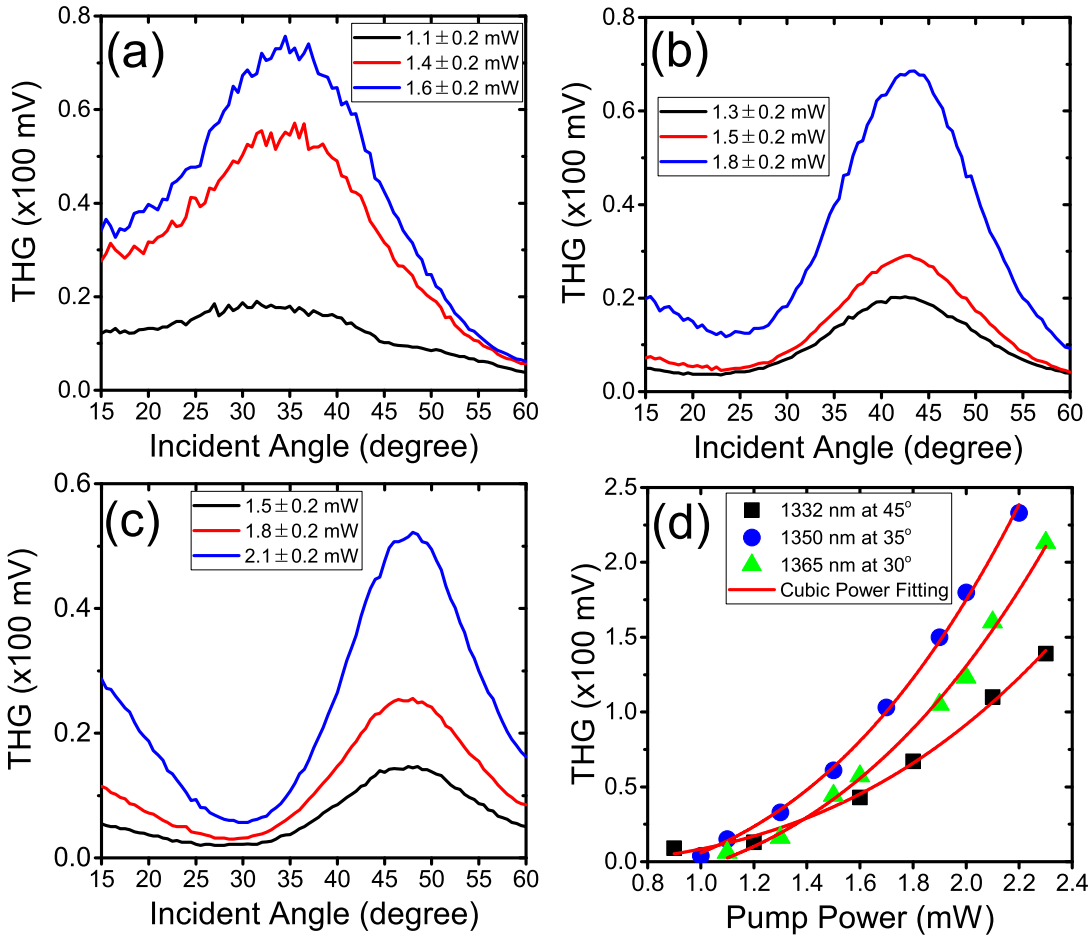

Figure 3.5. Angle-resolved reflected THG of the 165 nm-thick microcavity under different pump powers. Fundamental wavelength: (a) 1350 nm; (b) 1332 nm; (c) 1320 nm. (d) Measured THG intensity as a function of pump power for different wavelengths, and the red curves indicate the cubic power fitting.

shifts when the pump wavelength varies. Furthermore, for a fixed pump power, the longer (lower) the pump wavelength (energy), the larger the peak THG intensity. Thus, the angle values of the peak THG intensity for different pump wavelengths are plotted with the cavity-polariton dispersions in Fig. 3.4(b), and two different areas of the microcavity sample are tested. Also, the variation of the THG intensity is indicated by the change of the symbols color from violet to red in Fig. 3.4(b).

Two important observations should be emphasized, first, the THG energy (wavelength) with the angle of the peak THG intensity for different pump wavelengths follow the dispersion of the upper polaritons, which is the strong evidence of resonant cavity-polariton enhancement effect for THG. Second, the THG intensity is larger when the pump energy (wavelength) is lower (longer), corresponding that the cavity-polariton state resonant with the THG energy (wavelength) is more exciton-like, which is closer to the uncoupled exciton energy. This observation implies that the nonlinear characteristic of organic dye molecules in the cavity-polariton state plays a more significant role in the THG intensity for the hybrid light-matter system.

3.3.2 Linear and Nonlinear Characterization of a 140 nm and 155 nm-thick Organic Cavity

To investigate if the experimental observation is reproducible, a 140 nm and 155 nm-thick organic microcavity are also studied by angularly resolved reflectivity measurements in the linear regime and angle-resolved THG measurements.

In the linear optical regime, the angularly resolved TE-polarized reflectivity spectra of both organic microcavities are shown in Fig. 3.6. Comparing with Fig. 3.3(a), we can clearly find that the incident angle for exciton-cavity photon resonance shifts: for the 165 nm cavity, exciton-cavity photon resonance occurs at $\sim 40^o$, while the resonance occurs at $\sim 35^o$ for the 155 nm cavity, and at $\sim 15^o$ for the 140 nm cavity, respectively, which is strongly determined by the cavity dispersion (dashed curves in Fig. 3.6). To obtain the vacuum Rabi splitting, $\hbar\Omega_R$, the energetic positions of the reflectivity dips are plotted as a function of the wave vector for both cavities (Fig. 3.7), which also yields a vacuum Rabi splitting of $\hbar\Omega_R = 1.12 \pm 0.01$.

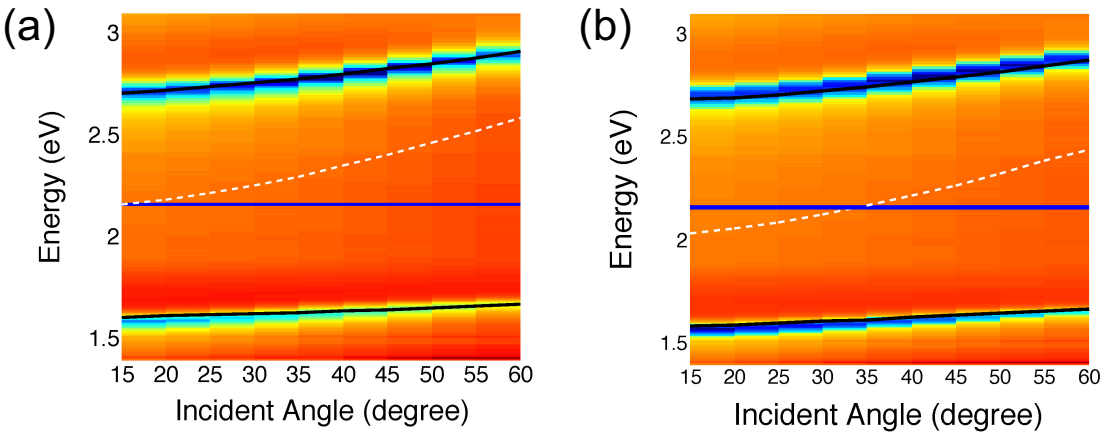

Figure 3.6. (a) Angle-resolved TE-polarized reflectivity map of a 140 nm-thick organic microcavity. The black solid lines show the calculated polariton dispersion using the linear transfer matrix method. The dashed curve is the dispersion of bare cavity mode, and the blue line shows the uncoupled exciton energy of DCDHF-6-V. (a) Angle-resolved TE-polarized reflectivity map of a 155 nm-thick organic microcavity.

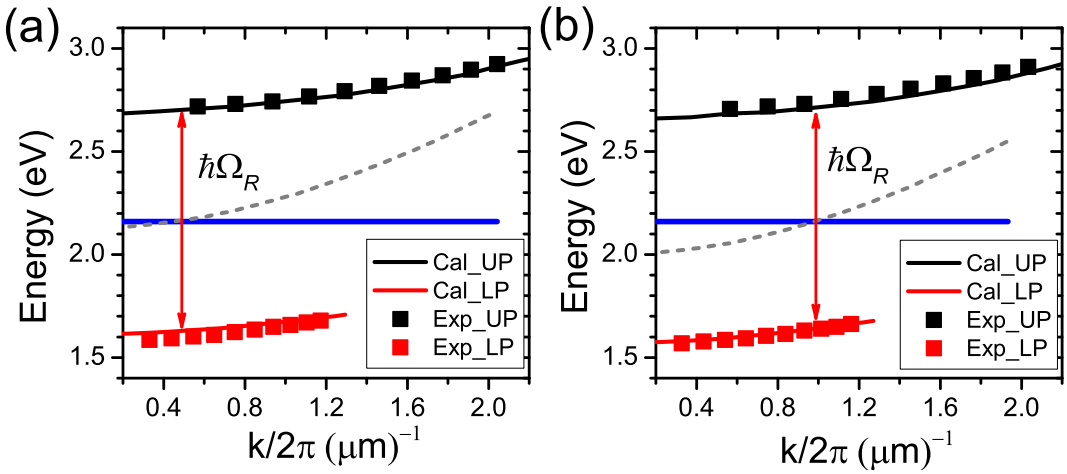

Figure 3.7. TE-polarized reflectivity dip energy as a function of the wave vector: (a) the 140 nm-thick cavity, (b) the 155 nm-thick cavity. Scattered squares represent experimental data. The black and red solid curves show the calculated polariton dispersion using the linear transfer matrix method, and the dashed curve indicates the dispersion of bare cavity mode.

In the nonlinear optical regime, the angle-resolved TE-polarized THG are measured with both cavities. In Fig. 3.8, the angle values of the peak THG intensity for different pump wavelengths are displayed for both cavities, which again follow the dispersion of the upper-polariton branch, suggesting the cavity-polariton enhanced THG. Moreover, for a constant pump power, the THG intensity is larger when the cavity-polariton state resonant with the THG wavelength is more exciton-like.

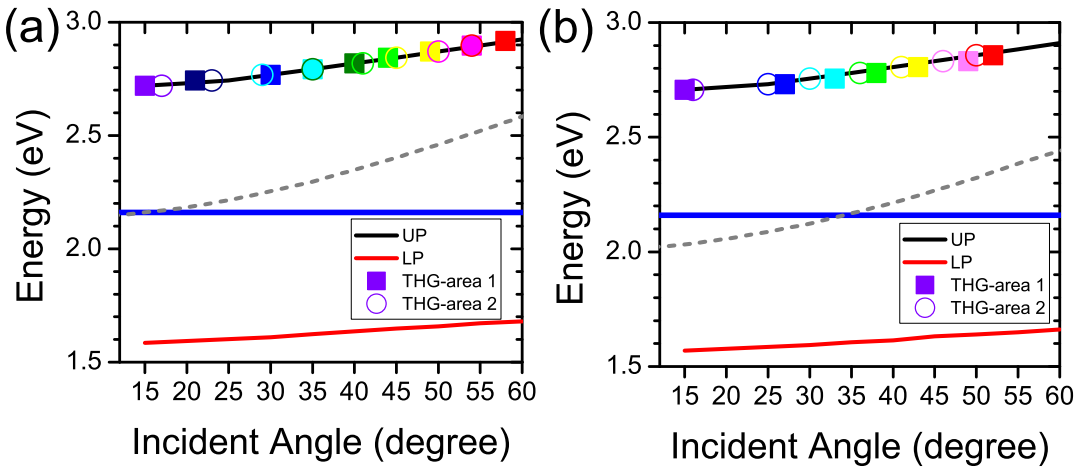

Figure 3.8. THG energy versus the incident angle at which the peak THG intensity is generated, following the dispersion of the upper-polariton branch. (a) the 140 nm-thick cavity, (b) the 155 nm-thick cavity. Squares and circles are the experimental data from two different areas of the same cavity, and the color changing from violet to red represent the THG intensity monotonically decreases.

3.4 Conclusion

In summary, we demonstrate ultrastrong exciton-photon coupling in organic microcavities at room temperature. Using angle-resolved THG technique, we observe that the THG of the organic microcavities is enhanced when the generated energy (wavelength) is resonant with the upper-polariton state, and the THG intensity is larger

when the THG energy is closer to the uncoupled exciton energy of the organic materials. Our work showing very large Rabi splittings in low-Q metal-based organic microcavities at room temperature could lead to promising optoelectronic applications, and the large nonlinear optical response of cavity polaritons could provide potentials for fundamental and applied nonlinear optics.

References

[115] C. Weisbuch, M. Nishioka, A. Ishikawa, and Y. Arakawa, "Observation of the coupled exciton-photon mode splitting in a semiconductor quantum microcavity," Phys. Rev. Lett. **69**, 3314 (1992).

[116] D. G. Lidzey, D. D. C. Bradley, M. S. Skolnick, T. Virgili, S. Walker, and D. M. Whittaker, "Strong exciton-photon coupling in an organic semiconductor microcavity," Nature **395**, 53 (1998).

[117] D. G. Lidzey, D. D. C. Bradley, T. Virgili, A. Armitage, M. S. Skolnick, and S. Walker, "Room temperature polariton emission from strongly coupled organic semiconductor microcavities," Phys. Rev. Lett. **82**, 3316 (1999).

[118] R. J. Holmes and S.R. Forrest, "Strong exciton-photon coupling in organic materials," Org. Electron. **8**, 77 (2007).

[119] Y. Todorov, A. M. Andrews, R. Colombelli, S. De Liberato, C. Ciuti, P. Klang, G. Strasser, and C. Sirtori, "Ultrastrong light-matter coupling regime with polariton dots," Phys. Rev. Lett. **105**, 196402 (2010).

[120] S. Kéna-Cohen, S. A. Maier, and D. D. C. Bradley, "Ultrastrongly coupled exciton-polaritons in metal-clad organic semiconductor microcavities," Adv. Opt. Mater. **1**, 827 (2013).

[121] S. Gambino, M. Mazzeo, A. Genco, O. Stefano, S. Savasta, S. Patanè, D. Ballarini, F. Mangione, G. Lerario, D. Sanvitto, and G. Gigli, "Exploring light-matter interaction phenomena under ultrastrong coupling regime," ACS Photonics **1**, 1042 (2014).

[122] B. Liu, P. Rai, J. Grezmak, R. J. Twieg, and K. D. Singer, "Coupling of exciton-polaritons in low-Q coupled microcavities beyond the rotating wave approximation," Phys. Rev. B **92**, 155301 (2015).

[123] M. Mazzeo, A. Genco, S. Gambino, D. Ballarini, F. Mangione, O. Di Stefano, S. Patanè, S. Savasta, D. Sanvitto, and G. Gigli, "Ultrastrong light-matter coupling in electrically doped microcavity organic light emitting diodes," Appl. Phys. Lett. **104**, 233303 (2014).

[124] C. R. Gubbin, S. A. Maier, and S. Kéna-Cohen, "Low-voltage polariton electroluminescence from an ultrastrongly coupled organic light-emitting diode," Appl. Phys. Lett. **104**, 233302 (2014).

[125] S. Kéna-Cohen and S. R. Forrest, "Room-temperature polariton lasing in an organic single-crystal microcavity," Nat. Photonics **4**, 371 (2010).

[126] K. S. Daskalakis, S. A. Maier, R. Murray, and S. Kéna-Cohen, "Nonlinear interactions in an organic polariton condensate," Nat. Mater. **13**, 271 (2014).

[127] J. D. Plumhof, T. Stöferle, L. Mai, U. Scherf, and R. F. Mahrt, "Room-temperature Bose-Einstein condensation of cavity exciton-polaritons in a polymer," Nat. Mater. **13**, 247 (2014).

[128] D. M. Coles, N. Somaschi, P. Michetti, C. Clark, P. G. Lagoudakis, P. G. Savvidis, and D. G. Lidzey, "Polariton-mediated energy transfer between organic dyes in a strongly coupled optical microcavity," Nat. Mater. **13**, 712 (2014).

[129] X. Zhong, T. Chervy, S. Wang, J. George, A. Thomas, J. A. Hutchison, E. Devaux, C. Genet, and T. W. Ebbesen, "Non-radiative energy transfer mediated by hybrid light-matter states," Angew. Chem. Int. Ed. **55**, 6202 (2016).

[130] G. Lerario, A. Fieramosca, F. Barachati, D. Ballarini, K. S. Daskalakis, L. Dominici, M. De Giorgi, S. A. Maier, G. Gigli, S. Kéna-Cohen, and D. Sanvitto, "Room-temperature superfluidity in a polariton condensate," Nat. Phys. **13**, 837 (2017).

[131] T. Chervy, J. Xu, Y. Duan, C. Wang, L. Mager, M. Frerejean, J. A. W. Münninghoff, P. Tinnemans, J. A. Hutchison, C. Genet, A. E. Rowan, T. Rasing, and T. W. Ebbesen, "High-efficiency second-harmonic generation from hybrid light-matter states," Nano Lett. **16**, 7352 (2016).

[132] F. Barachati, J. Simon, Y. A. Getmanenko, S. Barlow, S. R. Marder, and S. Kéna-Cohen, "Tunable third-harmonic generation from polaritons in the ultrastrong coupling regime," ACS Photonics (2017).

4 Optical Properties and Modeling of 2D Perovskite Solar Cells

4.1 Introduction

Since perovskite compounds were first introduced as an inorganic sensitizer materials in dye-sensitized solar cells in 2009,[133] a wide spectrum of research has been carried out on three-dimensional (3D) perovskite compounds of the form AMX_3 (A = Cs^+, $CH_3NH_3^+$, or $HC(NH_2)_2^+$); M=Sn^{2+} or Pb^{2+}; and X = Cl^-, Br^-, I^-), and significant progress in device performance has been achieved.[134–136] State-of-the-art perovskite-based solar cells deliver promising power-conversion-efficiencies (PCEs) of over 22%, approaching the Shockley-Queisser limit for a single-junction solar cell. Nevertheless, the moisture sensitivity of the 3D perovskites still remains a major concern in commercializing this technology.[137] To overcome this stability issue, new promising candidate materials have emerged for optoelectronic applications, which are derivatives of AMX_3, obtained by opening the 3D network and inserting long chain hydrocarbon cations between the perovskite layers. These materials form two-dimensional (2D) layered structures and can be considered as naturally occurring multiple quantum wells (QW), where the thickness of the inorganic slab (m) defines the QW width, and the organic spacer acts as the barrier.

Recently, our collaborators at Northwestern University demonstrated synthetic routes to phase-pure members of the Ruddlesden-Popper (RP) phase metal iodide perovskite series utilizing different organic spacers between the inorganic layers, and promising solar cell performance is observed in the $(BA)_2(MA)_{m-1}Pb_mI_{3m+1}$ (BA = $CH_3(CH_2)_3NH_3^+$, MA = $CH_3NH_3^+$, $m = 1 - 4$),[138–141] affording a maximum PCE of 12.5%, exhibiting greatly improved stability by producing thin films of near-single-crystalline quality.[142] For further advancing these emerging RP perovskite materials, it is essential to have a fundamental understanding of their optical and electronic properties.

Here we investigate how the optical properties and optical-frequency dielectric constants of the series of $(BA)_2(MA)_{m-1}Pb_mI_{3m+1}$ films vary as a function of QW or perovskite slab thickness (m), and the crystal structures of the compounds are shown in Fig. 4.1.[139,140] It will be seen that the experimental dielectric constants qualitatively follow a similar trend, exhibiting increased dielectric screening with increasing m. In addition, we find a sensitivity of the optical constants to the thin film microstructures formed by different film processing methods.

Moreover, we employ transfer matrix theory with complex index of refraction obtained by spectroscopic ellipsometry, to simulate absorption of $(BA)_2(MA)_4Pb_5I_{16}$ in an inverted planar solar cell device for various wavelengths, while varying the thickness of 2D perovskite layer, and find that it displays cavity-induced absorption enhancement.[143–146] Guided by this absorption profile, we describe a modified drift-diffusion model to optimize the photocurrent in the UV-Vis region of a complete solar cell device. Our model takes into account the charge-carrier recombination in the planar device architecture, which is an important parameter for determining charge

extraction and collection, and has been previously neglected in similar optical analyses.[147,148] After confirming the consistency of our modeling results for 3D perovskite solar cells with previously reported experimental data,[149] we extend our investigation to 2D RP perovskites and investigate $(BA)_2(MA)_4Pb_5I_{16}$ ($m = 5$) as a representative case due to its broader absorption spectrum and smaller dielectric constant than the lower-m members of the series. By using inputs from the experimental photovoltaic parameters as a function of perovskite film thickness in our drift-diffusion model, we predict the charge-carrier recombination constant of $(BA)_2(MA)_4Pb_5I_{16}$ which is found to be one order of magnitude larger than in the 3D parent compound. The present work, exploiting the cavity-tuned absorption enhancement with consideration of charge-carrier recombination, represents a novel design tool aiming to qualitatively boost the device efficiency for RP perovskite-based planar photovoltaic architectures.

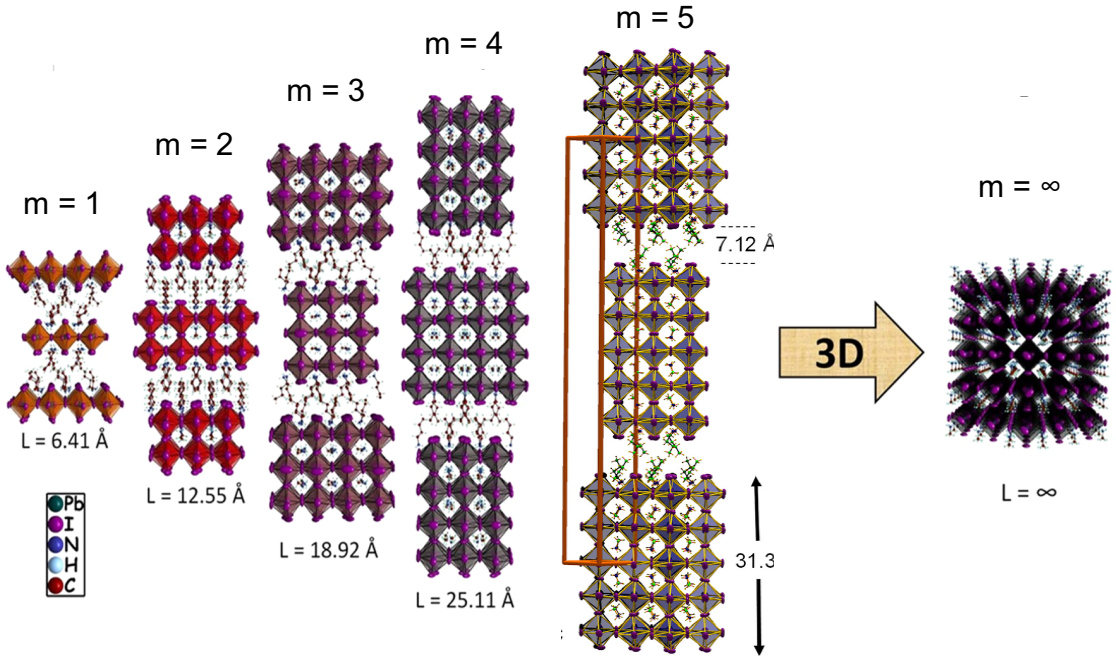

Figure 4.1. Crystal structures of the 2D lead iodide perovskites, $(BA)_2(MA)_{m-1}Pb_mI_{3m+1}$, extending from $m = 1$ to $m = \infty$.[139,140]

4.2 Experimental

4.2.1 Materials and Device Fabrication

- *Materials*: All reagents were used as received from Sigma-Aldrich without further purification: lead oxide (PbO, 99%), methylamine hydrochloride (MACl, 99%), hydriodic acid (HI, 57 wt% in H_2O), hypophosphorous acid (H_3PO_2, 50 wt% in H_2O), n-butylamine (BA, 99.5%), poly(3,4-ethylenedioxythiophene)-poly(styrenesulfonate) (PEDOT:PSS, 1.3wt % dispersion in H_2O, conductive grade), phenyl-C61-butyric acid methyl ester ($PC_{61}BM$, 99.9%), N,N-dimethylformamide (DMF, anhydrous, 99.8%), and chlorobenzene (CB, anhydrous, 99.8%).

  Perovskite crystals of $(BA)_2(MA)_{m-1}Pb_mI_{3m+1}$ $(m = 2-5)$ were synthesized according to previously reported procedure.[138–140]

- *Substrate Cleaning*: Patterned ITO-coated glass (150 nm, 7 Ω/sq, Thin Film Devices Inc.) or microscope glass substrates were cleaned by sequential sonication in aqueous detergent, deionized water, acetone (ACE), and isopropanol (IPA) for 15 min each, followed by a 5 min oxygen plasma treatment.

- *Perovskite Film Preparation*: Here we employ two film processing methods, namely, **hot-casting** and **post-annealing**. The 2D perovskite solutions of 0.225 M concentrations were prepared by dissolving the $(BA)_2(MA)_{m-1}Pb_mI_{3m+1}$ $(m = 2-5)$ crystals in DMF solvent. For hot-cast films, the pre-cleaned microscope glass substrates were pre-heated at 110 °C for 10 min before spin-coating 100 μl of the as-prepared solutions at 5,000 rpm. for 20 s. For post-annealed films, the solutions were spin-cast at 3,000 rpm. for 30 s and annealed at 85 °C for 5 min. The entire process was conducted in an argon-filled glove box. The 3D $MAPbI_3$ film was prepared by sequential deposition method. 1 M PbI_2 in DMF was spincoated at

6,500 rpm. for 60s and dried at 70 °C for 30 min. After cooling it to RT, the film was dipped in 10 mg/ml MAI solution for 30 s and dried at 70 °C for 30 min. The entire process was conducted in a humidity-controlled box with $< 3\%$ RH.

- *Device Fabrication*: A thin layer of PEDOT:PSS ($\sim$40 nm) was deposited on the clean ITO substrates by spin-coating at 6,000 rpm. for 30 s and annealing at 150 °C for 30 min in air. The substrates were then transferred to an argon glove box to complete the device fabrication. Various concentrations of $(BA)_2(MA)_4Pb_5I_{16}$ (0.1125 M, 0.225 M, 0.3 M, and 0.45 M) were prepared by dissolving the $(BA)_2(MA)_4Pb_5I_{16}$ crystals in DMF solvent. Perovskite layers were fabricated by pre-heating the ITO/PEDOT:PSS substrates at 110 °C for 10 min before spin-coating 100 μl of the as-prepared solutions at 5,000 rpm. for 20 s. $PC_{61}BM$ layer was deposited on the perovskite film from a 20 mg/ml solution in CB at 5,000 rpm. for 40 s. Finally, 150 nm of Al was thermally evaporated through a shadow mask at a pressure of $\sim 8\times10^{-7}$ Torr. The devices were encapsulated by using a cover slide and UV-curable epoxy, which was cured for 15 min under a UV lamp. For testing, the devices are masked with black tape to avoid edge effects for small area solar cells. The area is defined to be 0.03 cm^2.

4.2.2 Device Characterization

Current density vs. voltage (J-V) data were collected in air using a Keithley 2100 source meter under simulated AM 1.5G irradiation (100 mW/cm^2) generated by a xeon-lamp-based solar simulator (Oriel LCS-100). The light intensity was calibrated by using an NIST-certified monocrystalline Si reference cell (Newport 532, ISO1599) to reduce the spectral mismatch. The external quantum efficiency was measured with a NIST calibrated monochromator (QEX10, 22562, PV measurement INC.) in

the AC mode. The light intensity was first calibrated with a NIST calibrated photodiode (91005) as a reference before each measurement. During the measurement, the monochromator was chopped at a frequency of 150 Hz, the photocurrent was collected at short circuit condition through a lock-in amplifier. Quantum efficiency was calculated by software integrating the measured photocurrent for the device and the standard reference cell.

4.2.3 Absorption, Ellipsometry and Profilometry Measurements

Absorption spectra of perovskite films were measured with a Cary 300 UV-Vis spectrophotometer between 300 and 900 nm with 1 nm increment. Complex refractive index spectra of the materials used were determined using variable angle spectroscopic ellipsometer (Horiba Jobin Yvon UVISEL iHR320) between 300 and 2000 nm with 10 nm increment. Perovskite film thicknesses were measured using a stylus profilometer (KLA-Tencor P-6).

4.3 Results and Discussion

4.3.1 Optical Properties of 2D Perovskite Films

The refractive index of perovskite films are determined nondestructively by spectroscopic ellipsometry over a broad spectral range. To fit the ellipsometry measurement data taking the nanocrystalline nature of the 2D perovskite films into account, we use the Forouhi-Bloomer model in the parametrization of Jobin Yvon (new amorphous)

for the complex refractive index,[150,151]

$$n(\omega) = n_\infty + \sum_{j=1}^{N} \frac{B\,(E - E_j) + C}{(E - E_j) + \Gamma_j^2} \tag{4.1a}$$

$$k(\omega) = \begin{cases} \sum_{j=1}^{N} \dfrac{f_j\,(E - E_g)^2}{(E - E_j) + \Gamma_j^2} & E > E_g \\ 0 & E \leq E_g \end{cases} \tag{4.1b}$$

where

$$B = \frac{f_j}{\Gamma_j}\left(\Gamma_j^2 - (E_j - E_g)^2\right) \tag{4.2a}$$

$$C = 2 f_j \Gamma_j\,(E_j - E_g) \tag{4.2b}$$

where n and k are real and imaginary part of index of refraction, which are dispersive and depend on energy (frequency) E. E_g is the bandgap, E_j, f_j and Γ_j are the resonance energy, strength, and width of one oscillator, respectively. All fitting parameters for hot-cast (HC) and post-annealed (PA) 2D perovskite films are listed in Table 4.1, where the small χ^2 values illustrate an excellent agreement between the experimental data and the model. For simplicity, thin films of $(BA)_2(MA)_{m-1}Pb_mI_{3m+1}$ ($m = 2 - 5, \infty$) are abbreviated as Pb2 - Pb5 and 3D perovskite, respectively.

To investigate the optical properties of 2D RP phase perovskite films as a function of QW thickness (m), we compare their optical constants (complex refractive indices, n and k), which are prerequisites for the optical transfer matrix simulations, from the above ellipsometric modeling. The spectral-dependent refractive index upon varying m and between 3D and 2D layered perovskites are shown in Fig. 4.2. The optical constants obtained here for the 3D perovskite $MAPbI_3$ are in excellent agreement with previous reports, with the n value near the bandgap (1.6 eV) being approximately

2.5,[148,150] confirming the validity of the present experimental technique. For each compound, we have tested several samples in order to check the reproducibility for fitting results of the optical constants, shown in Fig. 4.3, and the observed acceptable distinction is due to the unavoidable variation of the film morphology during the deposition process.

Table 4.1. Fitting results of parameters in dispersion function Eq. 4.1 to the ellipsometry measurement data of hot-cast (HC) and post-annealed (PA) 2D perovskite films.

Fitting parameters	HC-Pb2	HC-Pb3	HC-Pb4	HC-Pb5	PA-Pb2	PA-Pb3	PA-Pb4	PA-Pb5	3D
χ^2	4.575	3.981	1.527	1.456	0.221	0.154	0.164	0.198	2.232
d(nm)	193.1	209.8	139.3	167.9	71.58	73.65	65.64	59.57	221.3
n_∞	1.634	1.643	1.791	1.801	1.655	1.632	1.651	1.711	1.938
E_g(eV)	1.920	1.742	1.686	1.640	1.830	1.720	1.620	1.594	1.572
f_1(eV)	0.017	0.102	0.177	0.177	0.018	0.068	0.004	0.018	0.128
E_1(eV)	2.131	1.438	1.774	1.621	2.183	1.550	1.916	1.877	1.599
Γ_1(eV)	0.085	0.160	0.065	0.052	0.100	0.435	0.303	0.183	0.047
f_2(eV)	0.012	0.093	0.155	0.060	0.137	0.146	0.148	0.141	0.074
E_2(eV)	2.793	1.911	2.280	2.339	2.887	1.883	2.861	2.377	2.407
Γ_2(eV)	0.202	0.165	0.482	0.450	0.511	0.305	1.060	0.701	0.355
f_3(eV)	0.134	0.089	0.044	0.063	0.023	0.119	0.047	0.068	0.057
E_3(eV)	3.386	3.352	3.417	3.357	3.589	3.325	3.356	3.387	3.369
Γ_3(eV)	0.605	0.643	0.420	0.497	0.376	0.657	0.495	0.543	0.431

Next, we investigate whether any disparity in optical constants arises from the particular film fabrication technique, hot-casting and post-annealing, where the former method was recently demonstrated to offer significant advantages over the latter.[136] In particular, the more rapid solvent removal and perovskite crystallization rate of hot-casting leads to a compact, uniform film morphology and near-single-crystalline orientation, hence enhanced charge transport in RP phase solar cells.[141,142] Fig. 4.2(**A**) and (**B**) present the real part n of refractive index, while Fig. 4.2(**C**) and (**D**) show

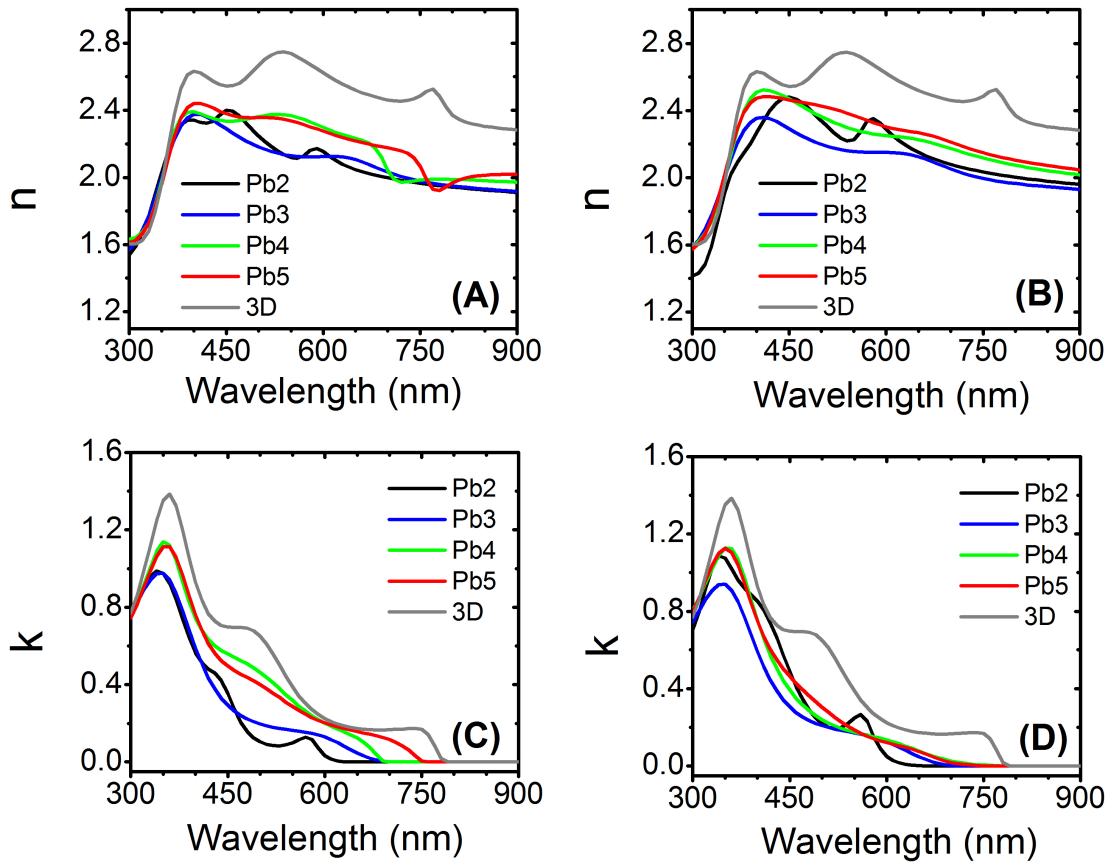

Figure 4.2. Complex refractive index (optical constants) of 2D perovskite (Pb2 - Pb5) and 3D perovskite films. Real part n (**A**) and imaginary part k (**C**) of hot-cast 2D perovskite films. Real part n (**B**) and imaginary part k (**D**) for post-annealed 2D perovskite films.

the imaginary part k (extinction coefficient) for hot-cast and post-annealed 2D perovskite films, respectively. The corresponding n and k plots reveal that thin films of identical 2D perovskite compounds from different processing methods yield different optical constants. This distinction can plausibly be explained by variations in film thickness and the complex nature of solution-processed thin films combined with the sensitivity of optical constants to the material density and surface conditions such as grain size, film roughness, crystallinity, and crystal orientation, especially for RP

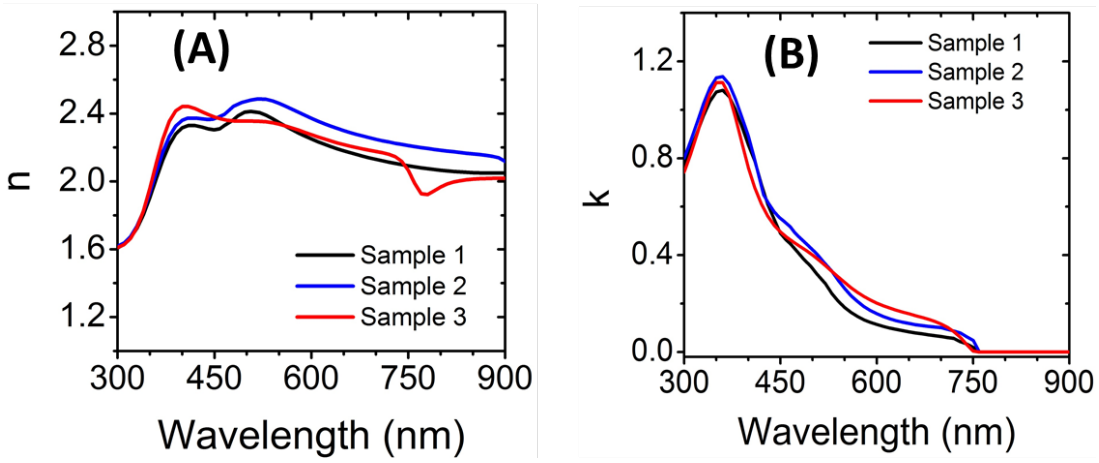

Figure 4.3. Complex refractive index of several hot-casting Pb5 perovskite films. Real part n (**A**) and imaginary part k (**B**).

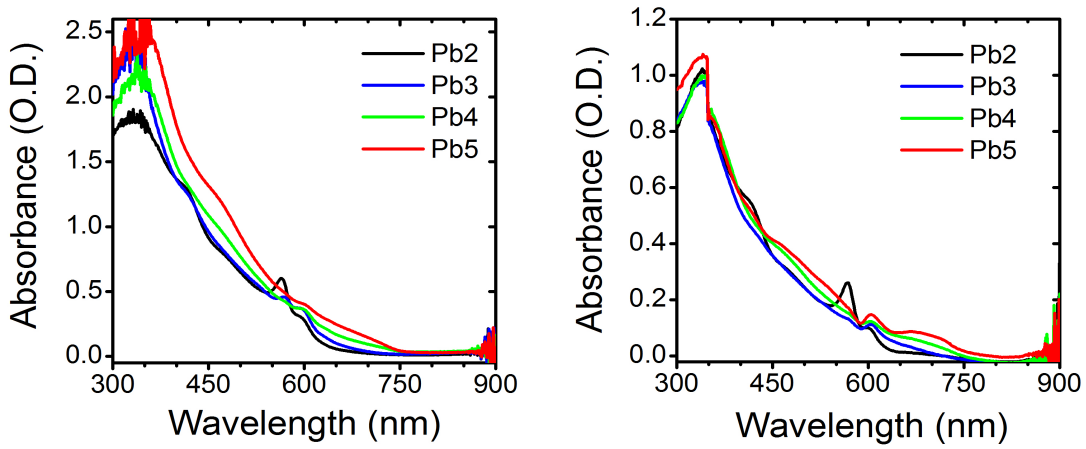

Figure 4.4. Absorbance spectra of (**A**) hot-cast and (**B**) post-annealed 2D perovskite films.

layered perovskites. A similar behavior can be observed in 3D perovskite, where the optical constants of the $MAPbX_3$ films are lower than those of their single crystals due to defects and surface inhomogeneities occurring in solution-processed thin films.[152,153] Furthermore, the measured absorbance spectra of the 2D perovskite films (Fig. 4.4) follow a parallel trend to the ellipsometry fitting results of the extinction coefficient k, which also indicates the the ellipsometry fitting results are satisfactory.

As summarized in Table 4.2, there is a small decrease in band-edge energies evident in both the absorption spectra and the fit with increasing m.

Table 4.2. Band-edge energies of hot-cast and post-annealed 2D perovskite ($m = 2 - 5$) thin films.

Preparation methods	Pb2 (eV)	Pb3 (eV)	Pb4 (eV)	Pb5 (eV)
Hot-casting	1.851	1.746	1.662	1.631
Post-annealing	1.823	1.722	1.653	1.610

4.3.2 Dielectric Constants of 2D Perovskite Films

We next discuss the optical-frequency dielectric constants of the homologous series as they can be derived from n and k. Note that the complex refractive index and the dielectric function are similar in nature and closely related to each other. The refractive index $[\widetilde{n}(\omega) = n(\omega) + ik(\omega)]$ is usually used to describe how a material responds when light propagates through it, whereas the dielectric function $[\varepsilon(\omega) = \varepsilon_1(\omega) + i\varepsilon_2(\omega)]$ is usually used to describe the material's band structure.[154] Fig. 4.5 shows the optical-frequency dielectric constants of the 2D perovskite films, which are derived according to the relation between the dielectric constants and complex refractive index $[\varepsilon_1(\omega) = n^2(\omega) - k^2(\omega), \varepsilon_2(\omega) = 2n(\omega)k(\omega)]$. In the limit of $(\omega \sim \infty)$, we assume $\varepsilon_\infty \sim n_\infty^2$, and $\varepsilon_2(\infty) \sim 0$ for the frequency regime which is far from resonance. Table 4.1 shows that the value of fitting parameter n_∞ increases as QW thickness m increases. Therefore, we can conclude that the value of ε_∞ increases as m varies from Pb2 to Pb5, and 3D perovskite ($m = \infty$) always has a larger ε_∞ than its 2D counterparts (Fig. 4.6**A**). This variation trend of ε_∞ is obtained by estimating

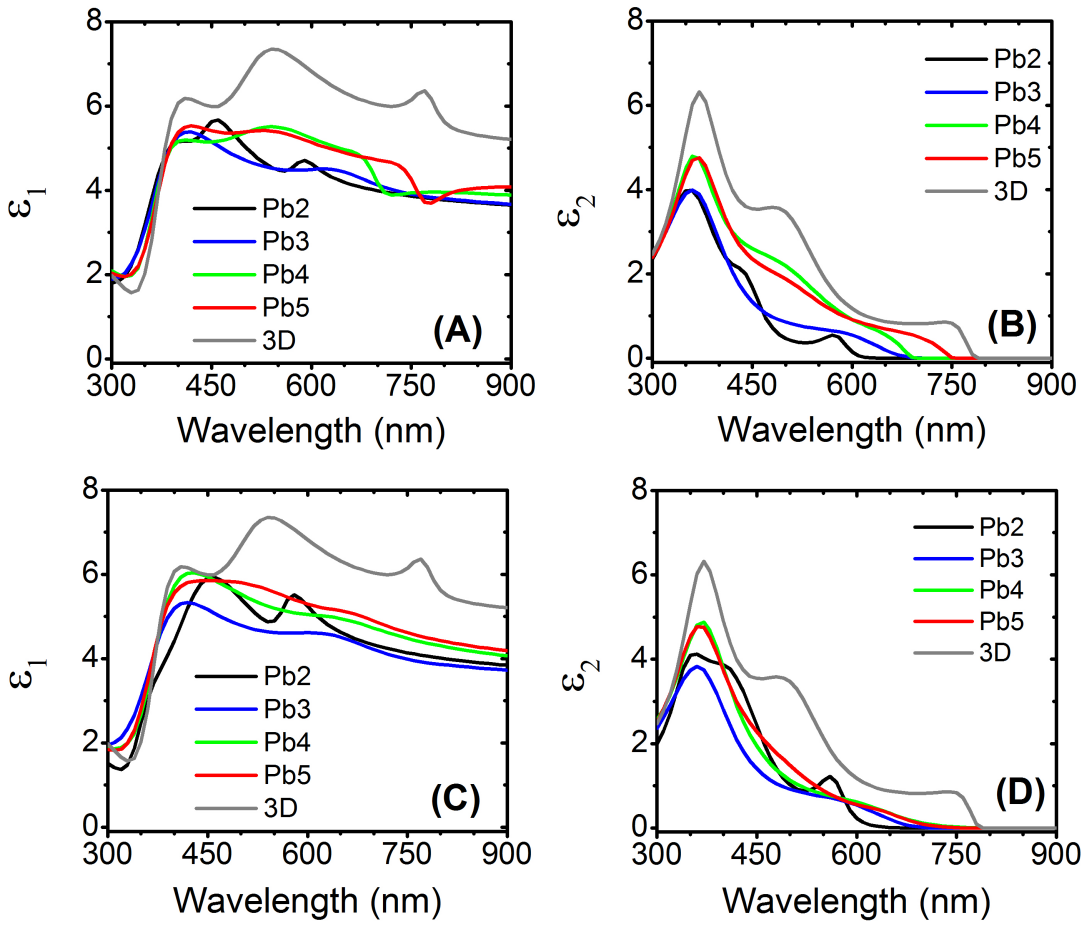

Figure 4.5. Dielectric constants of 2D $(BA)_2(MA)_{m-1}Pb_mI_{3m+1}$ ($m = 2, 3, 4, 5$) perovskite films. Real part ε_1 (**A**) and imaginary part ε_2 (**B**) of hot-cast 2D perovskite films. Real part ε_1 (**C**) and imaginary part ε_2 (**D**) for post-annealed 2D perovskite films. For comparison, dielectric constants of 3D ($m = \infty$) perovskite are included.

the average high-frequency dielectric constant of QWs using a simple mode:[155]

$$\varepsilon_\infty = \frac{\varepsilon_w L_w + \varepsilon_b L_b}{L_w + L_b} \tag{4.3}$$

where ε_w and ε_b are the dielectric constants of the inorganic layer (QW) and the organic spacer layer (barrier), respectively, while L_w and L_b are the well width and the barrier thickness, respectively. For this simple model, we employ $\varepsilon_w = 6.5, \varepsilon_b = 2.1$,

and $L_b = 0.775$ nm, and the most marked changes are produced by the modification of the QW width L_w. The L_w values for Pb2, 3, 4, 5, and 3D perovskite are 1.26, 1.89, 2.52, 3.15, and 315 nm, respectively.[139,140] Fig. 4.6(**B**) displays the calculated results of ε_∞ for 2D perovskites ($m = 1, 2, 3, 4, 5$). Also included is $\varepsilon = 6.5$ for the 3D perovskite, which was established from magnetoabsorption and diffuse reflectance measurements.[156,157] Note that the calculated ε_∞ increases as m increases, following a similar trend as the ellipsometry fitting results of ε_∞. However, the absolute values of ε_∞ from ellipsometric fitting do not agree well with those from the above model, and we rationalize this disparity from the following possibilities: i) the assumption that the well width L_w is the only variable may not always hold for this simple model; the well width L_w and barrier thickness L_b used here are the parameters for single crystals with perfect QWs. However, the solution processed thin films with nm-sized grains in the present study are likely to have imperfect QWs due to the presence of defects in the films; ii) the dielectric constant also has dispersion for the high-frequency range; thus ε_∞ derived from the simple model may fall into a different frequency range from those obtained from ellipsometric fitting.

It is important to consider low-frequency dielectric constants, ε_0, of these materials since they can provide a prediction of how strongly the photo-generated electron-hole pairs are bound and how easily they can be dissociated in the active layer, which prominently influences the photovoltaic efficiency. The ease of charge dissociation in the 3D perovskites comes from the fact that the Coulombic attraction between the photo-generated holes and electrons is weakened by the screening effect of the high dielectric constant of the inorganic lattice. In the 2D perovskites, however, the

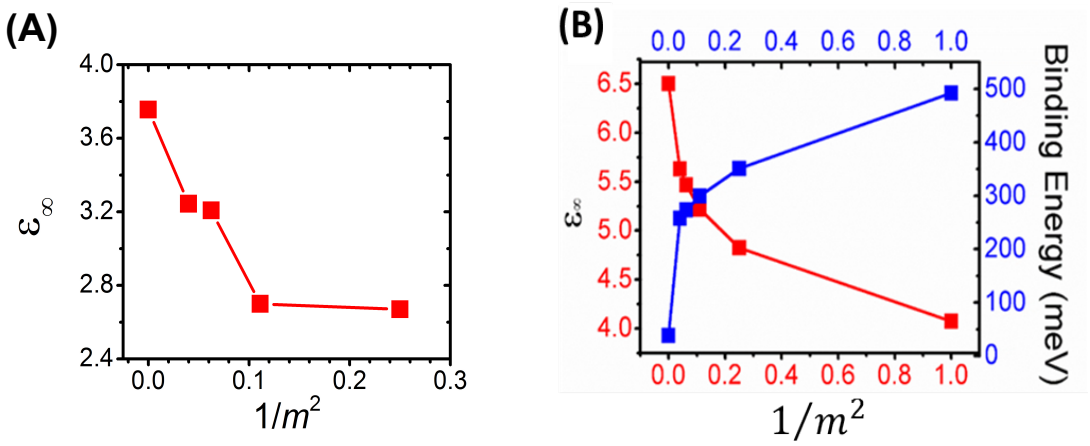

Figure 4.6. High-frequency dielectric constant ε_∞ as a function of number of inorganic layer for 3D ($m = \infty$) and hot-cast 2D ($m = 2, 3, 4, 5$) perovskite films, which are obtained from ellipsometry fitting (**A**); from a simple quantum-well model (**B**).

increase in quantum confinement results in significant anisotropy in the photoconductivity where the conductivity within lead iodide layers is much larger than that across the layers.[158] In addition, due to the dielectric mismatch between inorganic slabs and organic spacers, the exciton binding energy increases with smaller m.[159,160] Based on this consideration, we expect thicker QWs with a larger ε_0, and thus, a smaller exciton binding energy of molecules, such as Pb5, to exhibit higher PCE by tuning the molecular orientation for favorable charge transport.[142,161]

4.3.3 Transfer Matrix Calculations

To understand the optical cavity effects in these emerging materials integrated in a solar cell multilayer structure, we first calculate absorbance spectra of a free-standing 2D perovskite film surrounded by air as a function of the film thickness and wavelength (Fig. 4.7**D**). It is important to note that we do not consider the scattering effect caused by roughness in the multilayer structure for the optical model, and the

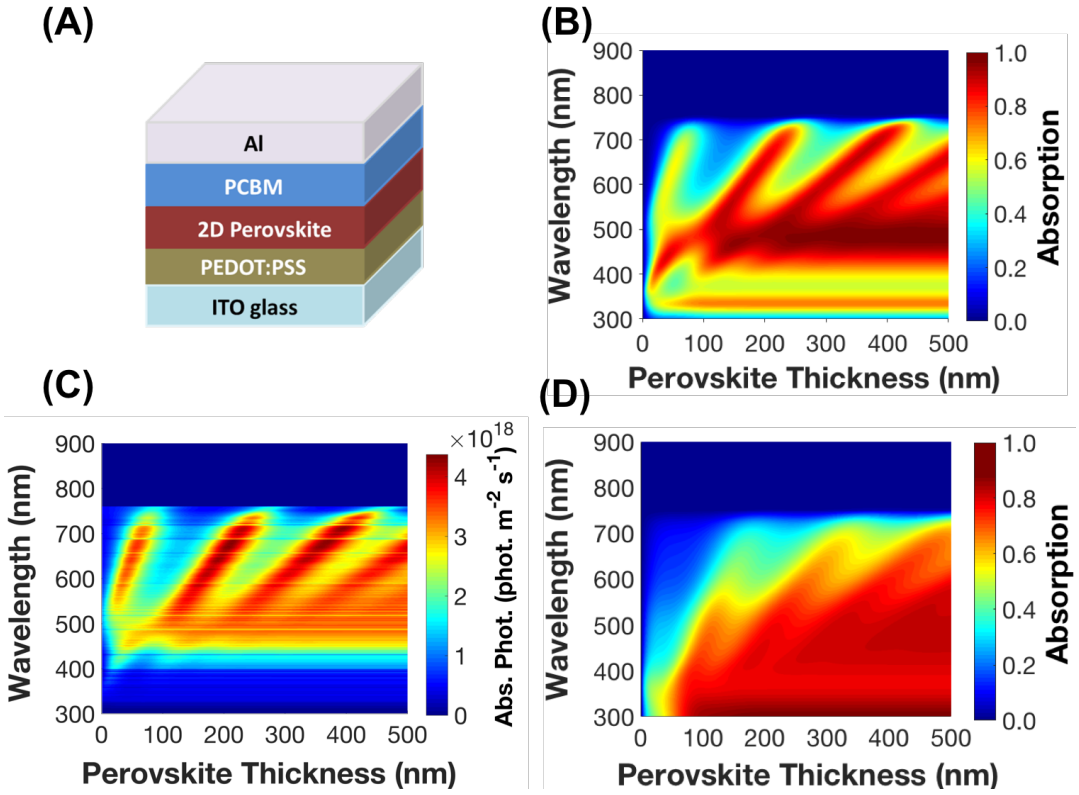

Figure 4.7. (**A**) Diagram illustrating the device architecture. (**B**) Spectral absorption contour versus active layer thickness for a photovoltaic structure consisting of ITO (150 nm)/PEDOT:PSS (40 nm)/Pb5 perovskite (thickness varied)/PCBM (20 nm)/Al (150 nm), calculated by optical transfer matrix theory for thicknesses ranging from 0 to 500 nm. (**C**) Spectral contour depicting absorbed photons in Pb5 perovskite layer using spectral absorption contour of Fig. 4.7(**B**) multiplied by the AM1.5G solar spectrum. (**D**) Absorption contours of a free-standing Pb5 perovskite film in air.

2D perovskite hot-cast films studied exhibit a compact and uniform morphology with a root-mean-square (RMS) roughness of $\sim 10 - 30$ nm, as shown in Fig. 4.8. For these relatively smooth films, we believe the approximation without considering the roughness-induced scattering effect is acceptable. Here we focus on Pb5 as a case scenario, representing the newest member of the homologous series with the largest QW thickness. For a free-standing Pb5 film in air, the absorption profile remains

relatively unchanged, and the absorbance increases nearly monotonically as the film gets thicker, with enhanced absorption in shorter wavelength range between 300 and 420 nm. This behavior is no longer observed when the Pb5 film is stacked in a solar cell device structure and sandwiched between interfacial layers and charge-collecting electrodes (Fig. 4.7**A**). After taking into consideration the optical constants and interference effects from other layers, and using optical transfer matrix calculations,[145,146] the obtained Pb5 absorption (Fig. 4.7**B**) and its total absorbed photons (absorbance multiplied by the AM1.5 solar spectrum) (Fig. 4.7**C**) in the device stack display diagonal contour structures with cavity-induced enhanced absorption. This effect can be described by a frequency pulling model,[145] with an accompanying absorption maxima shift toward the visible region (420-600 nm) compared to a free-standing perovskite film (Fig. 4.7**D**). This is favorable for device designs based on the solar spectrum.

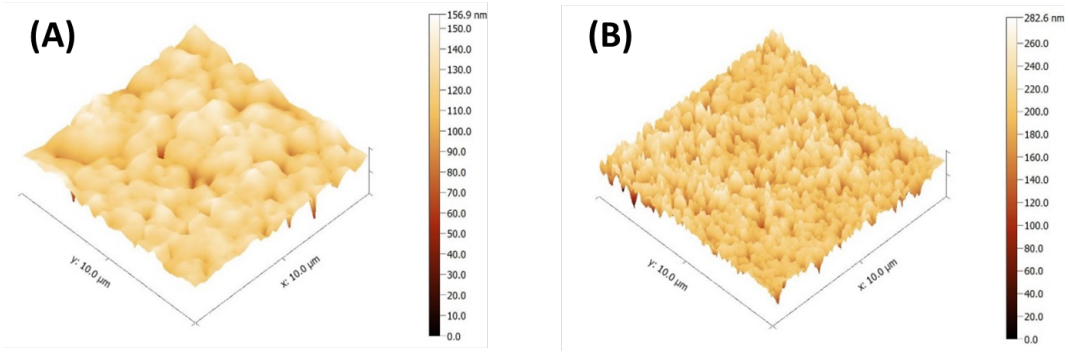

Figure 4.8. (**A**) Atomic force microscope (AFM) image of hot-cast Pb3 film with a roughness of 11.5 nm. (**B**) AFM image of hot-cast Pb5 film with a roughness of 27.5 nm.

Furthermore, the total absorbed photons of Pb2-Pb5 films in a planar device structure are calculated by integrating the absorbance spectra ($300 - 900$ nm) as a function of perovskite film thickness (Fig. 4.9**A**). First, due to the broader absorption spectra, Pb5 absorbs more photons than the lower-m perovskites; second, for each

type of 2D perovskite-based device, notable peaks and troughs of the total absorbed photons are observed and shift with perovskite film thickness due to the cavity effect. Moreover, there is a significant enhancement of absorbed photons in the perovskite films when assembled in a device multilayer structure, whereas no obvious peaks and troughs are observed for free-standing films in air, indicating negligible interference effect and hence absence of cavity structure (Fig. 4.9**B**). According to these simulation results, we find that optical cavity absorption enhancements can be used for thickness optimization in device design since light harvesting is the primary factor for photovoltaic performance.

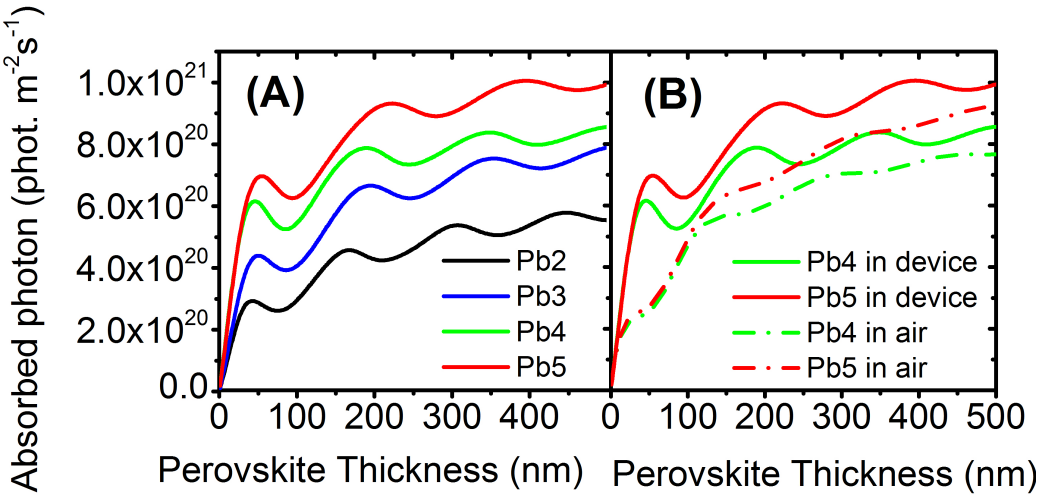

Figure 4.9. (**A**) Total absorbed photons in 2D perovskite layer calculated by transfer matrix theory for a photovoltaic structure consisting of ITO (150 nm)/PEDOT:PSS (40 nm)/2D perovskite (0-500 nm)/PCBM (20 nm)/Al (150 nm). (**B**) Total absorbed photons in 2D perovskite (Pb4 and Pb5) layer for device and surrounded by air.

4.3.4 Charge-Carrier Recombination

While optical modeling of the active layer gives some insights into the cavity effects, its absorption alone does not provide a complete description of photocurrent in the

device. Charge-carrier recombination needs to be taken into consideration since some photo-generated electron-hole pairs recombine instead of being extracted to the electrodes, which is a crucial loss mechanism in the organic photovoltaic and modest mobility perovskite-based devices.[138,162] This competition between charge carrier extraction and recombination is illustrated by the fill factor of the device. Hence, on the basis of transfer matrix simulation results for absorbed photons, we use/propose a simple modified drift-diffusion model for perovskite solar cell devices, considering monomolecular charge-carrier recombination (trap-assisted recombination) and bimolecular charge-carrier recombination as the main loss mechanisms of free charges.

4.3.4.1 Modified Drift-Diffusion Model

Drift-diffusion model is widely used for organic photovoltaics (OPV), and a key parameter θ, which can quantify the competition between charge extraction and recombination, is first introduced for organic solar cells.[163] In the literature, Bartesaghi *et al.* consider bimolecular recombination as the main loss mechanism of free charges. Instead, our model takes monomolecular and bimolecular recombination into account, and modifies the recombination-to-extraction ratio parameter θ.

First, on average, electrons (holes) have to travel half the active layer thickness (L) to reach the cathode (anode), and the extraction rate k_{ex} of electron and holes can be approximated as,

$$k_{ex} = \frac{2\mu_{n,p}V_{int}}{L^2} \tag{4.4}$$

where $\mu_{n,p}$ is the electron and hole mobility, respectively. V_{int} is the internal voltage, which is related to the LUMO and HOMO level of active materials, and $V_{int} \approx V_{oc} \approx 1$ eV is a good approximation for perovskite in our model. Note that k_{ex} has a unit of s^{-1}.

Second, the monomolecular recombination can be characterized by rate constant k_1, which also has a unit of s^{-1}.

Third, we use the approach reported by Bartesaghi *et al.* to describe the bimolecular recombination. The density of holes (electrons) is very small at the cathode (anode) and increases with increased distance from the cathode (anode). If holes (electrons) are generated at a volume rate G (10^{28} $m^{-3}s^{-1}$ for 1 sun) and flow towards the anode (cathode) at a speed $\mu_{n,p}V/L$, then the hole (electron) density close to the cathode (anode) is approximately:

$$p(x) = \frac{GLx}{\mu_{p,n}V_{int}} \tag{4.5}$$

The average density of holes (electrons) at the cathode (anode) side of the layer equals ($0 \leq x \leq L$)

$$p_{av} = \frac{GL^2}{\mu_{p,n}V_{int}} \tag{4.6}$$

Thus, the bimolecular recombination rate k_{rec} (s^-1) of electrons with holes near the cathode (anode) equals

$$k_{rec} = \gamma p_{av} = \frac{\gamma GL^2}{\mu_{p,n}V_{int}} \tag{4.7}$$

where γ is the strength of bimolecular recombination with a unit of $m^{-3}s^{-1}$. Considering monomolecular and bimolecular recombination of electrons and holes at both cathode and anode side, the modified recombination-to-extraction ratio parameter θ is defined as,

$$\theta = \frac{R_T}{k_{ex}} = \frac{k_1 + k_{rec}}{k_{ex}} = \left(\frac{1}{\mu_n} + \frac{1}{\mu_p}\right)\frac{k_1 L^2}{2V_{int}} + \frac{\gamma GL^4}{\mu_n \mu_p V_{int}^2} \tag{4.8}$$

Note that this characterizing factor θ presents a nonlinear relationship with the active layer thickness. Beyond an optimized thickness, the larger light harvesting

ability is counterbalanced by the stronger charge-carrier recombination effect, hence compromising the device performance. This can explain the previous observation that the fill factor begins to drop once the active layer thickness surpasses 65 nm, and the calculated J_{SC} of a 300-nm OPV device is larger than that of a 250-nm device, but the measured J_{SC} of 300-nm device is smaller.[146]

4.3.4.2 Simulation for Perovskite Solar Cells

Based on the transfer matrix simulation results for total absorbed photons in the active layer, assuming each absorbed photon generates an electron-hole pair, we exploit the modified drift-diffusion model for both 3D and 2D perovskite solar cells, and the ranges of parameters used are listed in Table 4.3. In particular, $\mu_{n,p}$, k_1 and γ are extrinsic parameters which have a much wider spectrum of values across the literature, in accordance with the vastly different measurement techniques and processing protocols that determine the microstructures of perovskite films.[135,142,164–174]

Table 4.3. Parameters used in the modified drift-diffusion simulations.

Symbol	Description	Values
L	Thickness	0−600nm for 3D perovskite 0−500nm for 2D perovskite
V_{int}	Internal voltage	1 V
$\mu_{n,p}$	Electron (hole) mobility	10^{-1}−10^{1} $cm^2V^{-1}s^{-1}$
G	Generation rate of free charges	10^{28} $m^{-3}s^{-1}$
k_1	Monomolecular recombination rate	10^{6}−10^{8} s^{-1}
γ	Strength of bimolecular recombination	10^{-10}−10^{-8} cm^3s^{-1}

- **Simulation for 3D Perovskite Solar Cells**

First, we perform calculations on the more extensively studied 3D perovskite system, using a photovoltaic structure comprised of ITO (150 nm)/PEDOT:PSS (45 nm)/$MAPbI_3$ (0−600 nm)/PCBM (20 nm)/Ag (140nm) as in the literature,[149] which

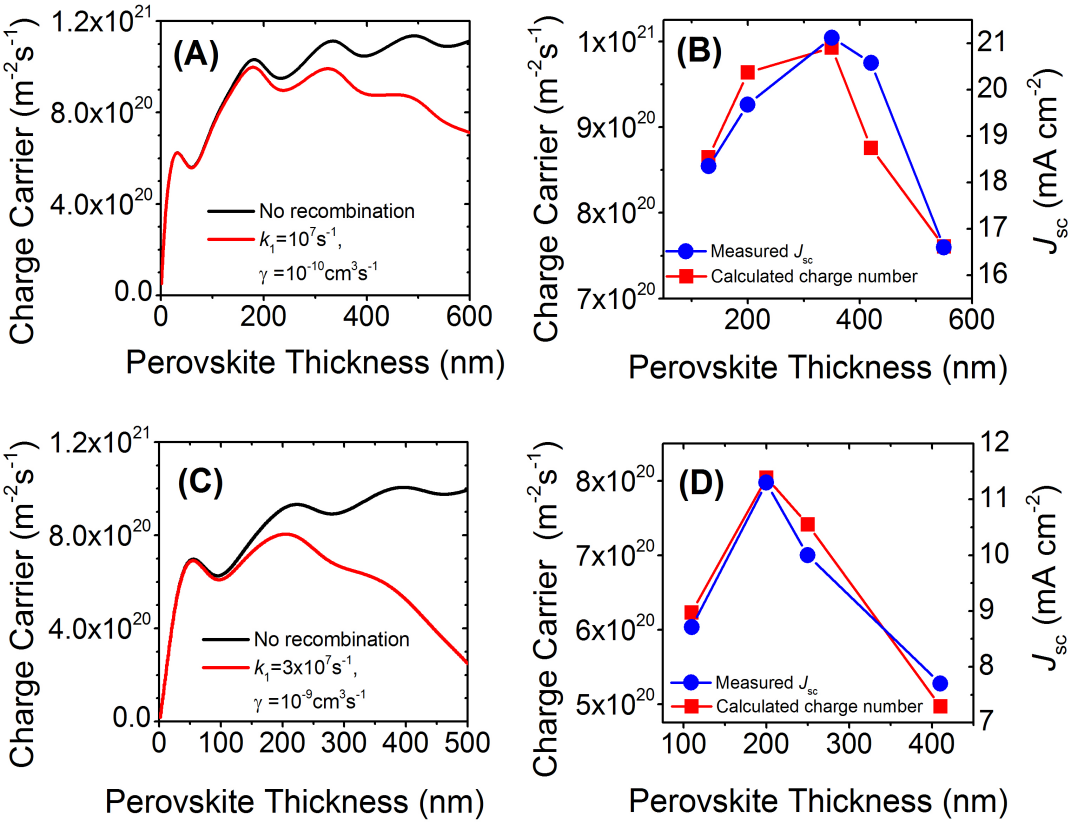

Figure 4.10. (**A**) Charge-carrier number calculated by modified drift-diffusion model for a photovoltaic structure consisting of ITO (150 nm)/PEDOT:PSS (45 nm)/$CH_3NH_3PbI_3$ (0 – 600 nm)/PCBM (20 nm)/Ag (140 nm). (**B**) Charge number in $CH_3NH_3PbI_3$-based device extracted from (**A**) for device comparing with measured J_{SC} from literature.[149] (**C**) Charge-carrier number calculated by modified drift-diffusion model for a photovoltaic structure consisting of ITO (150 nm)/PEDOT:PSS (40 nm)/2D Pb5 perovskite (0 – 500 nm)/PCBM (20 nm)/Al (150 nm). (**D**) Charge number in Pb5 device extracted from (**C**) comparing with measured J_{SC}.

has a structure similar to our 2D perovskite-based device described above. In the calculation, we use $k_1 = 10^7$ s^{-1} and $\gamma = 10^{-10}$ cm^{3}s^{-1} which have a typical order of magnitude for flat $MAPbI_3$ films reported by several research groups.[174] In Fig. 4.10(**A**), note that when the active layer is thicker than 150 nm, there is a drastic difference

in the extracted charge-carrier numbers before and after charge-recombination considerations. To investigate the accuracy of our calculation results from the model, we compare the measured charge-carrier populations extracted from Fig. 4.10(**A**) for solar cells comprised of $MAPbI_3$ layer with 130, 200, 350, 420, and 550 nm thickness with the corresponding measured J_{SC} values reported in literature.[149] As shown in Fig. 4.10(**B**), our calculations predict an optimal charge extraction for a 350-nm thick $MAPbI_3$ layer, beyond which the charge-carrier number decreases considerably due to significant charge recombination effects for the thicker device; this trend is in good agreement with that of the measured J_{SC}, confirming the effectiveness of our model. Interestingly, our model predicts another peak of the charge-carrier number for solar cell device with a perovskite layer around 180 nm, which may give rise to larger J_{SC} and higher PCE for this specific photovoltaic structure.

- **Fabrication, Characterization, and Simulation for 2D Pb5 Perovskite Solar Cells**

After verifying the validity of our drift-diffusion model using the extensively studied 3D perovskite, we next perform simulations for 2D Pb5-based photovoltaic structure (Fig. 4.7**A**), and obtain the active layer thickness-dependent charge-carrier number shown in Fig. 4.10(**C**). Since the experimental monomolecular and bimolecular recombination constants, k_1 and γ are unknown for Pb5 perovskite films, we need to select the constant values based on experimental device characteristics. Therefore, solar cells with hot-cast 2D Pb5 perovskite films of 110, 200, 250, and 410 nm thicknesses were fabricated and characterized. The measurement results are shown in Fig. 4.11 and Fig. 4.12, and summarized in Table 4.4. We find that the simulation

using $k_1 = 3 \times 10^7$ s^{-1} and $\gamma = 10^{-9}$ cm^{3}s^{-1} gives good agreement with the measurement results, and the calculated charge carrier number follows the same trend as the measured J_{SC} (Fig. 4.10**D**), where it first increases concomitantly with the active layer thickness from 110 to 200 nm, and then decreases significantly as the active layer gets thicker. Also, the optical modeling results, considering the charge recombination effect, match with the measured EQE for these specific thickness devices (Fig. 4.11**C**)

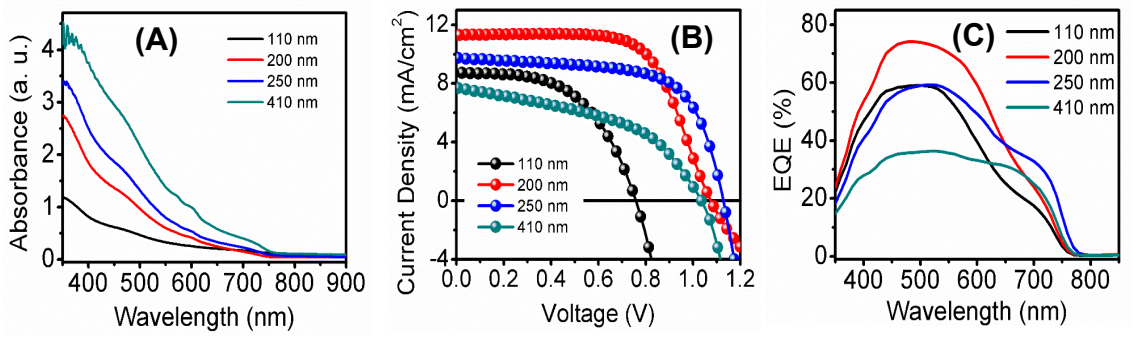

Figure 4.11. (**A**) UV-Vis absorption spectra of 2D Pb5 perovskite films with different thickness on glass. (**B**) $J-V$ curves of Pb5 perovskite-based devices. (**C**) EQE curves of Pb5 perovskite-based devices.

Table 4.4. Device parameters of optimized solar cells with different Pb5 perovskite film thicknesses along with calculated J_{SC} values. Average photovoltaic parameters and standard deviation for 10 devices are shown in parentheses.

Thickness (nm)	V_{OC} (V)	FF (%)	$J_{SC,cal}$ (mAcm^{-2})	$J_{SC,exp}$ (mAcm^{-2})	PCE (%)
110	0.759	54.2	9.98	8.71	3.58
	(0.738 ± 0.018)	(53.0 ± 1.1)		(8.33 ± 0.33)	(3.27 ± 0.28)
200	1.075	66.2	12.88	11.3	8.05
	(1.060 ± 0.011)	(68.1 ± 1.6)		(10.7 ± 0.40)	(7.71 ± 0.23)
250	1.143	61.0	11.88	10.0	6.98
	(1.131 ± 0.006)	(60.2 ± 1.6)		(9.54 ± 0.23)	(6.93 ± 0.14)
410	1.036	46.8	7.96	7.70	3.74
	(1.029 ± 0.01)	(46.4 ± 0.3)		(7.58 ± 0.06)	(3.62 ± 0.08)

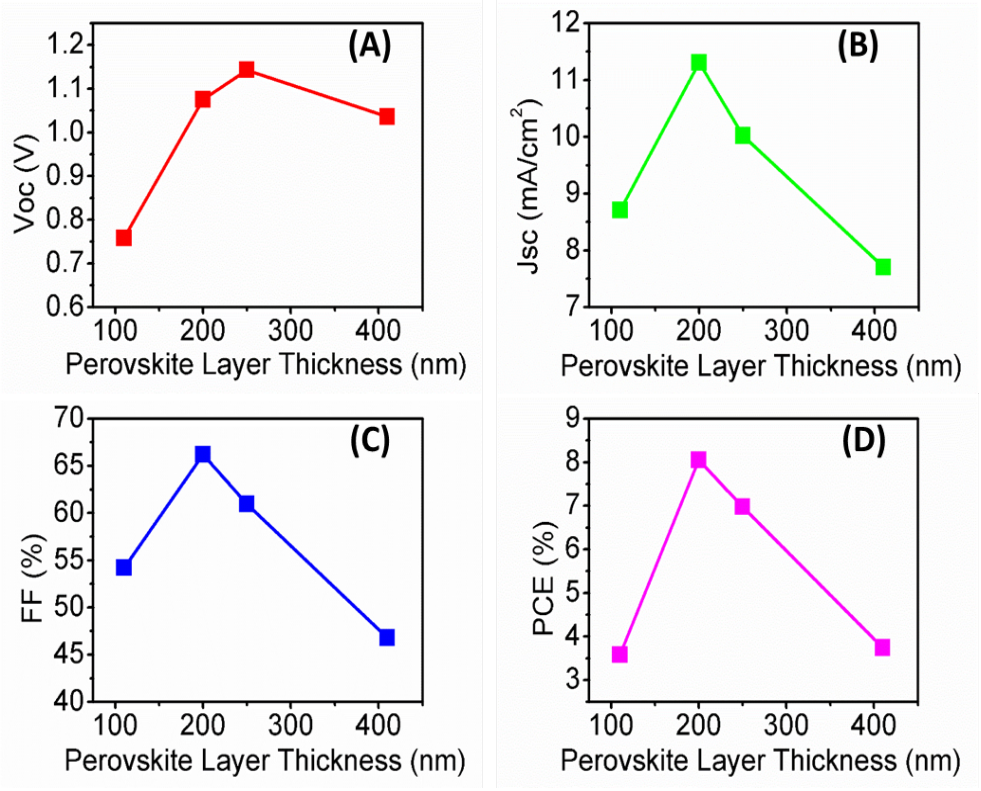

Figure 4.12. Device parameters of planar structure devices as a function of varying Pb5 active layer thicknesses: (**A**) open-circuit voltage (V_{OC}), (**B**) short-circuit current density J_{SC}, (**C**) fill factor (FF), and (**D**) power-conversion-efficiency (PCE).

Importantly, for simulations which can match the experimental data well, the monomolecular recombination constant k_1 used for Pb5 is slightly larger that of the 3D perovskite, and the bimolecular recombination constant γ is about one order of magnitude larger than that of the 3D counterpart. This observation is consistent with the experimental results reported by another study using 2D perovskites with a different type of organic spacer, $(PEA)_2(MA)_{m-1}Pb_mI_{3m+1}$, and PEA=$C_6H_5(CH_2)_2NH_3^+$, where the relatively larger k_1 and γ in the 2D perovskite films are attributed to an increase in exciton binding energy and electronic density of states near the band-edge as m decreases.[175] These changes are again a result of quantum confinement effects

and dielectric mismatch between the organic and inorganic components in the 2D layered perovskites. Moreover, the Pb5-based devices have a smaller measured fill factor ($< 70\%$ in Table 4.4), compared to the $MAPbI_3$-based devices with fill factors larger than 75% found in the literature,[149] suggesting that 2D Pb5 perovskite has a larger recombination rate and/or shorter diffusion length than the 3D counterpart. This likely arises from the polycrystalline nature of the present Pb5 films, inducing trap states between crystallites and hence a higher charge recombination.[176] Therefore, the selected values of k_1 and γ should be good estimates of the charge recombination constants of the 2D Pb5 perovskite films. Accordingly, the larger recombination constants of the 2D Pb5 perovskite, leading to a smaller J_{SC} and fill factor, may be the key limitation for achieving higher device efficiency compared to 3D perovskite solar cells. Note that the calculated J_{SC} extracted from the simulation results of charge carrier number is somewhat larger than the measured J_{SC} (Table 4.4), and we believe this can be attributed to the simplicity of our modified drift-diffusion model. In the model, we have assumed the charge-carrier mobility to be independent of the electric field and the charge density. Also, Auger recombination is not taken into account, which also plays an important role in the charge recombination, and can become dominant when the charge density is large. Overall, this simple model can describe recombination constants for different types of perovskite films, gives good estimations of the recombination constants, and can also be applied for thickness optimization in the solar cell device when the recombination parameters of specific active materials are well known.

4.4 Conclusion

In summary, spectroscopic ellipsometry and spectrophotometry can be used to investigate the optical properties of 2D $(BA)_2(MA)_{m-1}Pb_mI_{3m+1}$ (m = 2, 3, 4, and 5) perovskite thin films at room temperature, where the optical constants are found to depend on QW or perovskite slab thickness (m), and processing methods. The ellipsometric fitting results reveal that high-frequency dielectric constants increase with m for the members of the homologous series, which qualitatively agrees with the prediction of a simple QW model. Using optical constants of materials, optical transfer matrix formalism is used to investigate the absorption enhancement in 2D perovskite layers of planar-structure solar cells.

A modified drift-diffusion model is introduced to describe the charge recombination effects, which can predict the charge carrier number by combining the optical absorption profile obtained from transfer matrix calculations. This model is exploited for 3D $MAPbI_3$-based solar cells using typical measured values of charge recombination constants k_1 and γ, yielding good agreement between calculated charge number and measured J_{SC}. For 2D Pb5-based solar cells, our model gives good estimations for the charge recombination constants based on the device characterization measurement results, and we observe that the charge recombination constants of 2D Pb5 are larger than that of the 3D perovskite, which is the key limitation for achieving high efficiency of solar cells. This model can be applied for thickness optimization in solar cells via optical cavity-induced absorption enhancement in consideration of charge recombination, providing predictive metrics that can be used to guide device architecture design.

References

[133] A. Kojima, K. Teshima, Y. Shirai, and T. Miyasaka, "Organometal halide perovskites as visible-light sensitizers for photovoltaic cells," J. Am. Chem. Soc. **131**, 6050 (2009).

[134] H.-C. Liao, T. L. D. Tam, P. Guo, Y. Wu, E. F. Manley, W. Huang, N. Zhou, C. M. M. Soe, B. Wang, M. R. Wasielewski, L. X. Chen, M. G. Kanatzidis, A. Facchetti, R. P. H. Chang, and T. J. Marks, "Dopant-free hole transporting polymers for high efficiency, environmentally stable perovskite solar cells," Adv. Energy Mater. **6**, 1600502 (2016).

[135] H.-C. Liao, P. Guo, C.-P. Hsu, M. Lin, B. Wang, L. Zeng, W. Huang, C. M. M. Soe, W.-F. Su, M. J. Bedzyk, M. R. Wasielewski, A. Facchetti, R. P. H. Chang, M. G. Kanatzidis, and T. J. Marks, "Enhanced efficiency of hot-cast large-area planar perovskite solar cells/modules having controlled chloride incorporation," Adv. Energy Mater. **7**, 1601660 (2017).

[136] W. Nie, H. Tsai, R. Asadpour, J.-C. Blancon, A. J. Neukirch, G. Gupta, J. J. Crochet, M. Chhowalla, S. Tretiak, M. A. Alam, H.-L. Wang, and A. D. Mohite, "High-efficiency solution-processed perovskite solar cells with millimeter-scale grains," Science **347**, 522 (2015).

[137] Y. Han, S. Meyer, Y. Dkhissi, K. Weber, J. M. Pringle, U. Bach, L. Spiccia, and Y.-B. Cheng, "Degradation observations of encapsulated planar CH3NH3PbI3 perovskite solar cells at high temperatures and humidity," J. Mater. Chem. A Mater. Energy Sustain. **3**, 8139 (2015).

[138] D. H. Cao, C. C. Stoumpos, O. K. Farha, J. T. Hupp, and M. G. Kanatzidis, "2D homologous perovskites as light-absorbing materials for solar cell applications," J. Am. Chem. Soc. **137**, 7843 (2015).

[139] C. C. Stoumpos, D. H. Cao, D. J. Clark, J. Young, J. M. Rondinelli, J. I. Jang, J. T. Hupp, and M. G. Kanatzidis, "Ruddlesden-Popper hybrid lead Iodide perovskite 2D homologous semiconductors," Chem. Mater. **28**, 2852 (2016).

[140] C. C. Stoumpos, C. M. M. Soe, H. Tsai, W. Nie, J. Blancon, D. H. Cao, F. Liu, B. Traore, C. Katan, J. Even, A. D. Mohite, and M. G. Kanatzidis, "High members of the 2D Ruddlesden-Popper halide perovskites: synthesis, optical properties, and solar cells of $(CH_3(CH_2)_3NH_3)_2(CH_3NH_3)_4Pb_5I_{16}$," Chem. **2**, 427 (2017).

[141] J.-C. Blancon, H. Tsai, W. Nie, C. C. Stoumpos, L. Pedesseau, C. Katan, M. Kepenekian, C. M. M. Soe, K. Appavoo, M. Y. Sfeir, S. Tretiak, P. M. Ajayan, M. G. Kanatzidis, J. Even, J. J. Crochet, and A. D. Mohite, "Extremely efficient internal exciton dissociation through edge states in layered 2D perovskites," Science **6331**, 1228 (2017).

[142] H. Tsai, W. Nie, Jean-Christophe Blancon, C. C. Stoumpos, R. Asadpour, B. Harutyunyan, A. J. Neukirch, R. Verduzco, J. J. Crochet, S. Tretiak, L. Pedesseau, J. Even, M. A. Alam, G. Gupta, J. Lou, P. M. Ajayan, M. J. Bedzyk, M. G. Kanatzidis, and A. D. Mohite, "High-efficiency two-dimensional Ruddlesden-Popper perovskite solar cells," Nature **536**, 312 (2016).

[143] L. A. A. Pettersson, L. S. Roman, and O. Inganas, "Modeling photocurrent action spectra of photovoltaic devices based on organic thin films," J. Appl. Phys. **86**, 487 (1999).

[144] D. W. Sievers, V. Shrotriya, and Y. Yang, "Modeling optical effects and thickness dependent current in polymer bulk-heterojunction solar cells," J. Appl. Phys. **100**, 114509 (2006).

[145] B. Valle, S. Loser, J. W. Hennek, V. DeGeorge, C. Klosterman, J. H. Andrews, and K. D. Singer, "Spectral aspects of cavity tuned absorption in organic photovoltaic films," Opt. Express **20**, A954 (2012).

[146] S. Loser, B. Valle, K. A. Luck, C. K. Song, G. Ogien, M. C. Hersam, K. D. Singer, and T. J. Marks, "High-efficiency inverted polymer photovoltaics via spectrally tuned absorption enhancement," Adv. Energy Mater. **4**, 1301938 (2014).

[147] C. W. Chen, S.Y. Hsiao, C. Y. Chen, H. W. Kang, Z. Y. Huang, and H. W. Lin, "Optical properties of organometal halide perovskite thin films and general device structure design rules for perovskite single and tandem solar cells," J. Mater. Chem. A **3**, 9152 (2015).

[148] J. M. Ball, S. D. Stranks, M. T. Horantner, S. Huttner, W Zhang, E. J. W. Crossland, I. Ramirez, M. Riede, M. B. Johnston, R. H. Friend, and H. J. Snaith, "Optical properties and limiting photocurrent of thin-film perovskite solar cells," Energy Environ. Sci. **8**, 602 (2015).

[149] B. Xia, Z. Wu, H. Dong, J. Xi, W. Wu, T. Lei, K. Xi, F. Yuan, B. Jiao, L. Xiao, Q. Gong, and X. Hou, "Formation of ultrasmooth perovskite films toward highly efficient inverted planar heterojunction solar cells by micro-flowing anti-solvent deposition in air," J. Mater. Chem. A **4**, 6295 (2016).

[150] P. Löper, M. Stuckelberger, B. Niesen, J. Werner, M. Filipič, S. J. Moon, J. H. Yum, M. Topič, S. De Wolf, and C. Ballif, "Complex refractive index spectra of $CH_3NH_3PbI_3$ perovskite thin films determined by spectroscopic ellipsometry and spectrophotometry," J. Phys. Chem. Lett. **6**, 66 (2015).

[151] A. Forouhi and I. Bloomer, "Optical dispersion relations for amorphous semiconductors and amorphous dielectrics," Phys. Rev. B **34**, 7018 (1986).

[152] M. S. Alias, I. Dursun, M. I. Saidaminov, E. M. Diallo, P. Mishra, T. K. Ng, O. M. Bakr, and B. S. Ooi, "Optical constants of $CH_3NH_3PbBr_3$ perovskite thin films measured by spectroscopic ellipsometry," Opt. Express **24**, 16586 (2016).

[153] A. M. A. Leguy, P. Azarhoosh, M. I. Alonso, M. Campoy-Quiles, O. J. Weber, J. Yao, D. Bryant, M. T. Weller, J. Nelson, A. Walsh, M. van Schilfgaarde, and P. R. F. Barnes, "Experimental and theoretical optical properties of methylammonium lead halide perovskites," NanoscaleB **8**, 6317 (2016).

[154] H. Fujiwara, "Spectroscopic Ellipsometry: Principles and Applications," John Wiley & Sons: Chichester, UK (2007).

[155] T. Ishihara, J. Takahashi, and T. Goto, "Optical properties due to electronic transitions in two-dimensional semiconductors $(C_nH_{2n+1}NH_3)_2PbI_4$," Phys. Rev. B **42**, 11099 (1990).

[156] M. Hirasawa, T. Ishihara, T. Goto, K. Uchida, and N. Miura, "Magnetoabsorption of the lowest exciton in perovskite-type compound $(CH_3NH_3)PbI_3$," Physica B **201**, 427 (1994).

[157] M. Hirasawa, T. Ishihara, and T. Goto, "Exciton features in 0-, 2-, and 3-dimensional networks of $[PbI_6]^{4-}$," J. Phys. Soc. Jpn. **63**, 3870 (1994).

[158] X. Hong, T. Ishihara, and A. V. Nurmikko, "Photoconductivity and electroluminescence in lead iodide based natural quantum well structures," Solid State Commun. **84**, 657 (1992).

[159] X. Hong, T. Ishihara, and A. V. Nurmikko, "Dielectric confinement effect on excitons in PbI_4-based layered semiconductors," Phys. Rev B **45**, 6961 (1992).

[160] K. Tanaka and T. Kondo, "Bandgap and exciton binding energies in lead-iodide-based natural quantum-well crystals," Sci. Technol. Adv. Mater. **4**, 599 (2003).

[161] T. M. Koh, V. Shanmugam, J. Schlipf, L. Oesinghaus, P. Müller-Buschbaum, N. Ramakrishnan, V. Swamy, N. Mathews, P. P. Boix, and S. G. Mhaisalkar, "Nanostructuring mixed-dimensional perovskites: A route toward tunable, efficient photovoltaics," Adv. Mater. **28**, 3635 (2016).

[162] G. Lakhwani, A. Rao, and R. H. Friend, "Bimolecular recombination in organic photovoltaics," Annu. Rev. Phys. Chem. **65**, 557 (2014).

[163] D. Bartesaghi, I. del C. Perez, J. Kniepert, S. Roland, M. Turbiez, D. Neher, and L. J. A. Koster, "Competition between recombination and extraction of free charges determines the fill factor of organic solar cells," Nat. Commun. **6**, 7083 (2015).

[164] S. D. Stranks, G. E. Eperon, G. Grancini, C. Menelaou, M. J. P. Alcocer, T. Leijtens, L. M. Herz, A. Petrozza, and H. J. Snaith, "Electron-hole diffusion lengths exceeding 1 micrometer in an organometal trihalide perovskite absorber," Science **342**, 341 (2013).

[165] D. Wang, M. Wright, N. K. Elumalai, and A. Uddin, "Stability of perovskite solar cells," Sol. Energy Mater. Sol. Cells **147**, 255 (2016).

[166] D. W. Dane, S. M. Vorpahl, S. D. Stranks, H. Nagaoka, G. E. Eperon, M. E. Ziffer, H. J. Snaith, and D. S. Ginger, "Impact of microstructure on local carrier lifetime in perovskite solar cells," Science **348**, 683 (2015).

[167] Y. Yamada, T. Nakamura, M. Endo, A. Wakamiya, and Y. Kanemitsu, "Photocarrier recombination dynamics in perovskite $CH_3NH_3PbI_3$ for solar cell applications," J. Am. Chem. Soc. **136**, 11610 (2014).

[168] M. Saba, M. Cadelano, D. Marongiu, F. Chen, V. Sarritzu, N. Sestu, C. Figus, M. Aresti, R. Piras, A. Geddo Lehmann, C. Cannas, A. Musinu, F. Quochi, A. Mura, and G. Bongiovanni, "Correlated electron-hole plasma in organometal perovskites," Nat. Commun. **5**, 5049 (2014).

[169] V. D'Innocenzo, A. R. S. Kandada, M. De Bastiani, M. Gandini, and A. Petrozza, "Tuning the light emission properties by band gap engineering in hybrid lead halide perovskite," J. Am. Chem. Soc. **136**, 17730 (2014).

[170] M. T. Trinh, X. Wu, D. Niesner, and X. Y. Zhu, "Many-body interactions in photo-excited lead iodide perovskite," J. Mater. Chem. A **3**, 9285 (2015).

[171] T. J. Savenije, C. S. Ponseca, L. Kunneman, M. Abdellah, K. Zheng, Y. Tian, Q. Zhu, S. E. Canton, I. G. Scheblykin, T. Pullerits, A. Yartsev, and V. Sundström, "Thermally activated exciton dissociation and recombination control the carrier dynamics in organometal halide perovskite," J. Phys. Chem. Lett. **5**, 2189 (2014).

[172] R. L. Milot, G. E. Eperon, H. J. Snaith, M. B. Johnston, and L. M. Herz, "Temperature-dependent charge-carrier dynamics in $CH_3NH_3PbI_3$ perovskite thin films," Adv. Funct. Mater. **25**, 6218 (2015).

[173] L. M. Herz, "Charge-carrier dynamics in organic-inorganic metal halide perovskite," Rev. Phys. Chem. Mater. **67**, 65 (2016).

[174] M. B. Johnston and L. M. Herz, "Hybrid perovskites for photovoltaics: charge-carrier recombination, diffusion, and radiative efficiencies," Acc. Chem. Res. **49**, 146 (2016).

[175] R. L. Milot, R. J. Sutton, G. E. Eperon, A. A. Haghighirad, J. M. Hardigree, L. Miranda, H. J. Snaith, M. B. Johnston, and L. M. Herz, "Charge-carrier dynamics in 2D hybrid metal-halide perovskites," Nano Lett. **16**, 7001 (2016).

[176] B. Wang, K. Y. Wong, S. Yang, and T. Chen, "Crystallinity and defect state engineering in organo-lead halide perovskite for high-efficiency solar cells," J. Mater. Chem. A **4**, 3806 (2016).

5 Nonlinear Optical Properties of Coextruded Multilayered Polymer Films

5.1 Introduction

Organic second-order nonlinear optical (NLO) materials are being actively pursued due to their potential for application in photonic devices, such as high-speed electro-optic (EO) modulators, optical switches, and frequency converters. Compared with inorganic materials, like $LiNbO_3$ currently used in commercial modulators, organic NLO materials can give a significantly higher EO response. The availability of large EO coefficients enables not only unprecedented performance in conventional device formats, but also the possibility of new devices such as hybrid modulators and integrating EO polymers with silicon photonics.[177]

To give rise to a strong bulk second-order NLO response, first, according to the relationship between microscopic and macroscopic nonlinearities, it is required that the active component has a large molecular first hyperpolarizability coefficient β_{ijk}.[178] For this purpose, most of the effective NLO chromophores have been synthesized using a similar principle: planar conjugated p-electron systems end capped with electron-donor and -acceptor (D, A) moieties. This design algorithm gives rise to a dominant

intramolecular charge-transfer (ICT) transition from the ground state to the first excited state and induces a polarization along the π-conjugated axis.[179]

Moreover, structural features, such as ordering and orientation of molecules, can also influence bulk second-order NLO performance.[180] Several approaches have been reported for organizing NLO chromophores into materials with high, stable second-order NLO response. In polymeric structures, strategies to optimize the chromophore alignment usually include: 1) external electric-field poling, 2) Langmuir-Blodgett film transfer and crystal growth. However, these polymeric systems have significant limitations, which include limited thermal stability and tendency for randomization of chromophore alignment with time.[181]

Here we propose a completely new alignment strategy for NLO chromophores, producing thin films with hundreds or thousands of alternating layers of three polymers having net polarity by using melt-processed layer-multiplying co-extrusion technique.[182–184] The amphiphilic NLO chromophore used has two ends, where one is polar and should be soluble in hydrophilic polymers, while the other one is lipophilic and should be soluble in hydrophobic polymers. Thus, these NLO molecules would be included during the coextrusion and self-align themselves at the desired interface of the multilayers, composing polymers with differing hydrophobic nature that will provide the means of orienting the chromophore at the interface. Due to the centrosymmetry broken by the ordered orientation of NLO chromophores, the coextruded multilayer films could give rise to large second-order nonlinear optical response.

5.2 Experimental

5.2.1 Materials and Processing

The $(ABC)_n$ multilayer films were coextruded at 250 °C using a continuous layer-multiplying process (Fig. 5.1(a)), and consisted of 768 alternating layers of doped poly(styrene-co-acrylonitrile) with 25 wt% acrylonitrile (SAN25), Ethylene vinyl alcohol (EVOH) with 24 wt% ethylene content, and polyvinylidene fluoride (PVDF). Low-density polyethylene (PE) skin layers were added to both sides of the multilayer films.

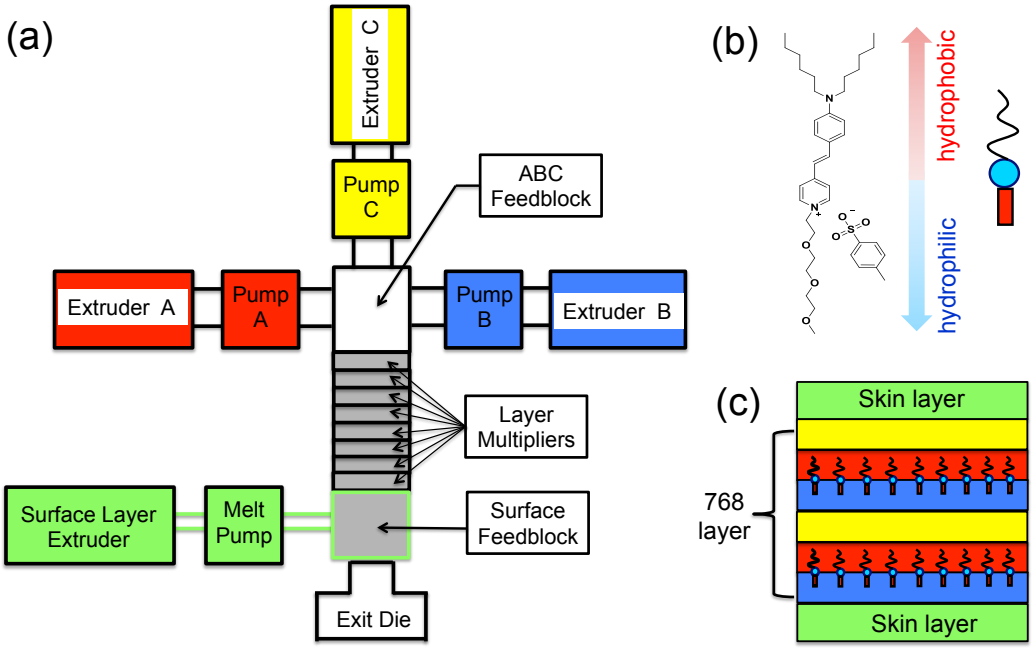

Figure 5.1. (a) Schematic of the multilayer coextrusion process. (b) Chemical structure of the NLO chromophore. (c) Coextruded multilayered architecture.

The chemical structure of the nonlinear optical chromophore employed shows two ends (Fig. 5.1(b)), and one is polar and should be soluble in hydrophilic polymers, EVOH used for the multilayer system; while the other one is lipophilic and should

be soluble in hydrophobic polymers, SAN25. Before coextrusion process, the NLO molecules are doped into SAN25 with a concentration of 3 wt%. An $(AB)_n$ multilayer structure is not used, because the chromophore will orient along opposite directions at two interfaces, the centrosymmetry of the system is not broken, and there will be no second-order nonlinear optical response. Therefore, a third layer is required, as shown in Fig. 5.1(c), PVDF is used as a barrier layer, and NLO molecules align along the same direction at the interface between SAN25 and EVOH within the $(ABC)_n$ multilayer system.

For comparison of NLO response, some dye-doped-polymer thin films were prepared by spin-coating.

5.2.2 Second-Harmonic Generation Technique

To characterize the second-order nonlinear optical response of the coextruded $(ABC)_n$ multilayer system, angle-resolved second-harmonic generation (SHG) is measured, and the setup is shown in Fig. 5.2. Infrared wavelengths used as the fundamental pump are generated from a optical parametric oscillator (GWU premiScan/BB), which is pumped by 355-nm Nd:YAG Q-switch pulsed laser (Spectra-Physics Quanta-Ray LAB-170-10) with 10 Hz reparation rate, 10-ns pulse duration and 180 mJ pulse energy. The combination of a polarizing prism and compensator is used to determine the polarization of the fundamental beam and continuously vary the pump power. Using a beam splitter, the fundamental beam is divided into two, one goes to a reference arm, where a potassium dihydrogen phosphate (KDP) plate is used as the reference; while the other goes to the sample arm, where the sample is placed on the computer-controlled motorized rotary stage. The signal from the sample is compared

to the signal from the reference to avoid errors due to pump beam intensity fluctuations. The KG3 (Schott) color filter, narrow band-pass filter (Thorlabs, Inc.) and neutral density filter are used to attenuate the fundamental beam and to verify the detected wavelength is from SHG. The data is acquired from a photomultiplier tube (PMT, Hamamatsu) in combination with a gated BoxCar integrator (SR200 series, Stanford Research Systems).

To obtain the second-harmonic generation coefficients of the thin films investigated, the SHG from a Y-cut quartz is also measured on the rotary stage in the sample arm, as its SHG coefficient is one known constant, and the ratio of peak SHG intensity of the extruded film to that of quartz will give the effective SHG coefficient of the film studied.

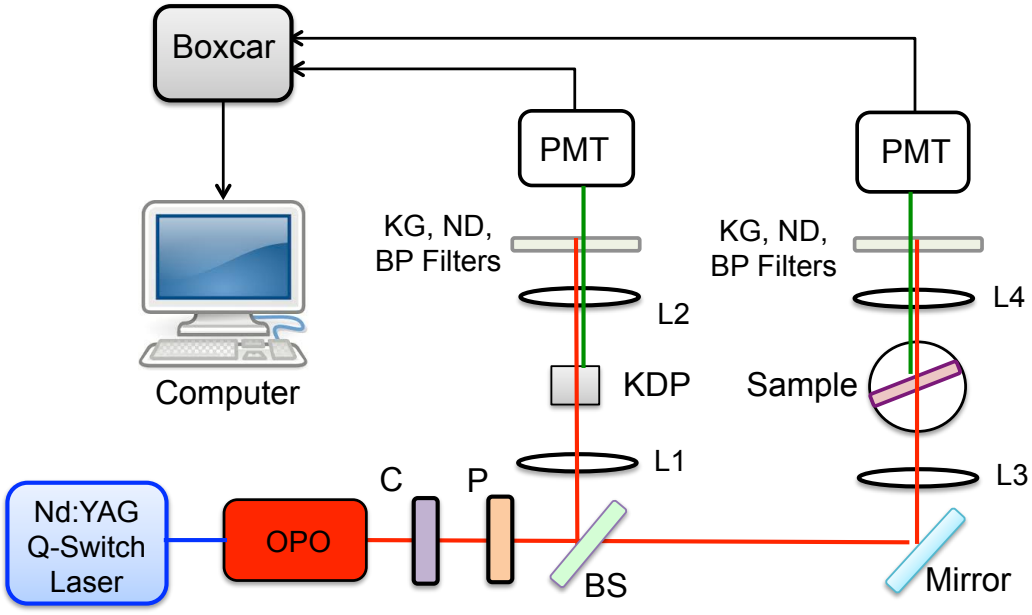

Figure 5.2. Schematic setup of angle-resolved SHG experiment. C: compensator; P: polarizing prism; BS: beam splitter; L1-L4: lens; ND: neutral density filter; BP: narrow band-pass filter; PMT: photomultiplier tube.

5.3 Results and Discussion

Fig. 5.3(a) shows the Atomic force microscopy (AFM) image of the cross-section of a typical extruded film, and individual layers of materials can be roughly resolved by different colors in the image, which demonstrates the formation of multilayer structure. The inset of Fig. 5.3(a) shows a picture of the surface of the film, and the thickness varies between 30 and 50 μm in different areas, leading to the streak in the film. The absorption spectra of a 2 μm-thick spin-coated SAN25/chromophore film and 30 μm-thick extruded film are shown in Fig. 5.3(b), which exhibit similar trend.

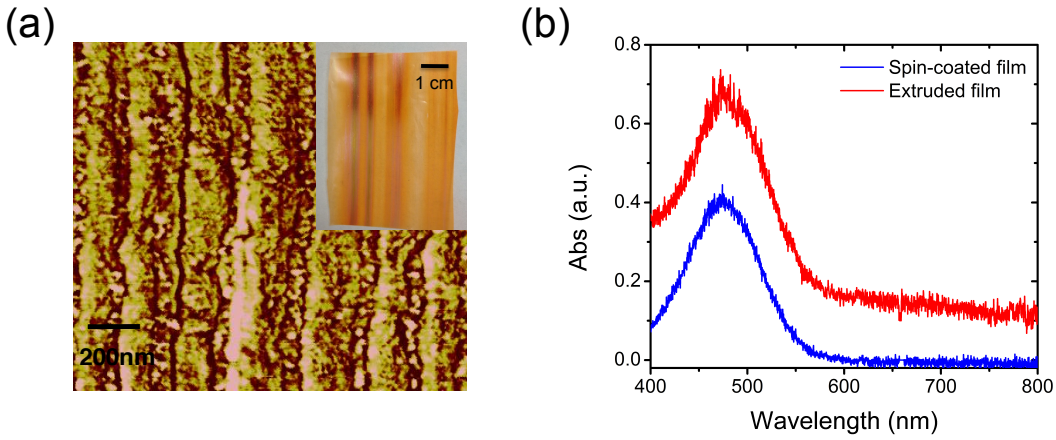

Figure 5.3. (a) AFM image of the cross-section of an extruded film. The inset is a photo of the surface of an extruded film. (b) Absorption spectra of a 2 μm-thick spin-coated SAN25/chromophore film and 30 μm-thick extruded film.

5.3.1 Nonlinear Optical Characterization by SHG

Fig. 5.4(a) shows Angle-resolved transmitted SHG intensity of a 30 μm-thick extruded film pumped by TM-polarized 1064 nm and 1300 nm, respectively, which behave typically for thin films when the coherence length is large compared to the film thickness.[185] Thus, the value of the effective SHG coefficients of the extruded

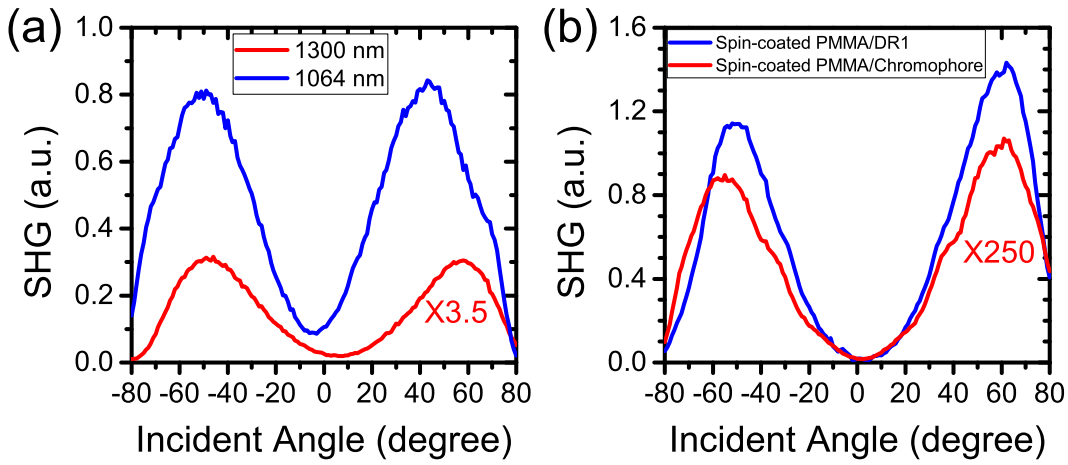

Figure 5.4. (a) Angle-resolved transmitted SHG intensity of a 30 μm-thick extruded film pumped by two different TM-polarized wavelengths. (b) Angle-resolved transmitted SHG intensity of two spin-coated films doped with different dye molecules.

film can be determined by comparison to the coefficient of quartz measured under the same conditions: $d_{eff} = 2 \times 10^{-10}$ esu at $\lambda = 1064$ nm, and $d_{eff} = 1.2 \times 10^{-10}$ esu at $\lambda = 1300$ nm, respectively.

However, compared to quartz, the extruded film gives rise to much lower SHG signal, and the effective SHG coefficients are one order of magnitude smaller than that of quartz. To understand the observation, we have tried to obtain the molecular first hyperpolarizability coefficient of the chromophore. For comparison, a well-studied nonlinear organic molecule, Disperse Red 1 (DR1), is also considered. Monolayer PMMA/DR1 and PMMA/Chromophore thin films are prepared by spin-coating, which are coated on ITO glass. To break the centrosymmetry and orient molecules with certain order, the corona poling technique is employed. Basically, the corona discharge, which is a partial breakdown of air at atmospheric pressure, is used to pole the polymer guest-host system after raising the temperature close to the glass-rubber transition temperature. Then, cool the system quickly during poling, and the guest

molecules are frozen into their new ordered orientation.[186,187] The SHG intensity of both poled films are measured using a TM-polarized fundamental wavelength of 1300 nm, which are shown in Fig. 5.4(b). The value of the second harmonic coefficient d_{33} for these poled films, which possess a unique axis in the direction parallel to the field direction within the point group ∞mm, thus can be determined by comparison to d_{11} of quartz measured under the same conditions:[185] $d_{33} = 2.0 \times 10^{-9}$ esu for PMMA/DR1 film, and $d_{33} = 3.8 \times 10^{-11}$ esu for PMMA/chromophore film, respectively.

Moreover, the magnitude of the nonlinear optical coefficients can be estimated from thermodynamic considerations that include the effect of local fields. The bulk polarization at optical frequency 2ω in the presence of incident electromagnetic fields at frequency ω can be derived by considering the molecular polarization and taking the thermodynamic average of the molecular ensemble under the assumptions that, at the poling conditions, the molecules rotate without interaction and that the molecule is axial and planar.[180] Thus, the SHG coefficient d_{33} and the molecular first hyperpolarizability have the following relation:[185]

$$d_{33}\left(2\omega;\omega,\omega\right) = N f^{2\omega} f^{\omega} f^{\omega} \beta_{zzz}\left(2\omega;\omega,\omega\right) L_3\left(p\right), \tag{5.1}$$

where N is the number density of nonlinear optical molecules, L_3 is the third order Langevin function, which, assuming that molecular polarization anisotropy is small, is given by

$$L_3\left(p\right) = \frac{p}{5} - \frac{p^3}{105} + \cdots, \tag{5.2}$$

where

$$p = \left(\frac{\epsilon\left(n^2+2\right)}{n^2+2\epsilon}\right)\frac{\mu E_p}{kT}, \tag{5.3}$$

where ϵ is the static dielectric constant, n the index of refraction, and E_p the poling field. The z direction is the direction of the ground state dipole moment, and β_{zzz} is the dominant molecular nonlinear optical susceptibility component. Appropriate local field factors for the optical field, f^{ω}, are Lorentz type, $\left(n_{\omega}^2+2\right)/3$, and for the poling field in Eq. 5.3, are Onsager type.[188]

Table 5.1. Properties of two types of dye-doped PMMA films. N is the number density of molecules in PMMA, E_p the magnitude of the poling field, d_{33} the SHG coefficients, and $\beta\mu$ the calculated results.

Spin-coated film	Thickness (μm)	E_p (MV/cm)	N (10^{19}/cm^3)	d_{33} (10^{-10} esu)	$\beta\mu$ (cm^{5}D/esu)
PMMA/DR1	1.2	3.3	7.0	20	525×10^{-30}
PMMA/chro.	1.5	2.3	3.3	0.38	30.4×10^{-30}

According to above discussion, using the leading term of the Langevin function, we have that

$$d_{33} \propto N \times E_p \times (\beta\mu) \tag{5.4}$$

Finally, using the parameter values of N, E_p and d_{33} listed in Table 5.1, we can obtain that:

$$\frac{(\beta\mu)_{chro.}}{(\beta\mu)_{DR1}} = \frac{(d_{33})_{chro.}}{(d_{33})_{DR1}} \times \frac{N_{DR1}}{N_{chro.}} \times \frac{(E_p)_{DR1}}{(E_p)_{chro.}} = 5.78 \times 10^{-2} \tag{5.5}$$

As given in the literature, the value of $(\beta\mu)$ of DR1 is 525×10^{-30} cm^{5}D/esu,[185] thus $(\beta\mu)$ of the chromophore studied is 30.4×10^{-30} cm^{5}D/esu.

According to the above discussion, we can conclude that the product $(\beta\mu)$ of the chromophore used for the extruded multilayer film is much smaller than the value of DR1, leading to smaller SHG coefficient d_{33}, and this may explain why the extruded film could not give rise to strong SHG signal.

Another possible reason for small SHG intensity from the extruded film is that multilayer structure is not well established, which can inhibit the orientation of the molecues. In order to orient the amphiphilic chromophore, hydrophobic polymer (SAN25) and hydrophilic polymer (EVOH) are used, however, the large contrast of hydrophobicity between two different polymers can extremely increase difficulties in making high-quality multilayer structure with favorable interfaces during coextrusion process.

5.4 Conclusion

In summary, we have demonstrated a new alignment strategy for nonlinear optical chromophore, producing thin films with hundreds of alternating layers of three polymers, and the amphiphilic chromophore can self-align at the interface of two polymers during the coextrusion process. The multilayer film gives relatively lower second-harmonic intensity, comparing with typical nonlinear inorganic and organic materials, such as quartz and Disperse Red 1, which contributes to the small molecular hyperpolarizability and unideal formation of multilayer structure. To resolve the problem, there are two requirements, first, using amphiphilic NLO chromophores with large molecular hyperpolarizability should be a prerequisite; second, to further improve the quality of the coextruded-multilayered film, deliberate selections of polymers are required, including the hydrophobic and hydrophilic polymers, which provide the interface to align chromophores, and the third barrier layer of polymer.

References

[177] X.-H. Zhou, J. Luo, S. Huang, T.-D. Kim, Z. Shi, Y.-J. Cheng, S.-H. Jang, D. B. Knorr Jr., R. M. Overney, and A. K.-Y. Jen, "Supramolecular self-assembled dendritic nonlinear optical chromophores: Fine-tuning of arene-perfluoroarene interactions for ultralarge electro-optic activity and enhanced thermal stability," Adv. Mater. **21**, 1976 (2009).

[178] J. Zyss and J. L. Oudar, "Relations between microscopic and macroscopic lowest-order optical nonlinearities of molecular crystals with one- or two-dimensional units," Phys. Rev. A **26**, 2028 (1982).

[179] Y.-J. Cheng, J. Luo, S. Hau, D. H. Bale, T.-D. Kim, Z. Shi, D. B. Lao, N. M. Tucker, Y. Tian, L. R. Dalton, P. J. Reid, and A. K-Y. Jen, "Large electro-optic activity and enhanced thermal stability from diarylaminophenyl-containing high-β nonlinear optical chromophores," Chem. Mater. **19**, 1154 (2007).

[180] K. D. Singer, M. G. Kuzyk, and J. E. Sohn, "Second-order nonlinear-optical processes in orientationally ordered materials: relationship between molecular and macroscopic properties," J. Opt. Soc. Am. B **4**, 968 (1987).

[181] K. D. Singer and L. A. King, "Relaxation phenomena in polymer nonlinear optical materials," J. Appl. Phys. **70**, 3251 (1991).

[182] T. Kazmierczak, H. Song, A. Hiltner, and E. Baer, "Polymeric one-dimensional photonic crystals by continuous coextrusion," Macromol. Rapid Commun. **28**, 2210 (2007).

[183] H. Wang, J. K. Keum, A. Hiltner, E. Baer, B. Freeman, A. Rozanski, and A. Galeski, "Confined crystallization of polyethylene oxide in nanolayer assemblies," Science **323**, 757 (2009).

[184] M. Mackey, A. Hiltner, E. Baer, L. Flandin, M. A. Wolak, and J. S. Shirk, "Enhanced breakdown strength of multilayered films fabricated by forced assembly microlayer coextrusion," J. Phys. D: Appl. Phys. **42**, 175304 (2009).

[185] K. D. Singer, J. E. Sohn, and S. J. Lalama, "Second harmonic generation in poled polymer films," Appl. Phys. Lett. **49**, 248 (1986).

[186] K. D. Singer, M. G. Kuzyk, W. R. Holland, J. E. Sohn, S. J. Lalama, R. B. Comizzoli, H. E. Katz, and M. L. Schilling, "Electro-optic phase modulation and optical second-harmonic generation in corona-poled polymer films," Appl. Phys. Lett. **53**, 1800 (1988).

[187] M. A. Mortazavi, A. Knoesen, S. T. Kowel, B. G. Higgins, and A. Dienes, "Second-harmonic generation and absorption studies of polymer-dye films oriented by corona-onset poling at elevated temperatures," J. Opt. Soc. Am. B **6**, 733 (1989).

[188] K. D. Singer and A. F. Garito, "Measurements of molecular second order optical susceptibilities using dc induced second harmonic generation," J. Chem. Phys. **75**, 3572 (1981).

6 Future Work

6.1 Organic Cavity Polaritons

6.1.1 Cavity-Polariton-Induced Conductivity Enhancement

Organic cavity polariton, as a hybrid light-matter state, is of importance for potential applications. Due to the characteristic delocalization of the wavefunctions of the hybridized states, it is expected that the strongly coupled coherent collective states can extend over a large number of organic molecules and should thereby favor conductivity. Theoretical work predicts that exciton conductance in organic materials can be enhanced by several orders of magnitude when the molecules are strongly coupled to an electromagnetic mode, resulting from the formation of a collective polaritonic mode which allows excitons to bypass the disordered array of molecules and jump directly from one end of the structure to the other.[189,190] Recently, Ebbesen *et al.* demonstrated that the conductivity of organic semiconductors was enhanced when the exciton of molecues was strongly coupled to surface plasmon modes of the metallic hexagonal arrays, to form hybrid coherent states.[191] To the best of our knowledge, cavity-polariton-induced conductivity enhancement has not been experimentally demonstrated yet. The challenge for particular metallic Fabry-Pérot cavities is how to ensure there is no direct contact between top and bottom metallic mirror

and no leakage via the top mirror when measuring the current parallel to the cavity,[191] as the organic cavity layer usually has a thickness of less than 200 nm.

To investigate cavity-polariton enhanced conductivity, the organic cavities should first have superb quality without pinholes. In the following, I will introduce the modified method for preparing organic cavities, which can improve the cavity quality.

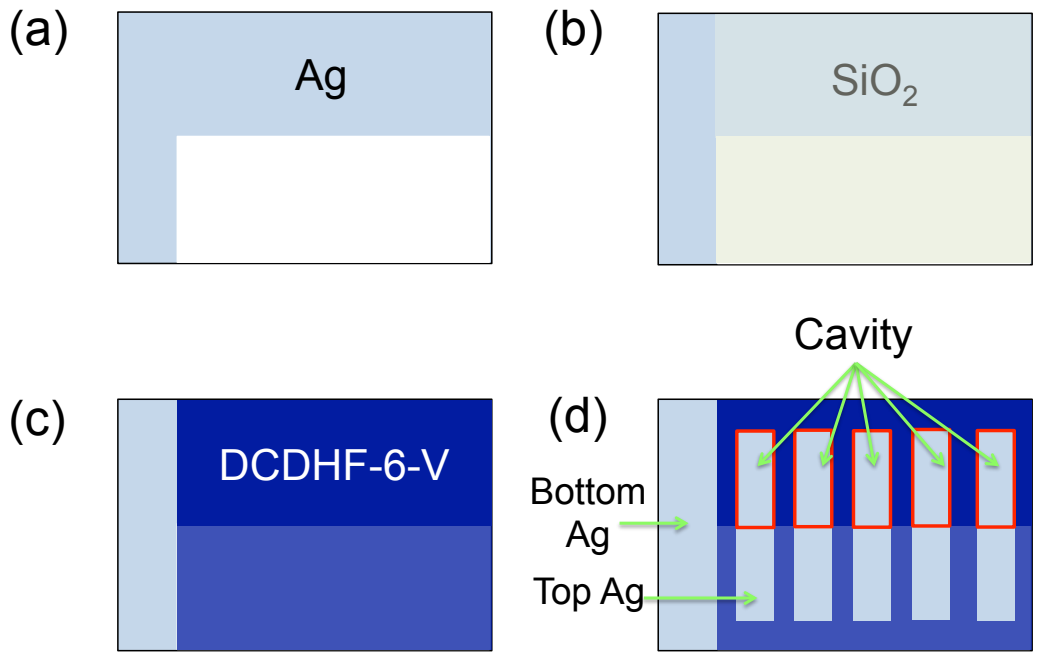

Figure 6.1. Steps for organic-cavity fabrication.

(1) A 30 nm-thck L-shape silver film is thermally evaporated onto the clean glass substrate in vacuum, see Fig. 6.1(a);

(2) As shown in Fig. 6.1(b), a very thin barrier layer (< 10 nm) of SiO_2 can be coated on top of the silver layer by electron-beam physical vapor deposition;

(3) DCDHF-6-V is then spun cast on top of the barrier layer, see Fig. 6.1(c);

(4) Using a specific shadow mask, a second 30 nm-thck silver layer is thermally evaporated onto the masked substrate, and several cavities will be made on a single glass substrate, which are illustrated in Fig. 6.1(d).

The above fabrication method has two key features, which can lead to good-quality cavities: (1) the barrier layer can effectively avoid direct contact between two silver layers; (2) several cavities are prepared on a substrate by using a shadow mask, some of which may have no pinholes due to the small cavity area (~ 0.1 cm^2).

Moreover, for comparison, some half-cavities can be prepared using L-shape indium tin oxide (ITO) coated glass to replace the bottom silver layer, and I-V curves are measured for both cavity-polariton and half-cavity samples in order to study if the conductivity of the organic material is enhanced by cavity polaritons.

6.1.2 Cavity-Polariton Enhanced NLO

In Chapter 3, upper-polariton enhanced third-harmonic generation was demonstrated using TE-polarized fundamental wavelength. As shown in Fig. 6.2, for the upper-polariton state at λ_1, THG is enhanced with a fundamental wavelength of $3\lambda_1$. However, there are several questions need to be answered with further study:

- Lower-polariton enhanced THG has not been observed with our cavity polariton samples in the ultrastrong coupling regime. As the lower polariton wavelength is longer than 710 nm, the fundamental wavelength for THG experiment should be longer than 2130 nm, which is beyond the output wavelength of our laser system. Therefore, to prepare cavity polariton samples with smaller vacuum Rabi splitting is required to experimentally investigate both upper- and lower-polariton enhanced THG with our current laser beam source, which is shown in Fig. 6.2. THG is

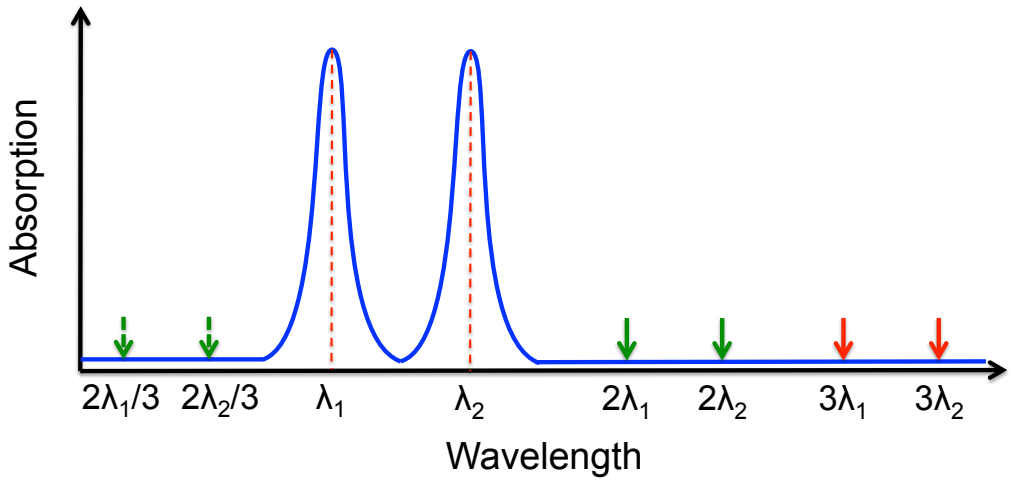

Figure 6.2. Schematic illustration of the nonlinear optical process involving cavity-polariton states with different fundamental wavelengths.

expected to be enhanced with fundamental wavelengths of $3\lambda_1$ and $3\lambda_2$ for the upper-polariton state at λ_1 and the lower-polariton state at λ_2, respectively.

- THG experiments with TM-polarized fundamental wavelength have not been well investigated. In this case, it will be very intricate: first, the induced nonlinear polarization is usually more complicated for TM-polarization than TE-polarization; second, the plasmonic effect of metallic surface may become significant for TM-polarzation. This study will help understand polarization-dependent nonlinear optical response of organic cavity polaritons.
- In addition, it has been demonstrated that two-photon resonance of organic nonlinear molecules leads to THG enhancement, which was explained by a modified three-level model.[192] Considering the characteristic light-matter hybridization, it is thus interesting to study the effect of two-photon resonance of cavity polaritons on the nonlinear optical response. As shown in Fig. 6.2, organic cavities can be pumped by wavelengths of $2\lambda_1$ and $2\lambda_2$, which are two-photon-resonant with

upper-polariton state at λ_1 and the lower-polariton state at λ_2, respectively, and investigate if the THG response is enhanced at wavelengths of $2\lambda_1/3$ and $2\lambda_2/3$.

6.2 Strong Coupling between Surface Plasmons and Organic Cavity Polaritons

Beside the strong and ultrastrong exciton-photon coupling in microcavities, organic materials have been used for the demonstration of strong coupling with surface plasmons (SP).[193] In this case the molecular excitations interact with surface waves propagating on a metallic interface.[194] The strong coupling with plasmon has been demonstrated with different types of organics[194–197] and plasmon geometries: propagating and localized plasmons.[198–200]

Here, we introduce a scheme to investigate if the coupling between surface plasmons and organic cavity polaritons can be achieved. Fig. 6.3(a) shows the experimental reflectometry in the Kretschmann geometry. The cavity sample is positioned on an hemispherical prism on the glass side with Glycerol to ensure the optical index continuity between the prism and the glass substrate. The incident light through the prism is coupled to the SP when its wave vector projection on the Ag plane matches the wave vector of the SP located at the Ag-organic thin film interface. Also, organic cavity polartons are formed as a results of strong exciton-photon coupling. Whether surface plasmons are strongly coupled with cavity polaritons can be demonstrated by analyzing the momentum-energy dispersion derived from angle-resolved reflectivity spectra.

Moreover, the photoluminescence emission can be measured with two detection configurations shown in Fig. 6.3(b). The sample is excited by short-wavelength laser

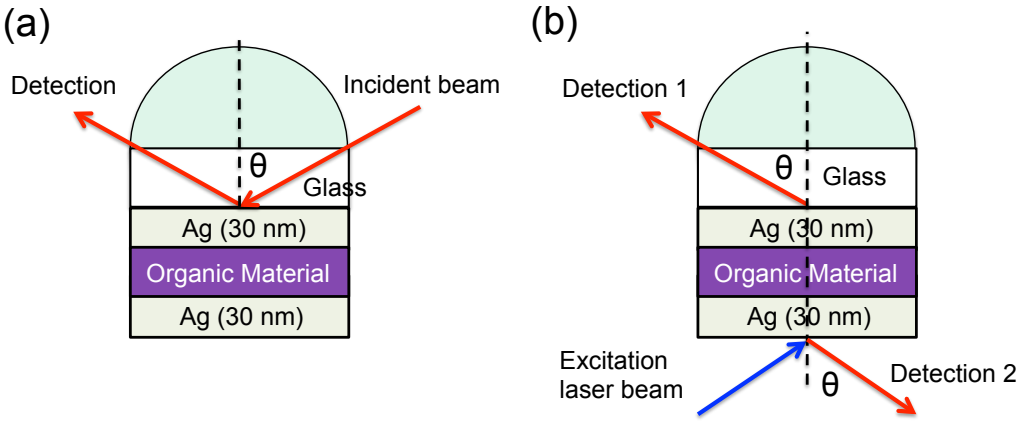

Figure 6.3. (a) Schematic of the reflectometry experiment showing the sample and hemispherical prism. (b) Geometry of the luminescence experiments with two detection configurations.

beam with a fixed incident angle, and the emission signal can be detected in those two directions while varying the detection angle. The emission spectra might be different for those two detection configurations if there is strong coupling between surface plasmons and cavity polaritons. This study will help understand the light-matter interaction in a complicated system, and is of importance for both theory development and practical applications.

6.3 2D Perovskite Photovoltaics

As mentioned in Chapter 4, there is no direct measurement results reported for the charge-carrier transport properties of 2D perovskite materials, which is crucial to the performance of photovoltaic devices. In particular, charge-carrier mobility and recombination rate are the key parameters which determine the charge-carrier transport. Therefore, experiments can be performed to investigate these two quantities for 2D perovskite materials.

6.3.1 Mobility Measurement by Time-of-Flight

Charge-carrier mobilities can be measured by Time-of-Flight (TOF) technique, see Fig. 6.4(a), which generates charge carrier sheets from a short absorption depth that travel along the sample when applying a bias voltage across the counter electrodes. A transient current is measured as the charge carriers move towards the opposite electrode with the transit time t_T and traveling distance L by an electric field E;[201,202] the charge-carrier mobility is then defined as

$$\mu = L/Et_T \tag{6.1}$$

Both the hole and electron mobility can be independently measured by reversing the bias. Also, temperature-dependent charge-carrier mobilities measurements can be accomplished, as the morphology and crystalline structure of 2D perovskites depends on the temperature.

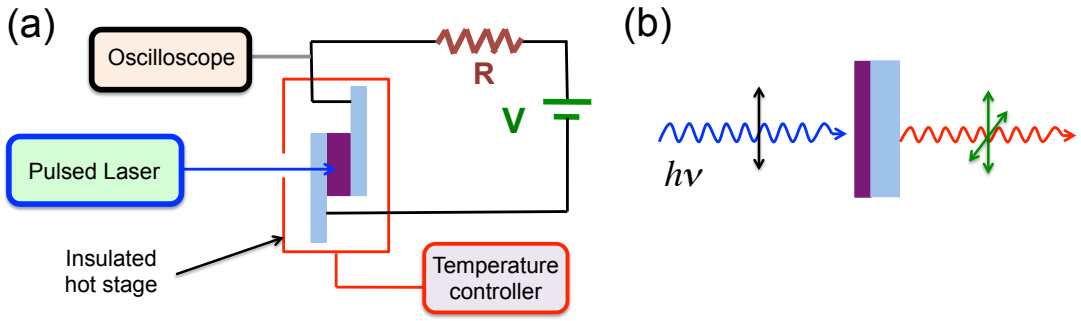

Figure 6.4. (a) The schematic of time-of-flight setup. (b) The schematic of fluorescence-anisotropy measurements.

6.3.2 Time-Resolved photoluminescence of 2D Perovskites

Time-resolved photoluminescence measurements can be used to determine the monomolecular decay rate k_1 of perovskite materials,[203] and charge-carrier dynamics in 2D perovskite film can be investigated using this technique.

In addition, due to the anisotropic structure, the photoluminescence of 2D perovskites might be strongly polarization-dependent. Compared to their 3D counterparts, 2D perovskites are expected to exhibit more significant fluorescence-anisotropy. Therefore, the fluorescence anisotropy of 2D perovskites can be investigated, as illustrated schematically in Fig. 6.4(b), 2D perovskite samples are excited with a linearly (TE or TM) polarized laser beam, and the time-resolved photoluminescence will be recorded, using a polarizer in front of the detector, for TE and TM polarization, respectively. Thus, the fluorescence anisotropy r is expressed as a function of measured fluorescence intensities of polarization along different axes:[204]

$$r = \frac{I_{\parallel} - GI_{\perp}}{I_{\parallel} + 2GI_{\perp}} \tag{6.2}$$

where $I_{\parallel}$ and $I_{\perp}$ are the intensities of the parallel and perpendicular polarized emissions, when the sample is excited with linearly polarized light. The quantity G represents the instrument correction factor accounting for the polarization bias of the detection system, which can be determined by calibrating the system with standard dyes.

References

[189] J. Feist and F. J. Garcia-Vidal, "Extraordinary exciton conductance induced by strong coupling," Phys. Rev. Lett. **114**, 196402 (2015).

[190] J. Schachenmayer, C. Genes, E. Tignone, and G. Pupillo, "Cavity-enhanced transport of excitons," Phys. Rev. Lett. **114**, 196403 (2015).

[191] E. Orgiu, J. George, J. Hutchison, E. Devaux, J. F. Dayen, B. Doudin, F. Stellacci, C. Genet, P. Samor, and T. W. Ebbesen, "Conductivity in organic semiconductors hybridized with the vacuum field," Nat. Mater. **14**, 1123 (2015).

[192] J. H. Andrews, J. D. V. Khaydarov, K. D. Singer, D. L. Hull, and K. C. Chuang, "Characterization of excited states of centrosymmetric and noncentrosymmetric squaraines by third-harmonic spectral dispersion," J. Opt. Soc. Am. B **12**, 2360 (1995).

[193] J. Bellessa, C. Bonnand, J. C. Plenet, and J. Mugnier, "Strong coupling between surface plasmons and excitons in an organic semiconductor," Phys. Rev. Lett. **93**, 036404 (2004).

[194] J. Bellessa, C. Symonds, J. Laverdant, Jean-Michel Benoit, J. C. Plenet, and S. Vignoli, "Strong Coupling between Plasmons and Organic Semiconductors," Electronics **3**, 303 (2014).

[195] T. K. Hakala, J. J. Toppari, A. Kuzyk, M. Pettersson, H. Tikkanen, H. Kunttu, and P. Törmä, "Vacuum rabi splitting and strong-coupling dynamics for surface-plasmon polaritons and rhodamine 6G molecules," Phys. Rev. Lett. **103**, 053602 (2009).

[196] C. Symonds, J. Bellessa, J. C. Plenet, A. Bréhier, R. Parashkov, J. S. Lauret, and E. Deleporte, "Emission of hybrid organic-inorganic exciton/plasmon mixed states," Appl. Phys. Lett. **90**, 091107 (2007).

[197] A. Salomon, S. Wang, J. A. Hutchison, C. Genet, and T. W. Ebbesen, "Strong light-molecule coupling on plasmonic arrays of different symmetry," ChemPhysChem **14**, 1882 (2013).

[198] G. A. Wurtz, P. R. Evans, W. Hendren, R. Atkinson, W. Dickson, R. J. Pollard, A. V. Zayats, W. Harrison, and C. Bower, "Molecular plasmonics with tunable exciton-plasmon coupling strength in J-aggregate hybridized Au nanorod assemblies," Nano Lett. **7**, 1297 (2007).

[199] N. T. Fofang, T.-H. Park, O. Neumann, N. A. Mirin, P. Nordlander, and N. J. Halas, "Plexcitonic nanoparticles: Plasmon-exciton coupling in nanoshell-J-aggregate complexes," Nano Lett. **8**, 3481 (2008).

[200] J. Bellessa, C. Symonds, K. Vynck, A. Lemaitre, A. Brioude, L. Beaur, J. C. Plenet, P. Viste, D. Felbacq, E. Cambril, and P. Valvin, "Giant Rabi splitting between localized mixed plasmon-exciton states in a two-dimensional array of nanosize metallic disks in an organic semiconductor," Phys. Rev. B **80**, 033303 (2009).

[201] N. J. Dawson, M. S. Patrick, S. Paul, B. Ellman, A. Semyonov, R. J. Twieg, R. Matthews, E. Pentzer, and K. D. Singer, "Interfacial trapping in an aged discotic liquid crystal semiconductor," J. Appl. Phys. **118**, 085502 (2015).

[202] B. Maynard, Q. Long, E. A. Schiff, M. Yang, K. Zhu, R. Kottokkaran, H. Abbas, and V. L. Dalal, "Electron and hole drift mobility measurements on methylammonium lead iodide perovskite solar cells," Appl. Phys. Lett. **108**, 173505 (2016).

[203] C. Wehrenfennig, M. Liu, H. J. Snaith, M. B. Johnston, and L. M. Herz, "Homogeneous emission line broadening in the organo lead halide perovskite $CH_3NH_3PbI_{3-x}Cl_x$," J. Phys. Chem. Lett. **5**, 1300 (2014).

[204] Y. Jiang, X. Wen, A. Benda, R. Sheng, A. W. Y. Ho-Baillie, S. Huang, F. Huang, Y.-B. Cheng, and M. A. Green, "Time-resolved fluorescence anisotropy study of organic lead halide perovskite," Sol. Energy Mater Sol. Cells **151**, 102 (2016).

Appendix A
Spectroscopic Ellipsometry

Spectroscopic ellipsometry is an optical technique for surface and thin films analysis. It is based on the measurement of the change of in polarization state of a light beam caused by the reflection on the material surface or the transmission through the material. From the change in state of polarization one can deduce film thickness and optical properties of the material. Furthermore ellipsometry is a fast and non-destructive optical measurement technique.

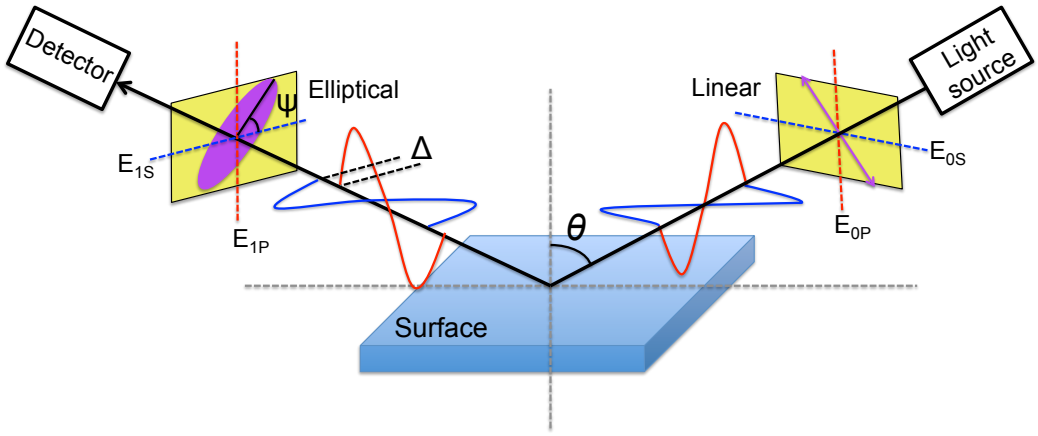

Figure A.1. Geometry of an ellipsometric experiment.

The directly measured quantities in polarization modulation ellipsometers are the first and second harmonics of the base modulation frequency of the polarized light, I_S and I_C, after reflection from the sample surface

$$I = I_1 \left(I_0 + I_S \sin\left(\delta\right) + I_C \cos\left(\delta\right) \right) \tag{A.1}$$

where I is the total light intensity, I_1 and I_0 are time-independent parameters, and δ is the time-dependent phase. Ellipsometric data are frequently expressed by the

amplitude ratio Ψ and phase difference δ between s- and p-polarization

$$\rho = \frac{r_p}{r_s} = \tan(\Psi)\exp(i\Delta) \tag{A.2}$$

where

$$\tan(\Psi) = \frac{|r_p|}{|r_s|} \quad 0^o \leq \Psi \leq 90^o \tag{A.3}$$

and

$$\Delta = \delta_p - \delta_s \quad 0^o \leq \Delta \leq 360^o \tag{A.4}$$

where $|r_p|$ and $|r_s|$ are the amplitude of the reflection coefficients for p- and s-polarization, respectively, and δ_p and δ_s are their respective phases. These quantities are parametrizations of I_S and I_C

$$\begin{aligned} I_S &= 2\,\mathrm{Im}\left(\frac{r_s r_p^*}{r_s r_s^* + r_p r_p^*}\right) = \sin(2\Psi)\sin(\Delta) \\ I_C &= 2\,\mathrm{Re}\left(\frac{r_s r_p^*}{r_s r_s^* + r_p r_p^*}\right) = \sin(2\Psi)\cos(\Delta) \end{aligned} \tag{A.5}$$

Appendix B
Transfer Matrix Theory

1 Linear Transfer Matrix

Let the z axis be perpendicular to the surface of the multilayer structure and xz be the plane of pumping wave incidence (Fig. B.1). A monochromatic linearly polarized fundamental wave with frequency ω, wave vector $\mathbf{k}_1^+$, and amplitude $\mathbf{E}_1^+$ propagates in half-space 1 at angle θ_1 to the normal to the surface We assume that the multilayer film is optically inactive and nonmagnetic; s- and p-polarized waves will therefore be considered separately. The electromagnetic field in the jth layer is a superposition of two plane forward waves (propagating in the positive direction along the z axis) and backward,

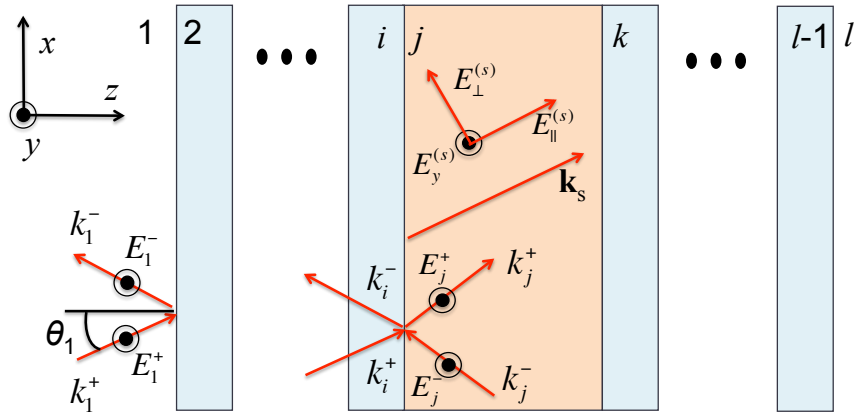

Figure B.1. Schematic of a multilayer structure, showing (in layer 1) the coordinate axes used and the orientation of the E-field basis vectors associated with $\mathbf{k}_1^+$ and $\mathbf{k}_1^-$ for s polarization and (in layer j) the components of $\mathbf{E}^{(s)}$, induced by the nonlinear polarization $\mathbf{P}^{(NL)}$, associated with a given source-wave vector $\mathbf{k}_s$.

$$\begin{aligned}\mathbf{E}_j^\omega(z,t) = \mathbf{E}_j^+ \exp\left(ik_{z,j}^\omega(z-d_{ij}) + \left(ik_{x,j}^\omega x - i\omega t\right)\right) \\ + \mathbf{E}_j^- \exp\left(-ik_{z,j}^\omega(z-d_{ij}) + \left(ik_{x,j}^\omega x - i\omega t\right)\right)\end{aligned} \tag{B.1}$$

where $k^{\omega}_{z,j} = |\mathbf{k}_j| \cos\theta_j$, $k^{\omega}_{x,j} = |\mathbf{k}_j| \sin\theta_j$. d_{ij} is the z coordinate of the boundary between the ith and jth layers, $\mathbf{k}_j$ is the wave vector, and θ_j is the angle of refraction of the pumping wave in the jth layer. The $\exp\left(ik^{\omega}_{x,j}x - i\omega t\right)$ term will further be omitted because of the translational invariance of the problem in the xy plane and its stationary character. The field at the left boundary of the jth layer is represented by the two-component vector $\mathbf{E}_j \equiv \left(E^+_j + E^-_j\right)$; the first component of this vector is the amplitude of the forward wave and the second one, that of the backward wave. The relation between $\mathbf{E}_j$ and $\mathbf{E}_k$ in the kth layer at its left boundary is given by the two 2×2 matrices

$$\begin{pmatrix} E^+_k \\ E^-_k \end{pmatrix} = \begin{pmatrix} 1/t_{kj} & r_{kj}/t_{kj} \\ r_{kj}/t_{kj} & 1/t_{kj} \end{pmatrix} \begin{pmatrix} e^{ik^{\omega}_{z,j}d_j} & 0 \\ o & e^{-ik^{\omega}_{z,j}d_j} \end{pmatrix} \begin{pmatrix} E^+_j \\ E^-_j \end{pmatrix} \tag{B.2}$$

Here, the first matrix contains the Fresnel reflectivity r_{kj} and transmissivity t_{kj} for the wave incident from the kth to the jth layer and relates fields to the left and right of the kjth interface. In what follows, this matrix is denoted by $\mathbf{M}_{kj}$. The second $\mathbf{\Phi}_j(d_j)$ matrix describes field propagation in the jth layer of thickness d_j from the left to right boundary. The fields in half-spaces 1 and l can therefore be related. Under the assumption that the backward wave is absent in half-space l and that a wave with unit amplitude is incident on the 1-2 boundary, we obtain

$$\begin{pmatrix} t \\ 0 \end{pmatrix} = \begin{pmatrix} T_{11} & T_{12} \\ T_{21} & T_{22} \end{pmatrix} \begin{pmatrix} 1 \\ r \end{pmatrix} \tag{B.3}$$

Here, r and t are the reflectivity and transmissivity of the multilayer film as a whole. They are determined from Eq. B.3, which gives

$$r = -\frac{T_{21}}{T_{22}}, \quad t = \frac{T_{11}T_{22} - T_{12}T_{21}}{T_{22}}$$

where $T_{\alpha\beta}$ are the elements of the transfer matrix for the multilayer film as a whole,

$$\mathbf{T} \equiv \mathbf{M}_{l(l-1)}\mathbf{\Phi}_{(l-1)} \cdots \mathbf{\Phi}_2\mathbf{M}_{21} \tag{B.4}$$

The fundamental field distribution within the jth layer is given by

$$\mathbf{E}_j^{\omega}(z) = \mathbf{\Phi}_j\mathbf{M}_{j(j-1)}\mathbf{\Phi}_{(j-1)} \cdots \mathbf{\Phi}_2\mathbf{M}_{21} \begin{pmatrix} 1 \\ \\ r \end{pmatrix} \tag{B.5}$$

Spatial distribution Eq. B.5 can be used to calculate the spatial distribution of the induced nonlinear polarization wave, for example, inhomogeneous second and third harmonic can be calculated.

2 Nonlinear Transfer Matrix for THG

Let the jth layer be nonlinear. The interference of the coupled $\mathbf{E}^{(s)}$ and free $\mathbf{E}_j$ third harmonic waves is included in the boundary conditions, which, for the ij-th and jk-th boundaries, have the form

$$\begin{aligned} \mathbf{\Phi}_i\mathbf{E}_i &= \mathbf{M}_{ij}\mathbf{E}_j + \mathbf{M}_i^{(s)}\mathbf{E}^{(s)} \\ \mathbf{M}_{kj}\mathbf{\Phi}_j\mathbf{E}_j &+ \mathbf{M}_k^{(s)}\mathbf{\Phi}^{(s)}\mathbf{E}^{(s)} = \mathbf{E}_k \end{aligned} \tag{B.6}$$

The amplitude of the inhomogeneous third-harmonic wave in Eq. B.6 is calculated in the jth nonlinear layer at its left boundary, and all homogeneous waves are third-harmonic waves. Matrices $\mathbf{M}$ with index (s) are constructed similarly to the usual transfer matrices, but the Fresnel coefficients in their elements contain refractive indexes for the inhomogeneous third-harmonic wave in the nonlinear layer and the free third harmonic in the layer whose number equals the lower index of the matrix. The $\mathbf{\Phi}^{(s)}$ matrix is similar to $\mathbf{\Phi}_j$ and is obtained from the latter by replacing the wave vectors of the free third harmonic with the wave vectors of the inhomogeneous wave.

Eq. B.6 yields

$$\mathbf{E}_k = \mathbf{M}_{kj}\mathbf{\Phi}_j\left(\mathbf{M}_{ji}\mathbf{\Phi}_i\mathbf{E}_i + \mathbf{S}_j\right) \tag{B.7}$$

where the vector

$$\mathbf{S}_j = \left(\mathbf{\Phi}_j^{-1}\mathbf{M}_j^{(s)}\mathbf{\Phi}^{(s)} - \mathbf{M}_j^{(s)}\right)\mathbf{E}^{(s)} \tag{B.8}$$

where the $\mathbf{\Phi}_j^{-1}$ matrix is inverse to $\mathbf{\Phi}_j$. Eq. B.7 determines the third-harmonic field in the kth layer as a superposition of the waves transmitted from the ith layer and generated in the jth layer by nonlinear sources. Eq. B.8 contains the contribution of the nonlinear jth layer to the third-harmonic wave; the term in parentheses takes into account the interference of the homogeneous and inhomogeneous waves. Under the assumption that no external field with the third-harmonic wavelength is incident on the multilayer film, Eq. B.7 can be rewritten as

$$\mathbf{R}_{jl}\begin{pmatrix} E_l^+(j) \\ 0 \end{pmatrix} - \mathbf{L}_{j1}\begin{pmatrix} 0 \\ E_l^-(j) \end{pmatrix} = \mathbf{S}_j \tag{B.9}$$

where the matrices

$$\begin{aligned} \mathbf{R}_{jl} &\equiv \mathbf{\Phi}_j^{-1}\mathbf{M}_{jk}\mathbf{\Phi}_k^{-1}\mathbf{M}_{k(k+1)}\cdots\mathbf{\Phi}_{l-1}^{-1}\mathbf{M}_{(l-1)l} \\ \mathbf{L}_{j1} &\equiv \mathbf{M}_{ji}\mathbf{\Phi}_i\mathbf{M}_{i(i-1)}\cdots\mathbf{\Phi}_2\mathbf{M}_{21} \end{aligned} \tag{B.10}$$

characterize the propagation of homogeneous third-harmonic waves from half-spaces 1 and l to the jth layer. It follows that, given $\mathbf{S}_j$ we can find the amplitude and phase of the third-harmonic fields $E_1^-(j)$ and $E_l^+(j)$ generated in the jth layer and emerging from the multilayer film into the vacuum (half-space 1) and substrate (half-space l). The total third-harmonic field in the substrate or vacuum is the sum of $E_l^+(j)$ or $E_1^-(j)$ taken over all layers.

Appendix C
List of Conference Presentations, Conference Proceedings and Journal Publications

1 Conference Presentations

- Frontiers in Optics/Laser Science Conference (FiO/LS) 2017, Washington D.C.
  Poster Presentation: Linear and nonlinear optical properties of organic cavity polaritons in the ultrastrong regime
- Conference for Laser and Electro-optics (CLEO) 2016, San Jose, CA
  Oral Presentation: Coupling of exciton-polaritons in low-Q coupled microcavities beyond the rotating wave approximation
- American Physical Society (APS) March Meeting 2015, San Antonio, TX
  Oral Presentation: Ultrastrong exciton-photon coupling in single and coupled organic semiconductor microcavities

2 Conference Proceedings

(1) B. Liu, M. Crescimanno, and K. D. Singer, "Linear and nonlinear optical properties of organic cavity polaritons in the ultrastrong regime," in FiO/LS: 2017, (JTu3A.51). Washington D.C. Optical Society of America.

(2) B. Liu, P. Rai, J. Grezmak, R. Twieg, and K. D. Singer, "Coupling of exciton-polaritons in low-Q coupled microcavities beyond the rotating wave approximation," in CLEO: 2016, (FTu4D.3). San Jose, California: Optical Society of America.

(3) B. Liu, R. Bramante, B. Valle, T. Khattab, J. Williams, R. Twieg, and K. D. Singer, "Ultrastrong exciton-photon coupling in single and coupled organic semiconductor microcavities," in APS March: 2015, (G8-3). San Antonio, Texas: American Physical Society.

3 Journal Publications

(1) B. Liu, M. Crescimanno, and K. D. Singer, "Resonant cavity-polariton enhanced third-harmonic generation in organic microcavities," (in preparation)

(2) B. Liu, C. M. M. Soe, C. C. Stoimpos, W. Nie, H. Tsai, K. Lim, A. D. Mohite, M. G. Kanatzidis, T. J. Marks, and K. D. Singer, "Optical properties and modeling of 2D perovskite solar cells," Solar RRL **1**, 1700062 (2017).

(3) B. Liu, P. Rai, J. Grezmak, R. J. Twieg, and K. D. Singer, "Coupling of exciton-polaritons in low-Q coupled microcavities beyond the rotating wave approximation," Phys. Rev. B **92**, 155301 (2015).

Bibliography

A. R. Parker and H. E. Townley, "Biomimetics of photonic nanostructures," Nat. nanotechnol. **2**, 347 (2007).

K. D. Singer, T. Kazmierczak, J. Lott, H. Song, Y. Wu, J. Andrews, E. Baer, A. Hiltner, and C. Weder, "Melt-processed all-polymer distributed Bragg reflector laser," Opt. Express **16**, 10358 (2008).

P. M. Kaminski, F. Lisco, and J. M. Walls, "Multilayer broadband anti-reflective coating for more efficient thin film solar cells," IEEE J. Photovoltaics **4**, 452 (2014).

L. El Chaar, L. A. lamont, and N. El Zein, "Review of photovoltaic technologies," Renew. Sustainable Energy Rev. **15**, 2165 (2011).

M. Fox, "Quantum Optics: An Introduction," Oxford University Press, (2006).

T. W. Ebbesen, H. J. Lezec, H. F. Ghaemi, T. Thio, and P. A. Wolff, "Extraordinary optical transmission through sub-wavelength hole arrays," Nature **391**, 667 (1998).

H. Yokoyama, Y. Nambu, T. Kawakami, in: E. Burstein, and C. Weisbuch (Eds.), "Confined Electrons and Photons: New Physics and Applications," Plenum Press, New York, (1995).

E. M. Purcell, "Spontaneous emission probabilities at radio frequencies," Phys. Rev. **69**, 681 (1946).

C. Weisbuch, M. Nishioka, A. Ishikawa, and Y. Arakawa, "Observation of the coupled exciton-photon mode splitting in a semiconductor quantum microcavity," Phys. Rev. Lett. **69**, 3314 (1992).

V. Savona, L. C. Andreani, P. Schwendimann, and A. Quattropani, "Quantum well excitons in semiconductor microcavities: Unified treatment of weak and strong coupling regimes," Solid State Commun. **93**, 733 (1995).

M. S. Skolnick, T. A. Fisher, and D. M. Whittaker, "Strong coupling phenomena in quantum microcavity structures," Semicond. Sci. Technol. **13**, 645 (1998).

E. T. Jaynes and F. W. Cummings, "Comparison of quantum and semiclassical radiation theories with application to the beam maser," Proc. IEEE **51**, 89 (1963).

X. Liu, "Control of Exciton Photon Coupling in Nano-structures," Thesis pp. 25-27 (2014).

J. J. Hopfield, "Theory of the contribution of excitons to the complex dielectric constant of crystals," Phys. Rev. **112**, 1555 (1958).

G. Güniter, A. A. Anappara, J. Hees, A. Sell, G. Biasiol, L. Sorba, S. De Liberato, C. Ciuti, A. Tredicucci, A. Leitenstorfer, and R. Huber, "Sub-cycle switch-on of ultrastrong light-matter interaction," Nature **458**, 178 (2009).

A. A. Anappara, S. De Liberato, A. Tredicucci, C. Ciuti, G. Biasiol, L. Sorba, and F. Beltram, "Signatures of the ultrastrong light-matter coupling regime," Phys. Rev. B **79**, 201303(R) (2009).

Y. Todorov, A. M. Andrews, R. Colombelli, S. De Liberato, C. Ciuti, P. Klang, G. Strasser, and C. Sirtori, "Ultrastrong light-matter coupling regime with polariton dots," Phys. Rev. Lett. **105**, 196402 (2010).

T. Schwartz, J. A. Hutchison, C. Genet, and T. W. Ebbesen, "Reversible switching of ultrastrong light-molecule coupling," Phys. Rev. Lett. **106**, 196405 (2011).

S. Kéna-Cohen, S. A. Maier, and D. D. C. Bradley, "Ultrastrongly coupled exciton-polaritons in metal-clad organic semiconductor microcavities," Adv. Opt. Mater. **1**, 827 (2013).

S. Gambino, M. Mazzeo, A. Genco, O. Stefano, S. Savasta, S. Patanè, D. Ballarini, F. Mangione, G. Lerario, D. Sanvitto, and G. Gigli, "Exploring light-matter interaction phenomena under ultrastrong coupling regime," ACS Photonics **1**, 1042 (2014).

B. Liu, P. Rai, J. Grezmak, R. J. Twieg, and K. D. Singer, "Coupling of exciton-polaritons in low-Q coupled microcavities beyond the rotating wave approximation," Phys. Rev. B **92**, 155301 (2015).

C. Ciuti and G. Bastard, "Quantum vacuum properties of the intersubband cavity polariton field," Phys. Rev. B **72**, 115303 (2005).

S. Wang, "Strong light-molecule coupling: routes to new hybrid materials," Thesis pp. 27-28 (2015).

S. De Liberato, "Light-matter decoupling in the deep strong coupling regime: the breakdown of the Purcell effect," Phys. Rev. Lett. **112**, 016401 (2014). M. Bamba and T. Ogawa, "System-environment coupling derived by Maxwell's boundary conditions from the weak to the ultrastrong light-matter-coupling regime," Phys. Rev. A **88**, 013814 (2013).

J. Casanova, G. Romero, I. Lizuain, J. J. Garca-Ripoll, and E. Solano, "Deep strong coupling regime of the Jaynes-Cummings model," Phys. Rev. Lett. **105**, 263603 (2010).

D. Hagenmüller, S. De Liberato, and C. Ciuti, "Ultrastrong coupling between a cavity resonator and the cyclotron transition of a two-dimensional electron gas in the case of an integer filling factor," Phys. Rev. B **81**, 235302 (2010).

R. W. Boyd, "Nonlinear Optics," Academic Press, 3rd Edition (2008).

P. A. Franken, A. E. Hill, C. W. Peters, and G. Weinreich, "Generation of optical harmonics," Phys. Rev. Lett. **7**, 118 (1961).

T. H. Maiman, "Stimulated optical radiation in ruby," Nature **187**, 493 (1960).

R. W. Terhune, P. D. Maker, and C. V. Savage, "Optical harmonic generation in calcite," Phys. Rev. Lett. **8**, 404 (1962).

E. J. Woodbury and W. K. Ng, "Ruby laser operation in the near IR," Proc. IRE **50**, 2367 (1962).

R. Y. Chiao, C. H. Townes, and B. P. Stoicheff, "Stimulated Brillouin scattering and coherent generation of intense hypersonic waves," Phys. Rev. Lett. **12**, 592 (1964).

R. W. Terhune, P. D. Maker, and C. M. Savage, "Measurements of nonlinear light scattering," Phys. Rev. Lett. **14**, 681 (1965).

R. Righini, "Ultrafast optical Kerr effect in liquids and solids," Science **1386**, 681 (1993).

R. Y. Chiao, E. Garmire, and C. H. Townes, "Self-trapping of optical beams," Phys. Rev. Lett. **13**, 479 (1964).

M. Kaiser and C. G. B. Garrett, "Two-photon excitation in CaF_2: Eu^{2+}," Phys. Rev. Lett. **7**, 229 (1961).

D. M. Chapin, C. S. Fuller, and G. L. Pearson, "A new silicon p-n Junction photocell for converting solar radiation into electrical power," J. Appl. Phys. **25**, 676 (1954).

M. A. Green, K. Emery, Y. Hishikawa, W. Warta, and E. D. Dunlop, "A new silicon p-n Junction photocell for converting solar radiation into electrical power," Prog. Photovolt. Res. Appl. **20**, 12 (2012).

B. Parida, S. Iniyan, and R. Goic, "A review of solar photovoltaic technologies," Renew. Sustainable Energy Rev. **15**, 1625 (2011).

W. Shockley and H. J. Queisser, "Detailed balance limit of efficiency of p-n junction solar cells," J. Appl. Phys. **32**, 510 (1961).

A. Kojima, K. Teshima, Y. Shirai, and T . Miyasaka, "Organometal halide perovskites as visible-light sensitizers for photovoltaic cells," J . Am. Chem. Soc. **131**, 6050 (2009).

H.-S. Kim, C.-R. Lee, J.-H. Im, K.-B. Lee, T. Moehl, A. Marchioro, S.-J. Moon, R. Humphry-Baker, J.-H. Yum, J. E. Moser, M. Grätzel, and N.-G. Park, "Lead iodide perovskite sensitized all-solid-state submicron thin film mesoscopic solar Cell with efficiency exceeding 9%," Sci. Rep. **2**, 591 (2012).

J. S. Manser, J. A. Christians, and P. V. Kamat, "Intriguing optoelectronic properties of metal halide perovskites," Chem. Rev. **116**, 12956 (2016).

M. Grätzel, "The rise of highly efficient and stable perovskite solar cells," Acc. Chem. Res. **50**, 487 (2017).

S. Günes, H. Neugebauer, and N. S. Sariciftci, "Conjugated polymer-based organic solar cells," Chem. Rev. **107**, 1324 (2007).

I. D. Parker, "Carrier tunneling and device characteristics in polymer light-emitting diodes," J. Appl. Phys. **75**, 1656 (1994).

J. M. Nunzi, "Organic photovoltaic materials and devices," C. R. Physique **3**, 523 (2002).

B. Valle, "Design of Multilayer Optical Media: Organic Photovoltaics and Optical Data Storage," Thesis pp. 7 (2013).

J. Rostalski and D. Meissner, "Monochromatic versus solar efficiencies of organic solar cells," Sol. Energy Mater. Sol. Cells **61**, 87 (2000).

J.-H. Im, J. Chung, S.-J. Kim, and N.-G. Park, "Synthesis, structure, and photovoltaic property of a nanocrystalline 2H perovskite-type novel sensitizer ($CH_3CH_2NH_3$)PbI_3," Nanoscale Res. Lett. **7**, 353 (2012).

G. E. Eperon, S. D. Stranks, C. Menelaou, M. B. Johnston, L. M. Herz, and H. J. Snaith, "Formamidinium lead trihalide: a broadly tunable perovskite for efficient planar heterojunction solar cells," Energy Environ. Sci. **7**, 982 (2014).

M. I. Ahmed, A. Habib, and S. S. Javaid, "Perovskite solar cells: potentials, challenges, and opportunities," Int. J. Photoenergy **2015**, 1 (2015).

F. Hao, C. C. Stoumpos, R. P. H. Chang, and M. G. Kanatzidis, "Anomalous band gap behavior in mixed Sn and Pb perovskites enables broadening of absorption spectrum in solar cells," J. Am. Chem. Soc. **136**, 8094 (2014).

S. D. Wolf, J. Holovsky, S.-J. Moon, P. Löper, B. Niesen, M. Ledinsky, F.-J. Haug, J.-H. Yum, and C. Ballif, "Organometallic halide perovskites: sharp optical absorption edge and its relation to photovoltaic performance," J. Phys. Chem. Lett. **5**, 1035 (2014).

A. Miyata, A. Mitioglu, P. Plochocka, O. Portugall, J. T. W. Wang, S. D. Stranks, H. J. Snaith, and R. J. Nicholas, "Direct measurement of the exciton binding energy and effective masses for charge carriers in organic-inorganic tri-halide perovskites," Nat. Phys. **11**, 582 (2015).

K. Galkowski, A. Mitioglu, A. Miyata, P. Plochocka, O. Portugall, G. E. Eperon, J. T.-W. Wang, T. Stergiopoulos, S. D. Stranks, H. Snaith, and R. J. Nicholas, "Determination of the exciton binding energy and effective masses for methylammonium and formamidinium lead tri-halide perovskite semiconductors," Energy Environ. Sci. **9**, 962 (2016).

C. Wehrenfennig, G. E. Eperon, M. B. Johnston, H. J. Snaith, and L. M. Herz, "High charge carrier mobilities and lifetimes in organolead trihalide perovskites," Adv. Mater. **26**, 1584 (2014).

M. B. Johnston and L. M. Herz, "Hybrid perovskites for photovoltaics: charge-carrier recombination, diffusion, and radiative efficiencies," Acc. Chem. Res. **49**, 146 (2016).

S. D. Stranks and H. J. Snaith, "Metal-halide perovskites for photovoltaic and light-emitting devices," Nat. Nanotechnol. **10**, 391 (2015).

V. Gonzalez-Pedro, E. J. Juarez-Perez, W.-S. Arsyad, E. M. Barea, F. Fabregat-Santiago, I. Mora-Sero, and J. Bisquert, "General working principles of $CH_3NH_3PbX_3$ perovskite solar cells," Nano Lett. **14**, 888 (2014).

H. J. Snaith, A. Abate, J. M. Ball, G. E. Eperon, T. Leijtens, N. K. Noel, S. D. Stranks, J. T.-W. Wang, K. Wojciechowski, and W. Zhang, "Anomalous hysteresis in perovskite solar cells," J. Phys. Chem. Lett. **5**, 1511 (2014).

E. L. Unger, E. T. Hoke, C. D. Bailie, W. H. Nguyen, A. R. Bowring, T. Heumüller, M. G. Christoforo, and M. D. McGehee, "Hysteresis and transient behavior in current-voltage measurements of hybrid-perovskite absorber solar cells," Energy Environ. Sci. **7**, 3690 (2014).

Y. Zhang, M. Liu, G. E. Eperon, T. C. Leijtens, D. McMeekin, M. Saliba, W. Zhang, M. de Bastiani, A. Petrozza, L. M. Herz, M. B. Johnston, H. Lin, and H. J. Snaith, "Charge selective contacts, mobile ions and anomalous hysteresis in organic-inorganic perovskite solar cells," Mater. Horiz. **2**, 315 (2015).

W. Tress, N. Marinova, T. Moehl, S. M. Zakeeruddin, M. K. Nazeeruddin and M. Grätzel, "Understanding the rate-dependent J-V hysteresis, slow time component, and aging in $CH_3NH_3PbI_3$ perovskite solar cells: the role of a compensated electric field," Energy Environ. Sci. **8**, 995 (2015).

I. C. Smith, E. T. Hoke, D. Solis-Ibarra, M. D. McGehee, and H. I. Karunadasa, "A layered hybrid perovskite solar-cell absorber with enhanced moisture stability," Angew. Chem. Int. Ed. **53**, 11232 (2014).

D. H. Cao, C. C. Stoumpos, O. K. Farha, J. T. Hupp, and M. G. Kanatzidis, "2D homologous perovskites as light-absorbing materials for solar cell applications," J. Am. Chem. Soc. **137**, 7843 (2015).

H. Tsai, W. Nie, Jean-Christophe Blancon, C. C. Stoumpos, R. Asadpour, B. Harutyunyan, A. J. Neukirch, R. Verduzco, J. J. Crochet, S. Tretiak, L. Pedesseau, J. Even, M. A. Alam, G. Gupta, J. Lou, P. M. Ajayan, M. J. Bedzyk, M. G. Kanatzidis, and A. D. Mohite, "High-efficiency two-dimensional Ruddlesden-Popper perovskite solar cells," Nature **536**, 312 (2016).

B. Valle, S. Loser, J. W. Hennek, V. DeGeorge, C. Klosterman, J. H. Andrews, and K. D. Singer, "Spectral aspects of cavity tuned absorption in organic photovoltaic films," Opt. Express **20**, A954 (2012).

S. Loser, B. Valle, K. A. Luck, C. K. Song, G. Ogien, M. C. Hersam, K. D. Singer, and T. J. Marks, "High-efficiency inverted polymer photovoltaics via spectrally tuned absorption enhancement," Adv. Energy Mater. **4**, 1301938 (2014).

G. S. Solomon, M. Pelton, and Y. Yamamoto, "Single-mode spontaneous emission from a single quantum dot in a three-dimensional microcavity," Phys. Rev. Lett. **86**, 3903 (2001).

M. Saba, C. Ciuti, J. Bloch, V. Thierry-Mieg, R. André, Le Si Dang, S. Kundermann, A. Mura, G. Bongiovanni, J. L. Staehli, and B. Deveaud, "High-temperature ultrafast polariton parametric amplification in semiconductor microcavities," Nature **414**, 731 (2001).

J. M. Raimond, M. Brune, and S. Haroche, "Manipulating quantum entanglement with atoms and photons in a cavity," Rev. Mod. Phys. **73**, 565 (2001).

M. G. Raizen, R. J. Thompson, R. J. Brecha, H. J. Kimble, and H. J. Carmichael, "Normal-mode splitting and linewidth averaging for two-state atoms in an optical cavity," Phys. Rev. Lett. **63**, 240 (1989).

R. J. Holmes and S.R. Forrest, "Strong exciton-photon coupling in organic materials," Org. Electron. **8**, 77 (2007).

S. Christopoulos, G. B. H. von Högersthal, A. J. D. Grundy, P. G. Lagoudakis, A. V. Kavokin, and J. J. Baumberg, "Room-temperature polariton lasing in semiconductor microcavities," Phys. Rev. Lett. **98**, 126405 (2007).

T.-C. Lu, Y.-Y. Lai, Y.-P. Lan, S.-W. Huang, J.-R. Chen, Y.-C. Wu, W.-F. Hsieh, and H. Deng, "Room temperature polariton lasing vs. photon lasing in a ZnO-based hybrid microcavity," Opt. Express **20**, 5530 (2012).

D. G. Lidzey, D. D. C. Bradley, M. S. Skolnick, T. Virgili, S. Walker, and D. M. Whittaker, "Strong exciton-photon coupling in an organic semiconductor microcavity," Nature **395**, 53 (1998).

D. G. Lidzey, D. D. C. Bradley, T. Virgili, A. Armitage, M. S. Skolnick, and S. Walker, "Room temperature polariton emission from strongly coupled organic semiconductor microcavities," Phys. Rev. Lett. **82**, 3316 (1999).

R. J. Holmes and S. R. Forrest, "Strong exciton-photon coupling and exciton hybridization in a thermally evaporated polycrystalline film of an organic small molecule," Phys. Rev. Lett. **93**, 186404 (2004).

S. Kéna-Cohen, M. Davanço, and S. R. Forrest, "Strong exciton-photon coupling in an organic single crystal microcavity," Phys. Rev. Lett. **101**, 116401 (2008).

J. D. Plumhof, T. Stöferle, L. Mai, U. Scherf, and R. F. Mahrt, "Room-temperature Bose-Einstein condensation of cavity exciton-polaritons in a polymer," Nat. Mater. **13**, 247 (2014).

X. Liu, T. Galfsky, Z. Sun, F. Xia, E.-C. Lin, Y.-H. Lee, S. Kéna-Cohen, and V. M. Menon, "Strong light-matter coupling in two-dimensional atomic crystals," Nat. Photonics **9**, 30 (2014).

S. Wang, S. Li, T. Chervy, A. Shalabney, S. Azzini, E. Orgiu, J. A. Hutchison, C. Genet, P. Samorì, and T. W. Ebbesen, "Room-temperature Bose-Einstein condensation of cavity exciton-polaritons in a polymer," Nano Lett. **16**, 4368 (2016)

K. S. Daskalakis, S. A. Maier, R. Murray, and S. Kéna-Cohen, "Nonlinear interactions in an organic polariton condensate," Nat. Mater. **13**, 271 (2014).

D. M. Coles, N. Somaschi, P. Michetti, C. Clark, P. G. Lagoudakis, P. G. Savvidis, and D. G. Lidzey, "Polariton-mediated energy transfer between organic dyes in a strongly coupled optical microcavity," Nat. Mater. **13**, 712 (2014).

X. Zhong, T. Chervy, S. Wang, J. George, A. Thomas, J. A. Hutchison, E. Devaux, C. Genet, and T. W. Ebbesen, "Non-radiative energy transfer mediated by hybrid light-matter states," Angew. Chem. Int. Ed. **55**, 6202 (2016).

J. A. Hutchison, A. Liscio, T. Schwartz, A. Canaguier-Durand, C. Genet, V. Palermo, P. Samorì, and T. W. Ebbesen, "Tuning the Work-Function Via Strong Coupling," Adv. Mater. **25**, 2481 (2013).

G. Lerario, A. Fieramosca, F. Barachati, D. Ballarini, K. S. Daskalakis, L. Dominici, M. De Giorgi, S. A. Maier, G. Gigli, S. Kéna-Cohen, and D. Sanvitto, "Room-temperature superfluidity in a polariton condensate," Nat. Phys. **13**, 837 (2017).

J. Galego, F. J. Garcia-Vidal, and J. Feist, "Cavity-induced modifications of molecular structure in the strong-coupling regime," Phys. Rev. X **5**, 041022 (2015).

M. Mazzeo, A. Genco, S. Gambino, D. Ballarini, F. Mangione, O. Di Stefano, S. Patanè, S. Savasta, D. Sanvitto, and G. Gigli, "Ultrastrong light-matter coupling in electrically doped microcavity organic light emitting diodes," Appl. Phys. Lett. **104**, 233303 (2014).

C. R. Gubbin, S. A. Maier, and S. Kéna-Cohen, "Low-voltage polariton electroluminescence from an ultrastrongly coupled organic light-emitting diode," Appl. Phys. Lett. **104**, 233302 (2014).

R. P. Stanley, R. Houdré, U. Oesterle, M. Ilegems, and C. Weisbuch, "Coupled semiconductor microcavities," Appl. Phys. Lett. **65**, 2093 (1994).

A. Armitage, M. S. Skolnick, V. N. Astratov, D. M. Whittaker, G. Panzarini, L. C. Andreani, T. A. Fischer, J. S. Roberts, A. V. Kavokin, M. A. Kaliteevski, and M. R. Vladimirova, "Optically induced splitting of bright excitonic states in coupled quantum microcavities," Phys. Rev. B **57**, 14877 (1998).

A. Armitage, M. S. Skolnick, A. V. Kavokin, D. M. Whittaker, V. N. Astratov, G. A. Gehring, and J. S. Roberts, "Polariton-induced optical asymmetry in semiconductor microcavities," Phys. Rev. B **58**, 15367 (1998).

C. Diederichs and J. Tignon, "Design for a triply resonant vertical-emitting micro-optical parametric oscillator," Appl. Phys. Lett. **87**, 251107 (2005).

T. Lecomte, D. Taj, A. Lemaitre, J. Bloch, C. Delalande, J. Tignon, and P. Roussignol, "Polariton-polariton interaction potentials determination by pump-probe degenerate scattering in a multiple microcavity," Phys. Rev. B **89**, 155308 (2014).

C. Diederichs, J. Tignon, G. Dasbach, C. Ciuti, A. Lematre, J. Bloch, P. Roussignol, and C. Delalande, "Parametric oscillation in vertical triple microcavities," Nature **440**, 904 (2006).

S. Stelitano, G. D. Luca, S. Savasta, L. M. Scolaro, and S. Patané, "Vertical coupled double organic microcavities," Appl. Phys. Lett. **95**, 093303 (2009).

C. Symonds, C. Bonnand, J. C. Plenet, A. Bréhier, R. Parashkov, J. S. Lauret, E. Deleporte, and J. Bellessa, "Particularities of surface plasmon-exciton strong coupling with large Rabi splitting," New J. Phys. **10**, 065017 (2008).

P. A. Hobson, W. L. Barnes, D. G. Lidzey, G. A. Gehring, D. M. Whittaker, M. S. Skolnick, and S. Walker, "Strong exciton-photon coupling in a low-Q all-metal mirror microcavity," Appl. Phys. Lett. **81**, 3519 (2002).

I. Diniz, S. Portolan, R. Ferreira, J. M. Gérard, P. Bertet, and A. Auffèves, "Strongly coupling a cavity to inhomogeneous ensembles of emitters: Potential for long-lived solid-state quantum memories," Phys. Rev. A **84**, 063810 (2011).

R. Houdré, R. P. Stanley, and M. Ilegems, "Vacuum-field Rabi splitting in the presence of inhomogeneous broadening: Resolution of a homogeneous linewidth in an inhomogeneously broadened system," Phys. Rev. A **53**, 2711 (1996).

G. Panzarini, L. C. Andreani, A. Armitage, D. Baxter, M. S. Skolnick, V. N. Astratov, J. S. Roberts, A. V. Kavokin, M. R. Vladimirova, and M. A. Kaliteevski, "Exciton-light coupling in single and coupled semiconductor microcavities: Polariton dispersion and polarization splitting," Phys. Rev. B **59**, 5082 (1999).

J. J. Hopfield, "Theory of the contribution of excitons to the complex dielectric constant of crystals," Phys. Rev. **112**, 1555 (1958).

S. Wang, T. Chervy, J. George, J. A. Hutchison, C. Genet, and T. W. Ebbesen, "Quantum yield of polariton emission from hybrid light-matter states," J. Phys. Chem. Lett. **5**, 1433 (2014).

A. Ridolfo, M. Leib, S. Savasta, and M. J. Hartmann, "Photon blockade in the ultrastrong coupling regime," Phys. Rev. Lett. **109**, 193602 (2012).

T. Chervy, J. Xu, Y. Duan, C. Wang, L. Mager, M. Frerejean, J. A. W. Münninghoff, P. Tinnemans, J. A. Hutchison, C. Genet, A. E. Rowan, T. Rasing, and T. W. Ebbesen, "High-efficiency second-harmonic generation from hybrid light-matter states," Nano Lett. **16**, 7352 (2016).

F. Barachati, J. Simon, Y. A. Getmanenko, S. Barlow, S. R. Marder, and S. Kéna-Cohen, "Tunable third-harmonic generation from polaritons in the ultrastrong coupling regime," ACS Photonics (2017).

H.-C. Liao, T. L. D. Tam, P. Guo, Y. Wu, E. F. Manley, W. Huang, N. Zhou, C. M. M. Soe, B. Wang, M. R. Wasielewski, L. X. Chen, M. G. Kanatzidis, A. Facchetti, R. P. H. Chang, and T. J. Marks, "Dopant-free hole transporting polymers for high efficiency, environmentally stable perovskite solar cells," Adv. Energy Mater. **6**, 1600502 (2016).

H.-C. Liao, P. Guo, C.-P. Hsu, M. Lin, B. Wang, L. Zeng, W. Huang, C. M. M. Soe, W.-F. Su, M. J. Bedzyk, M. R. Wasielewski, A. Facchetti, R. P. H. Chang, M. G. Kanatzidis, and T. J. Marks, "Enhanced efficiency of hot-cast large-area planar perovskite solar cells/modules having controlled chloride incorporation," Adv. Energy Mater. **7**, 1601660 (2017).

W. Nie, H. Tsai, R. Asadpour, J.-C. Blancon, A. J. Neukirch, G. Gupta, J. J. Crochet, M. Chhowalla, S. Tretiak, M. A. Alam, H.-L. Wang, and A. D. Mohite, "High-efficiency solution-processed perovskite solar cells with millimeter-scale grains," Science **347**, 522 (2015).

Y. Han, S. Meyer, Y. Dkhissi, K. Weber, J. M. Pringle, U. Bach, L. Spiccia, and Y.-B. Cheng, "Degradation observations of encapsulated planar CH3NH3PbI3 perovskite solar cells at high temperatures and humidity," J. Mater. Chem. A Mater. Energy Sustain. **3**, 8139 (2015).

C. C. Stoumpos, D. H. Cao, D. J. Clark, J. Young, J. M. Rondinelli, J. I. Jang, J. T. Hupp, and M. G. Kanatzidis, "Ruddlesden-Popper hybrid lead Iodide perovskite 2D homologous semiconductors," Chem. Mater. **28**, 2852 (2016).

C. C. Stoumpos, C. M. M. Soe, H. Tsai, W. Nie, J. Blancon, D. H. Cao, F. Liu, B. Traore, C. Katan, J. Even, A. D. Mohite, and M. G. Kanatzidis, "High members of the 2D Ruddlesden-Popper halide perovskites: synthesis, optical properties, and solar cells of $(CH_3(CH_2)_3NH_3)_2(CH_3NH_3)_4Pb_5I_{16}$," Chem. **2**, 427 (2017).

J.-C. Blancon, H. Tsai, W. Nie, C. C. Stoumpos, L. Pedesseau, C. Katan, M. Kepenekian, C. M. M. Soe, K. Appavoo, M. Y. Sfeir, S. Tretiak, P. M. Ajayan, M. G. Kanatzidis, J. Even, J. J. Crochet, and A. D. Mohite, "Extremely efficient

internal exciton dissociation through edge states in layered 2D perovskites," Science **6331**, 1228 (2017).

L. A. A. Pettersson, L. S. Roman, and O. Inganas, "Modeling photocurrent action spectra of photovoltaic devices based on organic thin films," J. Appl. Phys. **86**, 487 (1999).

D. W. Sievers, V. Shrotriya, and Y. Yang, "Modeling optical effects and thickness dependent current in polymer bulk-heterojunction solar cells," J. Appl. Phys. **100**, 114509 (2006).

C. W. Chen, S.Y. Hsiao, C. Y. Chen, H. W. Kang, Z. Y. Huang, and H. W. Lin, "Optical properties of organometal halide perovskite thin films and general device structure design rules for perovskite single and tandem solar cells," J. Mater. Chem. A **3**, 9152 (2015).

J. M. Ball, S. D. Stranks, M. T. Horantner, S. Huttner, W Zhang, E. J. W. Crossland, I. Ramirez, M. Riede, M. B. Johnston, R. H. Friend, and H. J. Snaith, "Optical properties and limiting photocurrent of thin-film perovskite solar cells," Energy Environ. Sci. **8**, 602 (2015).

B. Xia, Z. Wu, H. Dong, J. Xi, W. Wu, T. Lei, K. Xi, F. Yuan, B. Jiao, L. Xiao, Q. Gong, and X. Hou, "Formation of ultrasmooth perovskite films toward highly efficient inverted planar heterojunction solar cells by micro-flowing anti-solvent deposition in air," J. Mater. Chem. A **4**, 6295 (2016).

P. Löper, M. Stuckelberger, B. Niesen, J. Werner, M. Filipič, S. J. Moon, J. H. Yum, M. Topič, S. De Wolf, and C. Ballif, "Complex refractive index spectra of $CH_3NH_3PbI_3$ perovskite thin films determined by spectroscopic ellipsometry and spectrophotometry," J. Phys. Chem. Lett. **6**, 66 (2015).

A. Forouhi and I. Bloomer, "Optical dispersion relations for amorphous semiconductors and amorphous dielectrics," Phys. Rev. B **34**, 7018 (1986).

M. S. Alias, I. Dursun, M. I. Saidaminov, E. M. Diallo, P. Mishra, T. K. Ng, O. M. Bakr, and B. S. Ooi, "Optical constants of $CH_3NH_3PbBr_3$ perovskite thin films measured by spectroscopic ellipsometry," Opt. Express **24**, 16586 (2016).

A. M. A. Leguy, P. Azarhoosh, M. I. Alonso, M. Campoy-Quiles, O. J. Weber, J. Yao, D. Bryant, M. T. Weller, J. Nelson, A. Walsh, M. van Schilfgaarde, and P. R. F. Barnes, "Experimental and theoretical optical properties of methylammonium lead halide perovskites," NanoscaleB **8**, 6317 (2016).

H. Fujiwara, "Spectroscopic Ellipsometry: Principles and Applications," John Wiley & Sons: Chichester, UK (2007).

T. Ishihara, J. Takahashi, and T. Goto, "Optical properties due to electronic transitions in two-dimensional semiconductors $(C_nH_{2n+1}NH_3)_2PbI_4$," Phys. Rev. B **42**, 11099 (1990).

M. Hirasawa, T. Ishihara, T. Goto, K. Uchida, and N. Miura, "Magnetoabsorption of the lowest exciton in perovskite-type compound $(CH_3NH_3)PbI_3$," Physica B **201**, 427 (1994).

M. Hirasawa, T. Ishihara, and T. Goto, "Exciton features in 0-, 2-, and 3-dimensional networks of $[PbI_6]^{4-}$," J. Phys. Soc. Jpn. **63**, 3870 (1994).

X. Hong, T. Ishihara, and A. V. Nurmikko, "Photoconductivity and electroluminescence in lead iodide based natural quantum well structures," Solid State Commun. **84**, 657 (1992).

X. Hong, T. Ishihara, and A. V. Nurmikko, "Dielectric confinement effect on excitons in PbI_4-based layered semiconductors," Phys. Rev B **45**, 6961 (1992).

K. Tanaka and T. Kondo, "Bandgap and exciton binding energies in lead-iodide-based natural quantum-well crystals," Sci. Technol. Adv. Mater. **4**, 599 (2003).

T. M. Koh, V. Shanmugam, J. Schlipf, L. Oesinghaus, P. Müller-Buschbaum, N. Ramakrishnan, V. Swamy, N. Mathews, P. P. Boix, and S. G. Mhaisalkar, "Nanostructuring mixed-dimensional perovskites: A route toward tunable, efficient photovoltaics," Adv. Mater. **28**, 3635 (2016).

G. Lakhwani, A. Rao, and R. H. Friend, "Bimolecular recombination in organic photovoltaics," Annu. Rev. Phys. Chem. **65**, 557 (2014).

D. Bartesaghi, I. del C. Perez, J. Kniepert, S. Roland, M. Turbiez, D. Neher, and L. J. A. Koster, "Competition between recombination and extraction of free charges determines the fill factor of organic solar cells," Nat. Commun. **6**, 7083 (2015).

S. D. Stranks, G. E. Eperon, G. Grancini, C. Menelaou, M. J. P. Alcocer, T. Leijtens, L. M. Herz, A. Petrozza, and H. J. Snaith, "Electron-hole diffusion lengths exceeding 1 micrometer in an organometal trihalide perovskite absorber," Science **342**, 341 (2013).

D. Wang, M. Wright, N. K. Elumalai, and A. Uddin, "Stability of perovskite solar cells," Sol. Energy Mater. Sol. Cells **147**, 255 (2016).

D. W. Dane, S. M. Vorpahl, S. D. Stranks, H. Nagaoka, G. E. Eperon, M. E. Ziffer, H. J. Snaith, and D. S. Ginger, "Impact of microstructure on local carrier lifetime in perovskite solar cells," Science **348**, 683 (2015).

Y. Yamada, T. Nakamura, M. Endo, A. Wakamiya, and Y. Kanemitsu, "Photocarrier recombination dynamics in perovskite $CH_3NH_3PbI_3$ for solar cell applications," J. Am. Chem. Soc. **136**, 11610 (2014).

M. Saba, M. Cadelano, D. Marongiu, F. Chen, V. Sarritzu, N. Sestu, C. Figus, M. Aresti, R. Piras, A. Geddo Lehmann, C. Cannas, A. Musinu, F. Quochi, A. Mura, and G. Bongiovanni, "Correlated electron-hole plasma in organometal perovskites," Nat. Commun. **5**, 5049 (2014).

V. D'Innocenzo, A. R. S. Kandada, M. De Bastiani, M. Gandini, and A. Petrozza, "Tuning the light emission properties by band gap engineering in hybrid lead halide perovskite," J. Am. Chem. Soc. **136**, 17730 (2014).

M. T. Trinh, X. Wu, D. Niesner, and X. Y. Zhu, "Many-body interactions in photo-excited lead iodide perovskite," J. Mater. Chem. A **3**, 9285 (2015).

T. J. Savenije, C. S. Ponseca, L. Kunneman, M. Abdellah, K. Zheng, Y. Tian, Q. Zhu, S. E. Canton, I. G. Scheblykin, T. Pullerits, A. Yartsev, and V. Sundström, "Thermally activated exciton dissociation and recombination control the carrier dynamics in organometal halide perovskite," J. Phys. Chem. Lett. **5**, 2189 (2014).

R. L. Milot, G. E. Eperon, H. J. Snaith, M. B. Johnston, and L. M. Herz, "Temperature-dependent charge-carrier dynamics in $CH_3NH_3PbI_3$ perovskite thin films," Adv. Funct. Mater. **25**, 6218 (2015).

L. M. Herz, "Charge-carrier dynamics in organic-inorganic metal halide perovskite," Rev. Phys. Chem. Mater. **67**, 65 (2016).

M. B. Johnston and L. M. Herz, "Hybrid perovskites for photovoltaics: charge-carrier recombination, diffusion, and radiative efficiencies," Acc. Chem. Res. **49**, 146 (2016).

R. L. Milot, R. J. Sutton, G. E. Eperon, A. A. Haghighirad, J. M. Hardigree, L. Miranda, H. J. Snaith, M. B. Johnston, and L. M. Herz, "Charge-carrier dynamics in 2D hybrid metal-halide perovskites," Nano Lett. **16**, 7001 (2016).

B. Wang, K. Y. Wong, S. Yang, and T. Chen, "Crystallinity and defect state engineering in organo-lead halide perovskite for high-efficiency solar cells," J. Mater. Chem. A **4**, 3806 (2016).

X.-H. Zhou, J. Luo, S. Huang, T.-D. Kim, Z. Shi, Y.-J. Cheng, S.-H. Jang, D. B. Knorr Jr., R. M. Overney, and A. K.-Y. Jen, "Supramolecular self-assembled dendritic

nonlinear optical chromophores: Fine-tuning of arene-perfluoroarene interactions for ultralarge electro-optic activity and enhanced thermal stability," Adv. Mater. **21**, 1976 (2009).

J. Zyss and J. L. Oudar, "Relations between microscopic and macroscopic lowest-order optical nonlinearities of molecular crystals with one- or two-dimensional units," Phys. Rev. A **26**, 2028 (1982).

Y.-J. Cheng, J. Luo, S. Hau, D. H. Bale, T.-D. Kim, Z. Shi, D. B. Lao, N. M. Tucker, Y. Tian, L. R. Dalton, P. J. Reid, and A. K-Y. Jen, "Large electro-optic activity and enhanced thermal stability from diarylaminophenyl-containing high-β nonlinear optical chromophores," Chem. Mater. **19**, 1154 (2007).

K. D. Singer, M. G. Kuzyk, and J. E. Sohn, "Second-order nonlinear-optical processes in orientationally ordered materials: relationship between molecular and macroscopic properties," J. Opt. Soc. Am. B **4**, 968 (1987).

K. D. Singer and L. A. King, "Relaxation phenomena in polymer nonlinear optical materials," J. Appl. Phys. **70**, 3251 (1991).

T. Kazmierczak, H. Song, A. Hiltner, and E. Baer, "Polymeric one-dimensional photonic crystals by continuous coextrusion," Macromol. Rapid Commun. **28**, 2210 (2007).

H. Wang, J. K. Keum, A. Hiltner, E. Baer, B. Freeman, A. Rozanski, and A. Galeski, "Confined crystallization of polyethylene oxide in nanolayer assemblies," Science **323**, 757 (2009).

M. Mackey, A. Hiltner, E. Baer, L. Flandin, M. A. Wolak, and J. S. Shirk, "Enhanced breakdown strength of multilayered films fabricated by forced assembly microlayer coextrusion," J. Phys. D: Appl. Phys. **42**, 175304 (2009).

K. D. Singer, J. E. Sohn, and S. J. Lalama, "Second harmonic generation in poled polymer films," Appl. Phys. Lett. **49**, 248 (1986).

K. D. Singer, M. G. Kuzyk, W. R. Holland, J. E. Sohn, S. J. Lalama, R. B. Comizzoli, H. E. Katz, and M. L. Schilling, "Electro-optic phase modulation and optical second-harmonic generation in corona-poled polymer films," Appl. Phys. Lett. **53**, 1800 (1988).

M. A. Mortazavi, A. Knoesen, S. T. Kowel, B. G. Higgins, and A. Dienes, "Second-harmonic generation and absorption studies of polymer-dye films oriented by corona-onset poling at elevated temperatures," J. Opt. Soc. Am. B **6**, 733 (1989).

K. D. Singer and A. F. Garito, "Measurements of molecular second order optical susceptibilities using dc induced second harmonic generation," J. Chem. Phys. **75**, 3572 (1981).

J. Feist and F. J. Garcia-Vidal, "Extraordinary exciton conductance induced by strong coupling," Phys. Rev. Lett. **114**, 196402 (2015).

J. Schachenmayer, C. Genes, E. Tignone, and G. Pupillo, "Cavity-enhanced transport of excitons," Phys. Rev. Lett. **114**, 196403 (2015).

E. Orgiu, J. George, J. Hutchison, E. Devaux, J. F. Dayen, B. Doudin, F. Stellacci, C. Genet, P. Samor, and T. W. Ebbesen, "Conductivity in organic semiconductors hybridized with the vacuum field," Nat. Mater. **14**, 1123 (2015).

J. H. Andrews, J. D. V. Khaydarov, K. D. Singer, D. L. Hull, and K. C. Chuang, "Characterization of excited states of centrosymmetric and noncentrosymmetric squaraines by third-harmonic spectral dispersion," J. Opt. Soc. Am. B **12**, 2360 (1995).

J. Bellessa, C. Bonnand, J. C. Plenet, and J. Mugnier, "Strong coupling between surface plasmons and excitons in an organic semiconductor," Phys. Rev. Lett. **93**, 036404 (2004).

J. Bellessa, C. Symonds, J. Laverdant, Jean-Michel Benoit, J. C. Plenet, and S. Vignoli, "Strong Coupling between Plasmons and Organic Semiconductors," Electronics **3**, 303 (2014).

T. K. Hakala, J. J. Toppari, A. Kuzyk, M. Pettersson, H. Tikkanen, H. Kunttu, and P. Törmä, "Vacuum rabi splitting and strong-coupling dynamics for surface-plasmon polaritons and rhodamine 6G molecules," Phys. Rev. Lett. **103**, 053602 (2009).

C. Symonds, J. Bellessa, J. C. Plenet, A. Bréhier, R. Parashkov, J. S. Lauret, and E. Deleporte, "Emission of hybrid organic-inorganic exciton/plasmon mixed states," Appl. Phys. Lett. **90**, 091107 (2007).

A. Salomon, S. Wang, J. A. Hutchison, C. Genet, and T. W. Ebbesen, "Strong light-molecule coupling on plasmonic arrays of different symmetry," ChemPhysChem **14**, 1882 (2013).

G. A. Wurtz, P. R. Evans, W. Hendren, R. Atkinson, W. Dickson, R. J. Pollard, A. V. Zayats, W. Harrison, and C. Bower, "Molecular plasmonics with tunable exciton-plasmon coupling strength in J-aggregate hybridized Au nanorod assemblies," Nano Lett. **7**, 1297 (2007).

N. T. Fofang, T.-H. Park, O. Neumann, N. A. Mirin, P. Nordlander, and N. J. Halas, "Plexcitonic nanoparticles: Plasmon-exciton coupling in nanoshell-J-aggregate complexes," Nano Lett. **8**, 3481 (2008).

J. Bellessa, C. Symonds, K. Vynck, A. Lemaitre, A. Brioude, L. Beaur, J. C. Plenet, P. Viste, D. Felbacq, E. Cambril, and P. Valvin, "Giant Rabi splitting between localized mixed plasmon-exciton states in a two-dimensional array of nanosize metallic disks in an organic semiconductor," Phys. Rev. B **80**, 033303 (2009).

N. J. Dawson, M. S. Patrick, S. Paul, B. Ellman, A. Semyonov, R. J. Twieg, R. Matthews, E. Pentzer, and K. D. Singer, "Interfacial trapping in an aged discotic liquid crystal semiconductor," J. Appl. Phys. **118**, 085502 (2015).

B. Maynard, Q. Long, E. A. Schiff, M. Yang, K. Zhu, R. Kottokkaran, H. Abbas, and V. L. Dalal, "Electron and hole drift mobility measurements on methylammonium lead iodide perovskite solar cells," Appl. Phys. Lett. **108**, 173505 (2016).

C. Wehrenfennig, M. Liu, H. J. Snaith, M. B. Johnston, and L. M. Herz, "Homogeneous emission line broadening in the organo lead halide perovskite $CH_3NH_3PbI_{3-x}Cl_x$," J. Phys. Chem. Lett. **5**, 1300 (2014).

Y. Jiang, X. Wen, A. Benda, R. Sheng, A. W. Y. Ho-Baillie, S. Huang, F. Huang, Y.-B. Cheng, and M. A. Green, "Time-resolved fluorescence anisotropy study of organic lead halide perovskite," Sol. Energy Mater Sol. Cells **151**, 102 (2016).